

**Merger Dynamics and Stellar Populations
in the Host Galaxies of the Quasi-Stellar Objects
I Zw 1 and 3C 48**

INAUGURAL-DISSERTATION

zur
Erlangung des Doktorgrades
der Mathematisch-Naturwissenschaftlichen Fakultät
der Universität zu Köln

vorgelegt von

Julia Scharwächter
aus Solingen

Köln 2005

Berichterstatter:

Prof. Dr. A. Eckart

Prof. Dr. P. Reiter

Tag der letzten mündlichen Prüfung: 02. Februar 2005

Zusammenfassung

Basierend auf Daten aus Nahinfrarot-Beobachtungen und numerischen Vielteilchensimulationen werden Fallstudien zu den zwei Quasistellaren Objekten (QSOs) I Zw 1 und 3C 48 vorgestellt. Die Motivation für diese Studien beruht auf der unbewiesenen Hypothese von Sanders et al. (1988), dass Ultraleuchtkräftige Infrarot-Galaxien (ULIRGs) ein Frühstadium von Quasistellaren Objekten darstellen. Die entsprechende Entwicklungssequenz, die zunächst durch starke Sternentstehungsaktivität und später durch die zunehmende Dominanz eines aktiven Galaxienkernes gekennzeichnet ist, könnte durch gravitative Wechselwirkungen und Verschmelzungen von Galaxien und den dadurch verursachten Gaszufluss zum Zentrum initiiert werden. Als vermutliche Beispiele für ein Übergangsstadium zwischen beiden Phasen verkörpern I Zw 1 und 3C 48 interessante Fallstudien, um die drei Kernpunkte der Entwicklungshypothese zu untersuchen: den aktiven Kern, die Sternentstehungsaktivität und die Anzeichen für Galaxienwechselwirkungen.

In der Fallstudie zu I Zw 1 liegt der Schwerpunkt auf Beobachtungsdaten, die Bilder und Spektren im Nahinfrarot-Bereich umfassen und mit *ISAAC (Infrared Spectrometer and Array Camera)* am *Very Large Telescope* der *Europäischen Südsternwarte (ESO)* auf Cerro Paranal in Chile aufgenommen wurden. Die Wirtsgalaxie von I Zw 1 ist eine zweiarmige Spiralgalaxie mit je einer hellen Quelle im nördlichen und im westlichen Teil der Galaxienscheibe. Die hier untersuchten ISAAC-Spektren der nördlichen Quelle deuten auf einen projizierten Vordergrundstern hin und belegen damit trotz jüngster Zweifel die bislang gängige Annahme, dass die Quelle nicht mit der Dynamik von I Zw 1 verbunden ist. Die ISAAC-Bilder unterstützen die Theorie einer gravitativen Wechselwirkung zwischen I Zw 1 und der westlichen Quelle, indem sie Strukturen aufweisen, die Gezeitenverformungen ähneln. Die vermutliche Satellitengalaxie scheint durch eine vorwiegend alte stellare Population gekennzeichnet zu sein. Diese Schlussfolgerung aus den Spektren ist im Einklang mit den aus den ISAAC-Bildern erhaltenen Nahinfrarot-Farben und mit früheren Ergebnissen aus optischen Spektren (Canalizo & Stockton 2001). Die Position der Nahinfrarot-Farben im Zweifarben-Diagramm ist bei der Rotverschiebung von I Zw 1 kein eindeutiger Indikator für das Alter der zugrunde liegenden Sternpopulation, da sich die Rötungseffekte durch Alterung gerade mit denen durch Staubextinktion überlagern. Grundsätzlich ergibt sich aus den Nahinfrarot-Farben von verschiedenen Regionen in der Wirtsgalaxie von I Zw 1 kein Widerspruch zu einer jüngeren Sternpopulation in der Nähe des Zentrums. Eine solche Tendenz deuten die Masse-Leuchtkraft-Verhältnisse an, die sich aus einer eindimensionalen Zerlegung des *J*-Band-Helligkeitsprofils und der Gas-Rotationskurve von I Zw 1 in eine Bulge-, Scheiben- und Halokomponente ergeben und im Falle des Bulges unter den solaren Werten liegen. Das neue ISAAC-Kernspektrum von I Zw 1 bestätigt die bekannten Ergebnisse des Spektrums von Schinnerer et al. (1998) und deutet ebenfalls stark blauverschobene Positionen für zwei koronale Linien an.

In der Fallstudie zu 3C 48, die den numerischen Schwerpunkt der Arbeit darstellt, werden Vielteilchensimulationen zu Galaxienverschmelzungen vorgestellt. Das Ziel ist, durch die Reproduktion eines qualitativen Modells für die Wirtsgalaxie von 3C 48 die vorhandenen Anzeichen für eine starke Galaxienverschmelzung zu analysieren. Ein solches Modell resultiert unter einem bestimmten Projektionswinkel aus der simulierten Verschmelzung zweier inklinierter, gleich schwerer Scheibengalaxien. Es spiegelt die grundsätzliche Morphologie der 3C 48 Wirtsgalaxie wider und die Tendenzen in den von

Canalizo & Stockton (2000) veröffentlichten stellaren Sichtliniengeschwindigkeiten. Im Modell ist einer der zwei entstandenen Gezeitenarme vor die Hauptgalaxie projiziert, was einen neuen Lösungsansatz für das Problem des scheinbar fehlenden zweiten Gezeitenarms bei 3C 48 bietet. Da beide Galaxienzentren im Simulationsmodell gerade noch getrennt sind, lässt sich nicht ausschließen, dass das bekannte zweite Helligkeitsmaximum nördlich des Kerns von 3C 48 das Zentrum einer der verschmelzenden Galaxien ist. Die hohen Gasansammlungen im Zentrum und die projizierten Bahnen hoher Gasdichte, die in einer Simulation mit nicht-gravitierender Gaskomponente entstehen, stimmen qualitativ mit den beobachteten Eigenschaften der molekularen Gaskomponente in 3C 48 überein.

Die neuen Ergebnisse fügen sich gut in das bestehende Bild ein, nach dem I Zw 1 und 3C 48 einem Übergangsstadium in der vermutlichen Entwicklungssequenz zugeordnet werden und damit wichtige Fallbeispiele in der Kontroverse um die globale Gültigkeit einer entwicklungsmäßigen Verbindung zwischen Ultraleuchtkräftigen Infrarot-Galaxien und Quasistellaren Objekten darstellen.

Abstract

The thesis focuses on two case studies of the host galaxies of the quasi-stellar objects (QSOs) I Zw 1 and 3C 48. The studies are motivated by the hypothesis that ultra-luminous infrared galaxies (ULIRGs) might represent the early stage of QSO evolution (Sanders et al. 1988). According to this hypothesis, galaxy mergers and interactions trigger gas inflow which is followed by starburst activity and by the formation of an active nucleus. As likely transitional objects between the ultra-luminous infrared stage and the QSO stage, I Zw 1 and 3C 48 are promising candidates to investigate the active nucleus, the starburst, and the merger properties as the essential links between all stages of the proposed evolutionary sequence.

The case study of I Zw 1 has an observational focus and is based on near-infrared (NIR) imaging and spectroscopy, carried out with *ISAAC (Infrared Spectrometer and Array Camera)* at the *Very Large Telescope* of the *European Southern Observatory (ESO)* on Cerro Paranal in Chile. The two-armed spiral host galaxy of I Zw 1 shows two bright knots in the north and in the west of the optical disk region, respectively. Here, the new ISAAC spectra indicate that the northern object is a projected foreground star, as previously assumed but recently challenged. In the surroundings of the western source, the ISAAC *J*-band image displays tidal features. This gives further support for the scenario that I Zw 1 is presently in a minor merger process with this source. The new spectra and the NIR colors of the western source indicate an old stellar population. The host of I Zw 1 is analyzed in a one-dimensional structural decomposition into bulge, disk, and halo components, which results in mean *J*-band mass-to-light ratios. The latter indicate a young mean stellar population in the bulge component, while the disk ratios agree with those of normal spiral galaxies. Such a scenario of younger stellar populations in the central region of the I Zw 1 host is also plausible from a two-color analysis. The nuclear ISAAC spectrum of I Zw 1 basically confirms previous results, by showing hydrogen emission lines and indications of extremely blueshifted high-excitation lines.

The case study of 3C 48 is the numerical focus of this thesis and based on simulations with multi-particle methods. The aim is to investigate the major merger scenario for 3C 48 by reproducing a 3C 48 model. Such a model is found for a certain projection angle during the inclined merger of two equal-mass spiral galaxies. It inspires a new idea for the problem of the apparently missing second tidal tail in 3C 48. For the derived projection angle, this tidal tail is located in front of the main body of the modeled host galaxy and is likely to be missed in observations. In the model, both galaxy centers are still separated. This leaves room to interpret the known second luminosity peak, north-east of the QSO in 3C 48, as the center of the galaxy merging with 3C 48. A central gas accumulation and a complex system of gas lanes develop in the simulation with a non-gravitating gas component added. Both results qualitatively agree with the known distribution of molecular gas in 3C 48.

The new results about I Zw 1 and 3C 48 complement the existing assumption that both are likely transitional objects in the evolutionary sequence.

Contents

I	Introduction	1
1	The Phenomenon of Nuclear Activity	1
1.1	Active Galactic Nuclei and Ultra-Luminous Infrared Galaxies	2
1.2	AGN Unification by Orientation	3
1.3	AGN Evolution	3
2	The Case Studies of I Zw 1 and 3C 48	6
2.1	Classification of AGN Host Galaxies	6
2.2	I Zw 1 and Properties of its Host Galaxy	8
2.3	3C 48 and Properties of its Host Galaxy	9
II	The Case Study of I Zw 1	13
3	ISAAC and Basic Observation and Reduction Techniques	13
3.1	Measures of Quality	13
3.2	Imaging Techniques and ISAAC Specifications	14
3.2.1	Integration Times	15
3.2.2	Sky Subtraction	15
3.2.3	Photometric Calibration and the <i>K</i> -Correction	16
3.3	Additional Features of Spectroscopy	18
4	ISAAC Observations of I Zw 1	20
4.1	Spectroscopy	21
4.1.1	Data Reduction	21
4.1.2	Telluric Correction and Calibration	22
4.1.3	Spectral Quality and Resolution	22
4.2	Imaging	23
4.2.1	Data Reduction	23
4.2.2	Calibration	24
4.2.3	Image Quality and Photometric Significance	24
4.3	The <i>K</i> -Correction for I Zw 1	28
5	Results	31
5.1	The <i>J</i> -Band Image	31
5.2	The Nuclear Spectrum of I Zw 1	32
5.2.1	Hydrogen Emission Lines	33
5.2.2	Coronal Lines	34
5.3	The Spectrum of the Northern Source	37
5.3.1	Continuum	38
5.3.2	Spectral Lines and Redshift	39
5.4	The Spectrum of the Likely Western Companion	41
5.4.1	Qualitative Analysis	43
5.4.2	A Tentative Quantitative Analysis	44

5.5	Near-Infrared Colors	46
5.5.1	The I Zw 1 Host	46
5.5.2	The Likely Western Companion	48
5.6	Structural Decomposition of the I Zw 1 Host Galaxy	49
5.6.1	Subtraction of the QSO Nucleus	49
5.6.2	First-Order Analysis of the Surface-Brightness Profile and the Gas Rotation Curve of the I Zw 1 Host	53
5.6.3	Gravitational Potential Models	55
5.6.4	Solutions for the Decomposition	56
5.6.5	Dynamical Discussion of the Solution for the Medium Case <i>Fit B</i>	60
5.6.6	Dynamical Mass-to-Light Ratios	61
5.6.7	Corrections for Stellar Mass-to-Light Ratios	62
5.6.8	Mean Stellar Populations	63
III The Case Study of 3C 48		65
6	Methods of Multi-Particle Simulations	65
6.1	Basic Dynamics of the Physical System	65
6.2	N-Body Simulations of Collisionless Systems	66
6.3	Smoothed Particle Hydrodynamics (SPH)	67
6.4	The Hierarchical Tree Method	68
7	Simulations	69
7.1	The Collisionless Simulation for 3C 48	69
7.1.1	The Initial Galaxy Models	70
7.1.2	The Orbital Configuration	71
7.1.3	The Simulation Run	73
7.1.4	Methods of Comparison with Observations	73
7.2	The Simulation with Gas	75
7.2.1	The Gas Component of the Initial Galaxy Model	75
7.2.2	The Simulation Run	76
8	Results	78
8.1	The Collisionless Model for 3C 48	78
8.1.1	Merger Orbit and Time Scales	78
8.1.2	The Location of the Second Tidal Tail	81
8.1.3	Kinematical Comparison	82
8.1.4	The Nature of 3C 48A	84
8.2	The Gas Model for 3C 48	84
8.2.1	Reliability of the Gas Model	85
8.2.2	Evolution of the Gas Simulation	87
8.2.3	The Gas Distribution in the 3C 48 Model	90
8.3	The 3C 48 Model as Observational Stimulus	92
IV Conclusions		93

9	Summary of the Individual Case Studies	93
9.1	I Zw 1 and the Two Nearby Sources	93
9.2	3C 48	94
10	The Merger Properties of I Zw 1 and 3C 48	94
10.1	3C 48 and the Toomre Sequence	95
10.2	Possible Scenarios for 3C 48 and I Zw 1	96
11	On the Discrepancies between ULIRGs and QSO Hosts	97
A	List of Abbreviations	99
B	The Program SIM2OBS	99
C	Cosmological Measures	100
D	Eddington Luminosity and Eddington Limit	101

Part I

Introduction

The investigations of this thesis are motivated by the ongoing discussion about the frequently-cited hypothesis that ultra-luminous infrared galaxies (ULIRGs) are the early stages of an evolutionary sequence to QSO host galaxies (Sanders et al. 1988). While the evoked scenario of merger-induced starburst activity and nuclear activity finds increasing support on the ULIRG-side (Sanders 1999, 2003, for reviews), evidence on the QSO-side is less established. Studies of ULIRGs and QSOs are intricate as they require to clearly separate the central active galactic nucleus (AGN) from the underlying host galaxy. Detailed imaging and spectroscopic data have only recently become accessible with the Hubble Space Telescope and the largest ground-based telescopes and will be an ongoing challenge for adaptive optics techniques or optical interferometry.

The improved statistical results from samples of ULIRGs and QSOs indicate that a global ULIRG-to-QSO evolutionary track is disputable. Discrepancies between the ULIRG and the QSO host populations are suggested for parameters, such as effective radii and surface brightnesses or stellar velocity dispersions, defining the location with respect to the fundamental plane of elliptical and S0 galaxies (Genzel et al. 2001; Veilleux et al. 2002; Tacconi et al. 2002; Dunlop et al. 2003, and the discussion in Sect. 11). Nevertheless, the ULIRG population shows basic similarities to the population of infrared-excess QSOs which are considered as transitional objects between the ULIRG and the QSO stage (Veilleux et al. 2002). These likely QSOs in the making are characterized by star formation activity, large masses of molecular gas, signs of gas outflows, and indications for recent merger processes (Boroson & Oke 1982; Boroson et al. 1982; MacKenty & Stockton 1984; Boroson et al. 1985; Hickson & Hutchings 1987; Hutchings & Crampton 1990; Lipari et al. 1994; Schinnerer et al. 1998; Evans et al. 2001; Surace et al. 2001; Canalizo & Stockton 2001; Scoville et al. 2003). They could be the key to a subset of QSOs which indeed follows the ULIRG-to-QSO evolutionary track.

The investigations presented here focus on two QSO hosts, I Zw 1 and 3C 48, which are known as typical transitional objects. Both are presented as templates for a transitional stage in the original publication by Sanders et al. (1988), (see also Fig. 1), both are in the sample of the transitional objects studied by Canalizo & Stockton (2001), and I Zw 1 belongs to the infrared-excess Palomar Green QSOs (e.g. Surace et al. 2001). By means of near-infrared (NIR) imaging and spectroscopy as well as multi-particle simulations, I Zw 1 and 3C 48 are investigated with a prime focus on the three essential links between the different stages of the assumed evolutionary sequence – galaxy mergers, starburst activity, and the AGN. In the concluding part, both case studies are directly compared to get a picture of their likely evolutionary history.

1 The Phenomenon of Nuclear Activity

QSOs show the most powerful form of nuclear activity, a phenomenon which was first discovered through unusually bright and point-like sources at radio wavelengths in the late 1950s. Their exceptional nature became clear in the early 1960s when the first optical spectra confirmed extremely high redshifts (Schmidt 1963; Greenstein & Schmidt 1964). Because of their star-like appearance whilst being located at extra-galactic distances, these

active galactic nuclei (AGN) were called *quasi-stellar radio sources* (*quasars*) or *quasi-stellar objects* (*QSOs*). From the historical point of view, 3C 48, one of the two case studies of this thesis (see Sect. 2.3 and Fig. 3), played an important role for the understanding of the QSO phenomenon. It was one of the first QSOs to be identified also at optical wavelengths (Matthews et al. 1961; Matthews & Sandage 1963). Furthermore, it was the first QSO found by direct spectroscopic evidence to be embedded in a host galaxy (Boroson & Oke 1982). This meant an important progress, since QSOs were no longer considered as isolated objects but as phenomena whose properties are closely entangled with the physical conditions in the host galaxy.

Descriptions of the phenomena associated with AGN and of the current status of AGN research can be found in Krolik (1999) and Urry (2004), respectively. The following outline is based on these references as well as on the publications cited in the text.

1.1 Active Galactic Nuclei and Ultra-Luminous Infrared Galaxies

From a purely empirical point of view, nuclear activity appears as a very diverse phenomenon manifesting itself with a wide variety of characteristics. This led to complex classification schemes and to naming-conventions which will be briefly summarized in Sect. 2.1. However, it is today's prevailing opinion that the physical mechanism for nuclear activity is basically the same for all kinds of AGN. The enormous luminosity from optical to X-ray energies is assumed to be caused by magnetic and/or viscous heating in the accretion disk and the corona of the AGN when gas and dust is accreted onto the central supermassive black hole. The Magorrian-relation between black hole and bulge mass (Magorrian et al. 1998) or the tight correlation between the black hole mass and the stellar velocity dispersion in the bulge (Ferrarese & Merritt 2000; Gebhardt et al. 2000) suggest that all galaxies with bulges, including elliptical galaxies as pure bulge galaxies, contain a supermassive black hole in their centers. In order to activate the supermassive black hole via accretion, a sufficient amount of fuel is required in the central region.

In gas-rich galaxies, large amounts of gas and dust are present in the disk. But the detailed nature of the fueling mechanisms which drive the gas and dust from the host disk to the immediate vicinity of the central black hole is still a matter of controversy. On large scales, i.e. kiloparsec scales, the transport is likely provided by bars, spiral arms, and other potential instabilities as possible consequences of galaxy interactions and/or mergers. On small scales, i.e. several Schwarzschild radii, the transport is taken over by the accretion process. For intermediate scales between several 100 pc and several Schwarzschild radii, the understanding of transport phenomena is just in its infancy, partly because this region in external galaxies has only recently become accessible with high-resolution observations. The NUGA¹ (NUclei of GALaxies) survey of 28 nearby AGN hosts (García-Burillo et al. 2003; Combes et al. 2004), originally based on high-resolution molecular gas data obtained with the IRAM Interferometer on Plateau de Bure in France, aims at a study of fueling mechanisms in a multi-wavelength approach. The first results show evidence for a surprising variety of secondary perturbations like lop-sidedness or nuclear spirals. Their role within the overall fueling process still needs clarification.

The investigations about the interplay between potential instabilities, AGN fueling, and starburst activity were stimulated in the 1980s when the all-sky survey of the Infrared

¹The NUGA team includes people from France, Spain, Italy, the USA, and Germany with the collaboration of Cologne.

Astronomical Satellite (IRAS) resulted in the discovery of a population of galaxies matching the bolometric luminosities of QSOs but mainly emitting their light in the infrared. According to their extreme infrared luminosities of $L_{\text{IR}(10-1000\mu\text{m})} > 10^{12} L_{\odot}$, these objects were called *ultra-luminous infrared galaxies (ULIRGs)* (Sanders & Mirabel 1996, for a review). The source of the high infrared luminosity is assumed to be a combination of starburst and AGN activity. However, it is still a matter of debate which of these processes produces the dominant contribution (e.g. Rigopoulou et al. 1999).

1.2 AGN Unification by Orientation

In view of the empirical diversity of nuclear activity, unification has naturally become a prime objective of AGN research.

In the most popular and promising unification scheme the diverse phenomena are attributed to orientation effects only. This scheme is based on the assumption that all kinds of AGN, independent of their observational appearance, are likewise composed of a supermassive black hole, an accretion disk and a corona, a broad- and a narrow-line region with high- and low-velocity gas, respectively, and an obscuring torus of gas and dust. At least in the case of radio-loud AGN, a further ingredient is given by the relativistic jet. The luminosity and perhaps the radio-loudness are considered as intrinsic properties resulting from the particular combination of physical states in the different building blocks. The differences in emission-line widths displayed by the so-called *type 1* and *type 2* AGN (see Sect. 2.1 for more details) are explained via different orientations of the obscuring torus with respect to the line-of-sight: If the torus is seen face-on, both, the broad- and the narrow-line regions, are visible (type 1 AGN). If the torus is seen edge-on, the broad-line region is hidden so that only emission lines from the narrow-line region are visible (type 2 AGN).

The classical scheme for radio-loud unification is independent of this optical one and based on the orientation of the radio jet axis only. If the jet points into the line of sight, the AGN appears as core-dominated with a flat spectrum. If the jet axis is seen under a certain angle, the AGN appears as lobe-dominated with a steep spectrum. However, there is still the possibility that a radio jet of varying power is also present in radio-quiet AGN but decelerated by high-density material in the host galaxies before becoming observable.

1.3 AGN Evolution

The evolutionary hypothesis, which is the focal point of this study, assumes ULIRGs as the precursors of QSOs (Sanders et al. 1988). The evolutionary link between ULIRGs and QSOs is suggested by several similarities between both populations.

- Both types of objects have comparable bolometric luminosities of about $10^{12} - 10^{12.5} L_{\odot}$ (Sanders et al. 1988).
- For the luminosity range of $10^{12} - 10^{12.5} L_{\odot}$ both types of objects have similar local space densities of $10^{-7} - 10^{-8} \text{ Mpc}^{-3}$ (Soifer et al. 1987).
- At least 25%-30% of the ULIRGs show typical signs of AGN activity, like AGN emission lines and point-like nuclei (Veilleux et al. 1999; Scoville et al. 2000).
- Almost all ULIRGs and some QSOs show clear indications of galaxy interactions (e.g. Bushouse et al. 2002).

- The spectral energy distributions show smooth transitions from ULIRG spectra characterized by far-infrared excess to QSO spectra characterized by UV brightness (Fig. 1).

The corresponding evolutionary scenario proposed by Sanders et al. (1988) is based on interactions and mergers of galaxies as the major mechanism for triggering gas inflow. The accumulation of material in the central regions of the galaxies is accompanied by strong starburst activity. An increasing amount of matter is accreted onto the supermassive black hole and a new AGN is formed or an already existing one is fueled. This is the ULIRG stage at which the combination of emission from the strong starburst activity and of AGN emission re-radiated by the dense dust-envelope causes an exceptional far-infrared luminosity. In the subsequent evolution, starburst activity subsides and at some stage the dust envelope of the AGN is blown away. In consequence of the cleared line-of-sight towards the AGN, the galaxy appears as a UV-bright QSO.

This scenario is temptingly simple but has recently been challenged by apparent discrepancies between the representatives of both populations (see the discussion in Sect. 11). Case studies of likely transitional objects like I Zw 1 and 3C 48 are promising to shed light on the discrepancies.

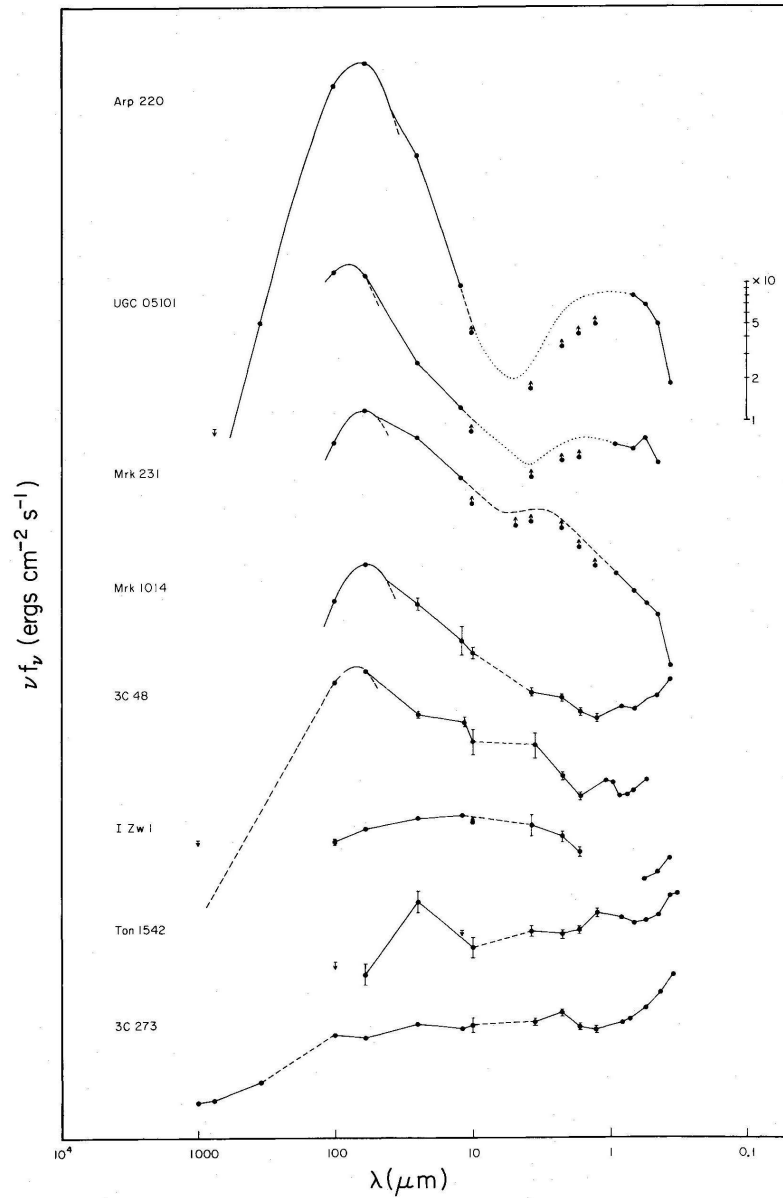


Figure 1: *Reproduction of Fig. 17 published by Sanders et al. (1988) to highlight the smooth transition of spectral energy distributions from ULIRGs to QSOs. The template ULIRGs are at the top of the sequence showing strong far-infrared excess. The template QSOs are at the bottom of the sequence and display the typical UV brightness. I Zw 1 and 3C 48 are classified as neighboring template objects at a transitional stage.*

2 The Case Studies of I Zw 1 and 3C 48

As shown in Fig. 1, I Zw 1 and 3C 48 are among the original objects used by Sanders et al. (1988) to highlight the smooth transition of spectral energy distributions from ULIRGs to QSOs and to propose the corresponding evolutionary sequence. Within this sequence, the two QSO hosts appear as neighboring templates at a transitional stage.

Both objects are qualified for a detailed observational and numerical approach by their particular properties. I Zw 1 and 3C 48 have coordinates of $\alpha_{2000} = 00\text{h}53\text{m}34.9\text{s}$, $\delta_{2000} = +12\text{d}41\text{m}36\text{s}$ (Falco et al. 1999) and $\alpha_{2000} = 01\text{h}37\text{m}41.3\text{s}$, $\delta_{2000} = +33\text{d}09\text{m}35\text{s}$ (Ma et al. 1998), respectively. The declinations allow for observations with the 8 m class unit telescopes of the Very Large Telescope located at a geographical latitude of about -24° on Cerro Paranal in Chile. I Zw 1 is outstanding from other QSO hosts regarding that it is one of the closest representatives at a redshift of only $z = 0.0611$ (Solomon et al. 1997). Given the corresponding conversion factor² of $1'' \approx 1.1$ kpc and the high angular resolving powers of large telescopes, resolutions on sub-kiloparsec scale are feasible. 3C 48, at a redshift of $z = 0.367$ (Barkhouse & Hall 2001), is outstanding from the more distant QSO host population in its unusual size and brightness. Applying the conversion factor² of $1'' \approx 4.1$ kpc, the size of the host of about $15'' \times 10''$ results in a physical size of $61.5 \text{ kpc} \times 41 \text{ kpc}$.

As the following introduction will show, I Zw 1 and 3C 48 belong to very distinct classes of AGN despite their common classification as transitional objects in the evolutionary sequence. While I Zw 1 is a radio-quiet QSO hosted in a galaxy which probably undergoes a minor merger, 3C 48 is a radio-loud QSO hosted in a likely major merger remnant. A complementary investigation of both case studies provides the opportunity to obtain a broad insight into the spectrum of properties displayed by transitional objects.

2.1 Classification of AGN Host Galaxies

The large variety of characteristics inherent to the AGN phenomenon has resulted in a complex classification scheme. The corresponding naming-scheme is not less complex, including *AGN*, *quasars*, *QSOs* (*quasi-stellar objects*), and *radio galaxies*, or *Seyfert galaxies* as examples of the most frequently-used terminology.

AGN are defined as radio-loud if their fluxes at 5 GHz and at 5000 \AA fulfill the criterion $\log(f_{5 \text{ GHz}}/f_{5000 \text{ \AA}}) > 1$. Originally, the terms *quasar* and *QSO* were only applied to radio-loud and radio-quiet AGN, respectively. But more often both terms are mixed and radio properties are stated explicitly. Similar to the criterion for radio loudness, high-luminosity AGN, called *QSOs*, are distinguished from low-luminosity AGN by a blue magnitude brighter than $M_B = -21.5 + 5 \log h$ (i.e. $M_B < -22.1$ for $H_0 = 75 \text{ km s}^{-1} \text{ Mpc}^{-1}$, $q_0 = 0.5$, Schmidt & Green 1983). However, the physical reality of these criteria is not as clear-cut. The reference fluxes are usually affected by variability, anisotropy, and/or dust extinction, and the transition from low- to high-luminosities of AGN is indeed continuous.

Based on their properties at radio wavelengths, radio-loud AGN are further distinguished by their *Fanaroff-Riley types*. If the ratio of the distance between the two brightest opposite radio spots to the overall size of the radio source is lower than 0.5, radio galaxies are of Fanaroff-Riley type 1, otherwise of type 2. A similar classification is indicated by

²Assuming $H_0 = 75 \text{ km s}^{-1} \text{ Mpc}^{-1}$ and $q_0 = 0.5$, the angular size distances (see Appendix C) of I Zw 1 and 3C 48 are 220 Mpc and 846 Mpc, respectively.

the terms *core-dominated* and *lobe-dominated*. Core-dominated objects usually have flat radio spectra, while lobe-dominated objects have steep radio spectra. The various ratios of core-to-lobe emission found for radio-loud AGN are explained via Doppler boosting effects if the radio jet is close to the line-of-sight. A peculiar subclass is composed of the *compact steep-spectrum sources (CSS)*. Their radio structures are core-dominated, extending less than 15 kpc, but the radio spectrum shows a steep power law with a turn-over frequency below 1 GHz. Although the role of CSSs within the unified schemes is still controversial, there is increasing evidence that the jets of these objects are mostly distorted. This suggests that the radio jets are interacting with the ambient interstellar medium.

The optical spectra of AGN are basically divided into a type 1 class with broad and narrow emission lines, and a type 2 class with narrow emission lines only. This convention applies to the host galaxies of radio-quiet AGN, which are consequently called *Seyfert 1* or *Seyfert 2*, and to radio galaxies, usually called *broad-line radio galaxies* and *narrow-line radio galaxies*. Intermediate widths of emission lines are considered via an additional decimal place in the type-numbering. As outlined in Sect. 1.2, the unification scheme assumes that type 2 AGN are hidden by an obscuring torus. The classical QSOs mostly show broad lines and, thus, belong to the type 1 objects. The issue of type 2 QSOs, which should be highly obscured like ULIRGs but dominated by the AGN rather than the starburst, has been a matter of debate (e.g. Maiolino 2001). Only recently, a significant number of likely QSO 2 identifications has been found using the data base of the Sloan Digital Sky Survey (e.g. Zakamska et al. 2003, and references therein).

A special subclass of Seyfert 1s is formed by the *narrow-line Seyferts 1s (NLS1)*. Similar to Seyfert 2s, they show narrow permitted lines with a full width at half maximum (FWHM) of about 1000 km s^{-1} . But their low excitation state ($[\text{O III}] \lambda 5007 \text{ \AA} / \text{H}\beta < 3$) is typical of Seyfert 1s. Their spectra display many Fe II multiplets (Osterbrock & Pogge 1985). In the X-ray regime, NLS1s are often characterized by variability as well as rather steep spectral slopes at the soft X-rays (Boller et al. 1996). The role of NLS1s in unification schemes is still controversial. They could be Seyfert 1s with extremely pole-on orientations of a disk-like broad-line region (e.g. Boller et al. 1996; Bian & Zhao 2004). But there is also increasing evidence that the narrow emission lines of NLS1s arise from smaller black hole masses and higher accretion rates (e.g. Pounds et al. 1995; Mathur 2000; Botte et al. 2004).

It is well known that the class of *broad absorption line QSOs (BALQSOs)* shows many similarities to NLS1s (e.g. Leighly et al. 1997; Brandt & Gallagher 2000). BALQSOs are defined as particular QSOs with strong signs of outflows from the broad line region. Similar to the unification schemes for NLS1s, BALQSOs can be unified with non-BALQSOs via orientation or via black hole mass and accretion rate. In the first case, all QSOs are considered as objects with anisotropic outflows which are coincidentally directed along the line-of-sight when the object appears as a BALQSO (Weymann et al. 1991; Willott et al. 2003). In the second case, BALQSOs differ from non-BALQSOs by higher accretion rates close to the Eddington limit³ (Yuan & Wills 2003; Maiolino et al. 2004, and references therein). The intriguing similarities between NLS1s and BALQSOs suggest the possibility that NLS1s are the nearby, low-luminosity counterparts of BALQSOs (Mathur 2000). Both classes of objects could be manifestations of an early stage in AGN evolution at which the material, initially obscuring the AGN, is just in the process of being blown away (Fabian

³see Appendix D

1999; Mathur 2000; Leighly et al. 1997; Brandt & Gallagher 2000). This would represent an interesting interconnection between NLS1-type QSOs or BALQSOs and the scenario evoked for the ULIRG-to-QSO evolutionary sequence.

2.2 I Zw 1 and Properties of its Host Galaxy

With an infrared luminosity of $L_{\text{IR}} = 10^{11.87} L_{\odot}$ (Canalizo & Stockton 2001), I Zw 1 just fails the ULIRG criterion (Sect. 1.1). In contrast, with a nuclear blue magnitude of $M_B = -22.62$ (Canalizo & Stockton 2001), it just meets the QSO criterion. Since the transition to Seyfert galaxies is fluent at the low-luminosity tail of QSOs, I Zw 1 is also classified as the prototypical narrow-lined Seyfert 1 galaxy (NLS1). Its weak UV absorption and the remarkably red continuum are reminiscent of BALQSOs and the NLS1-BALQSO similarities (Laor et al. 1997). Outflows from the broad-line region of I Zw 1 are also suggested by an extremely blueshifted line system in the spectrum of I Zw 1. Instead of the simple broad and narrow lines, expected for emission from the broad- and narrow-line regions, the optical spectrum of I Zw 1 reveals a complex mixture of four different line systems (Véron-Cetty et al. 2004):

- A low-excitation narrow-line system (FWHM $\sim 300 \text{ km s}^{-1}$) consisting of Balmer lines, [N II], [S II], [O I], [Ca II], Si II, N I, and N II at the redshift of I Zw 1,
- A broad-line Lorentzian system (FWHM $\sim 1100 \text{ km s}^{-1}$), consisting of Balmer lines, He I, Na I, Ti II, and Si II blueshifted by about 150 km s^{-1} ,
- And two high-excitation narrow-line systems (FWHM $\sim 1900 \text{ km s}^{-1}$ and FWHM $\sim 920 \text{ km s}^{-1}$) consisting of H α , H β , [O III], [Ne III], [Fe VII], [N II], and [S II] and being significantly blueshifted by about 1450 km s^{-1} and 500 km s^{-1} , respectively.

The blueshift seems to increase with ionization level in the UV and optical spectra (Laor et al. 1997). Similarly high blueshifts of about 1350 km s^{-1} are exhibited by the NIR coronal lines of [Si VI] $\lambda = 19634 \text{ \AA}$ and [Al IX] $\lambda = 20400 \text{ \AA}$ (Schinnerer et al. 1998). Such coronal lines seem to originate from coronal line regions which trace the kinematics at distances between the classical broad- and narrow-line regions (Rodríguez-Ardila et al. 2002).

Fig. 2 shows one of the new NIR images of the I Zw 1 host obtained with the ISAAC camera at the Very Large Telescope of the European Southern Observatory. The host has an extended disk with an optical diameter of about $12''$ inclined by $(38^{\circ} \pm 5^{\circ})$ around the kinematic major axis at a position angle of 135° (Schinnerer et al. 1998). The disk shows two asymmetric spiral arms starting on the eastern and the western side of the nucleus and arcing counterclockwise. The stronger western arm passes by a bright source in the west and points towards another source to the north of the I Zw 1 disk. These two sources and their natures are central parts of this study and are discussed by means of the new ISAAC data in Part II.

The western object is clearly extended and considered as a likely companion galaxy. Its systemic line-of-sight velocity is very similar to that of I Zw 1, with a velocity difference of only $\Delta v = (170 \pm 110) \text{ km s}^{-1}$ (Canalizo & Stockton 2001). Although the velocity field of molecular and atomic gas within the region of the optical disk of I Zw 1 is very regular (Schinnerer et al. 1998; Lim & Ho 1999), a tidal interaction with the companion is suggested by the asymmetric distribution of atomic hydrogen at larger distances. Starting

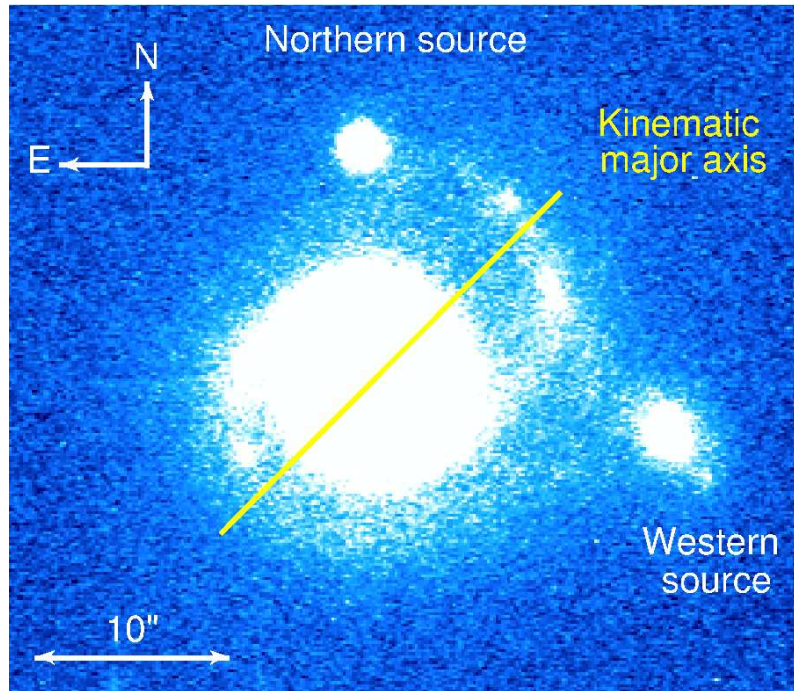


Figure 2: The new ISAAC J-band image of I Zw 1. The kinematic major axis as well as the two other sources in the field are highlighted. This image and the complementary H- and K-band data will be discussed and analyzed in Part II.

at about $15''$ to $20''$ from the I Zw 1 nucleus, HI shows two tidal-arm-like extensions on either side of the disk, pointing roughly towards and away from the companion (Lim & Ho 1999). Numerical multi-particle simulations indicate that the stellar two-armed spiral of the I Zw 1 host could be a consequence of an ongoing minor merger process with the companion object (Scharwächter 2001). The northern source is either suggested as a projected foreground star (Sargent 1970; Stockton 1982), or as a tidal dwarf galaxy or the nucleus of an interacting galaxy (Davies et al. 2003).

The mass of molecular gas in the I Zw 1 host of $M_{H_2} \approx 9 \times 10^9 M_{\odot}$ (computed from Schinnerer et al. 1998) is typical of gas-rich spiral galaxies. Enhanced star-formation activity is displayed by the north-western spiral arm as well as the circum-nuclear region (Canalizo & Stockton 2001; Schinnerer et al. 1998). Interferometric observations of ^{12}CO (1-0) in I Zw 1 show evidence for a circum-nuclear molecular ring with a radius of about 1.2 kpc (Staguhn et al. 2004). The cloud complexes in this ring are likely parts of the nuclear starburst sites.

2.3 3C 48 and Properties of its Host Galaxy

Regarding the strong infrared luminosity of $L_{\text{IR}} = 10^{12.81} L_{\odot}$ and the bright blue magnitude of $M_B = -24.55$ of 3C 48 (Canalizo & Stockton 2001), this object matches the ULIRG as well as the QSO definition. The high infrared luminosity seems to originate from dust heated by vigorous star formation activity (Neugebauer et al. 1985). In contrast to I Zw 1, 3C 48 is radio-loud and belongs to the peculiar class of compact steep-spectrum sources (see Sect. 2.1). The relatively weak radio core is elongated in north-south direction

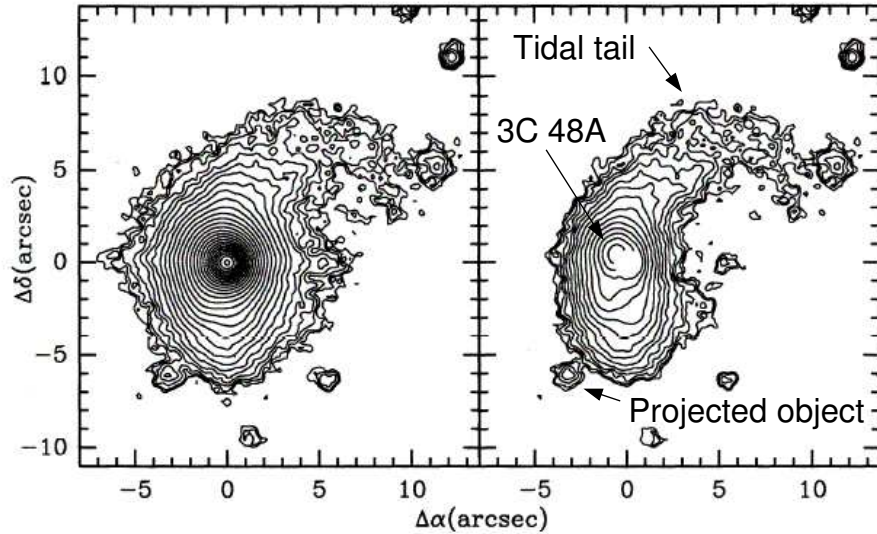


Figure 3: *3C 48* in a reproduction of Fig. 2 from Stockton & Ridgway (1991). The labels are added to the original image. The figure shows the sum of images obtained in filters at 5800 \AA and at 7655 \AA . The left image is the original one. In the right image, Stockton & Ridgway (1991) subtracted a scaled stellar profile to remove the QSO component. By the right image, Stockton & Ridgway (1991) found the high-surface-brightness region 3C 48A at about $1''$ north-east of the QSO position.

and is the origin of a powerful one-sided radio jet which expands to about $1''$ north-east (Wilkinson et al. 1991). As often found for compact steep-spectrum sources, the radio jet is significantly disrupted. This disruption seems to be caused by a strong interaction with the dense interstellar medium. Investigations of the ionized gas in the circum-nuclear region of 3C 48 reveal two emission line components, a narrow one ($\text{FWHM} \sim 400 \text{ km s}^{-1}$) close to the systemic velocity of 3C 48 and a broad one ($\text{FWHM} \sim 1000 \text{ km s}^{-1}$) blueshifted by about 580 km s^{-1} and displaying a large velocity gradient over the central region (Chatzichristou et al. 1999; Canalizo & Stockton 2000). The blueshifted component is most likely driven by an interaction with the radio jet. The fact that the corresponding red emission line component is missing suggests that the radio jet could be intrinsically one-sided. Alternatively, the opposite direction could be either void of gas or extinguished by dust (Chatzichristou et al. 1999).

A second luminosity peak, 3C 48A, is found in NIR and optical images at about $1''$ to the north-east of the 3C 48 QSO nucleus (Fig. 3; Stockton & Ridgway 1991; Zuther et al. 2004). Its nature is still controversially discussed. There are basically the three alternatives (Stockton & Ridgway 1991): First, 3C 48A could be the center of a second galaxy in an advanced merger state. Second, it could be a hot spot of enhanced star formation incited by the radio jet. Finally, it could be a peak of scattered light from the AGN.

The interpretation of 3C 48A as a second galaxy center is tempting with respect to the disturbed overall morphology of the 3C 48 host. As evident from Fig. 3, the unusually large size of the host galaxy is dominated by the arc-like extension about $15''$ to the north. Its shape strongly suggests a tidal origin from a recent major merger event. A drawback of the major merger assumption for 3C 48 is the apparently missing counter tidal tail which would be expected to be formed during the merger of two massive galaxies. A tail-

like extension to the south-east has been identified as a projected object not belonging to the 3C 48 system (Canalizo & Stockton 2000; Zuther et al. 2004). In an alternative scenario, a tidal tail could bend from the south-east of the QSO nucleus to the south-west (Canalizo & Stockton 2000). However, a clear identification has failed so far. The north-western tidal tail is basically characterized by an old stellar population but also contains some clumps indicating recent star formation activity. The central region reveals young stellar populations and ongoing star formation activity (Canalizo & Stockton 2000). The indications for ongoing starburst activity are consistent with the large amounts of molecular gas of a few times $10^{10} M_{\odot}$ (Scoville et al. 1993; Wink et al. 1997).

Part II

The Case Study of I Zw 1

This part deals with the reduction and analysis of the NIR imaging and spectroscopy data obtained with the ISAAC camera at the Very Large Telescope (VLT) of the European Southern Observatory (ESO) on Cerro Paranal in Chile. The nuclear properties of the I Zw 1 QSO and the nature of the northern and the western source mentioned in Sect. 2.2 are addressed by means of the H - and K -band spectra. The high angular resolution of the imaging observations provides insights into the likely merger process with the western source. The available data from the three NIR bands are used for investigating the colors of the western source and the host of I Zw 1. Based on the J -band image and the gas rotation curve, the I Zw 1 host galaxy is decomposed into bulge, disk, and halo contributions and mean mass-to-light ratios are computed for the luminous components.

3 ISAAC and Basic Observation and Reduction Techniques

ISAAC is the acronym for the Infrared Spectrometer and Array Camera, operated at the Very Large Telescope (VLT) of the European Southern Observatory (ESO) since April 1999 (Moorwood et al. 1998). The camera is installed at the Nasmyth B focus of UT1 (Antu), the first of the four 8.2 m Unit Telescopes of the VLT on Cerro Paranal in the Atacama Desert in Chile. It provides observation modes for imaging, long-slit spectroscopy, and polarimetry in the NIR and infrared from 0.9 μm to 5.0 μm (9000 \AA to 50 000 \AA), with two separate arms for the short wavelength and the long wavelength domains. Carried out with the short wavelength arm, the ISAAC observations for I Zw 1 were detected with the Rockwell Hawaii 1024 \times 1024 pixel array which provides a pixel scale of 0".1484/pixel and a field-of-view of 152" \times 152". As a natural consequence of the given read-out speed, the detector integration time is limited to a minimum of 3.55 s. Integrations are controlled and pre-processed by the ESO-IRACE controller.

3.1 Measures of Quality

The information content of any astronomical image depends on the spatial resolution measured via the point-spread function (PSF) and the sensitivity measured via the signal-to-noise ratio (S/N) or the limiting magnitude. A more detailed description than the following outline can be found in Howell (2000).

As a consequence of diffraction and seeing, an ideal point source is spread over several pixels of the array in reality. This spread is measured by the PSF. A first-order measure of the angular resolution can be obtained from the FWHM of an assumed Gaussian PSF.

The S/N is defined as the ratio of the signal from the object to the total noise. The latter is composed of the noise from the object signal, the noise from the sky background, the dark current of the detector, and the read noise of the detector. Under the assumption that all sources of noise are statistically independent and either due to Poisson noise or to signal-independent noise, the S/N for a signal integrated over an aperture of n pixels is given by

$$\text{S/N} = \frac{S_{\text{obj}}nT}{\sqrt{S_{\text{obj}}nT + S_{\text{bg}}nT + N_d nT + R_d^2 n}}, \quad (3.1)$$

where S_{obj} , S_{bg} , and N_d are the object signal level, the sky signal level, and the dark current of the detector, respectively measured in electrons per pixel per unit time. R_d is the read noise of the detector in root-mean-square (RMS) electrons per pixel, and T is the detector integration time. In the case of a point source, n is the number of pixels of the PSF which have to be integrated to recover the total signal. For a Gaussian PSF, this is approximately the number of pixels within an aperture with a size of $4 \times \text{FWHM}$ around the PSF peak. If the source is extended and the aim is to measure its total flux, n has to be replaced by the size of the object. If the aim is to investigate structural properties, a suitable noise measurement is given by the S/N per pixel or per spatial resolution element. In the former case, n is one; in the latter case, n corresponds to the number of pixels within an aperture of the size of the FWHM of the PSF. Binning of n pixels improves the S/N per pixel by a factor of \sqrt{n} . Longer integration times also improve the S/N, which scales with \sqrt{T} in the typical case of NIR observations where the dominant noise contribution comes from the sky background emission, i.e. $S/N \approx S_{\text{obj}}nT/\sqrt{S_{\text{bg}}nT} \propto \sqrt{T}$. Since the observations are background-limited, the noise level of the reduced images can be obtained from the RMS (σ) of several aperture measurements of the background flux at different positions in the image, using suitable aperture sizes.

Other intuitive measures are the limiting magnitude or limiting surface-brightness. These measures mean the magnitude or surface-brightness, which can just be distinguished from the background noise at a 1σ - or 3σ -level. They can be computed from the background RMS or three times the background RMS, expressed in magnitudes or surface-brightnesses, respectively.

The quality of one-dimensional spectra depends on the spectral resolution and the S/N. The spectral resolution is defined as $Rs = \lambda/\Delta\lambda$. In practice, the spectral resolution element $\Delta\lambda$ can be determined from the FWHM of a Gaussian fit to lines which are intrinsically narrow. A suitable choice of lines is provided by the arc lines usually measured for wavelength calibration.

The S/N can be specified in different ways, depending on the particular objectives of the investigations. One possibility is to compute the S/N from the ratio of the peak flux of a line to the RMS fluctuations of the continuum. Alternatively, the S/N can be derived by integrating the line flux as well as the continuum RMS over the width of the spectral resolution element or, in case that the measured line is intrinsically broad, over the width of the line.

3.2 Imaging Techniques and ISAAC Specifications

Observations from ground-based telescopes are affected by the fluorescent and thermal emission of the atmosphere. As e.g. described in Glass (1999), the continuum- and line-emission associated with fluorescence is caused by the recombination of electrons and ions which have been dissociated by photochemical reactions during day time. Fluorescent emission is increasing from optical towards NIR wavelengths (Fig. 4). In the NIR, the emission mainly originates from the radical OH. At wavelengths above $2.2 \mu\text{m}$ fluorescence is dominated by thermal emission from the atmosphere.

Most of the following summaries of observing and reduction techniques is based on the practical descriptions provided by the ISAAC user manual⁴ and the ISAAC reduction

⁴http://www.eso.org/instruments/isaac/userman/umhtml/um1_10_1.html, Issue 1.8.3

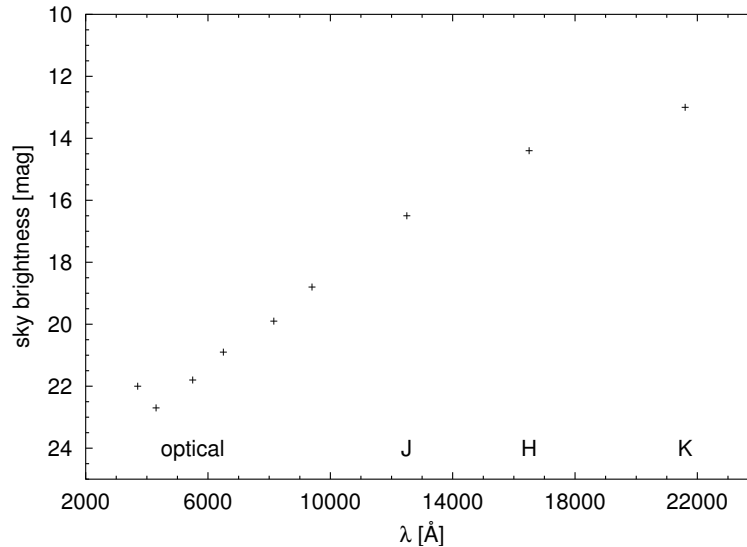


Figure 4: *Brightness of the sky background produced by atmospheric fluorescent and thermal emission. The magnitudes are taken from the descriptions of the exposure time calculators provided by ESO (<http://www.eso.org/observing/etc/>). Optical values from the U- to the z-band refer to the calculator for the VIMOS instrument working in the optical wavelength domain. The NIR data refer to the calculator for ISAAC.*

guide⁵. A general overview about photometry and photometric systems can be found in e.g. Binney & Merrifield (1998).

3.2.1 Integration Times

Because of the strong sky background, NIR observations are generally characterized by shorter but more frequent exposures than optical observations. In order to avoid an excess need for storage space, it is a usual technique to directly average a given number of integrations during pre-processing.

The detector integration times for imaging observations should be long enough to distinguish faint objects or structures from the background emission but short enough to prevent saturation by the brightest object in the image. Some standard integration times recommended by the ISAAC user manual are listed in Table 1.

3.2.2 Sky Subtraction

A simple NIR observation program is made up of object frames and calibration frames. In the classical on-off technique required for an accurate subtraction of the strong background emission of the night sky at NIR wavelengths, the object frames consist of an alternating series of object and sky exposures. During data reduction, the sky exposures are subtracted from the object frames. For observations in an uncrowded field, this method can be applied efficiently by shifting the object across the detector in a sequence of object exposures. If the offsets are chosen so that the object position in one frame overlaps with sky in another

⁵<http://www.eso.org/instruments/isaac/drg/html/>, Issue 1.4

Table 1: Standard values for extinction, recommended detector integration times (DITs), and recommended exposure times per frame (i.e. the number of integrations averaged during pre-processing (NDIT) multiplied by the detector integration time) for imaging as well as low-resolution (LR) and medium-resolution (MR) spectroscopy with ISAAC on Cerro Paranal. The data are taken from the ISAAC user manual.

	Filter		
	<i>J</i>	<i>H</i>	<i>K_s</i>
Extinction [mag (air mass) ⁻¹]	0.11	0.06	0.07
Imaging DITs [s]	30 – 60	10 – 15	10 – 15
Imaging DIT × NDIT [s]	60 – 180	60 – 120	60 – 120
LR spectroscopy DITs [s]	60 – 200	60 – 200	60 – 200
LR spectroscopy DIT × NDIT [s]	60 – 200	60 – 200	60 – 200
MR spectroscopy DITs [s]	300 – 900	300 – 900	300 – 900
MR spectroscopy DIT × NDIT [s]	300 – 900	300 – 900	300 – 900

frame, sky-subtraction is possible without additional integration time on the sky. Sky-subtraction is either done by directly subtracting the frames for all possible permutations. Alternatively, a separate sky frame can be obtained by combining the object frames via a median algorithm. This median sky is subsequently subtracted from each object frame. The sky-subtracted frames are aligned to a common offset and added up via a mean or median combination. The RMS noise of the reduced image scales as $1/\sqrt{N_{\text{frame}}}$ with the number of input frames. As the sky emission depends on the air mass, variations in air mass can cause systematic errors during sky subtraction. Suitable combinations of object and sky frames are only given by those exposures observed at similar times. The ISAAC user manual recommends maximum time intervals on either side of the object frames of 10 to 20 minutes for *J*-band observations and of 5 to 10 minutes for *H*- and *K_s*-band observations. A good sky sampling requires to reduce the integration times of each exposure for the benefit of a larger number of exposures.

3.2.3 Photometric Calibration and the *K*-Correction

The calibration frames include dark frames, sky flats, and standard star exposures. Dark frames are exposures without detector illumination, measuring the dark current of the detector. Such frames are not required if the on-off technique is applied, since sky and dark current are simultaneously removed during the subtraction step. Flat fields are needed to correct for variations of the response to a signal from pixel to pixel within one frame. ISAAC flat fields are measured as twilight flats by imaging an empty region of the sky in a series of ten to twenty exposures during twilight. The time series of frames with increasing or decreasing illumination is used to determine the pixel gain by measuring the slope of the signal level for each pixel. In order to flatten the object frames, they are divided by the normalized image of pixel gains.

After the image is flattened and cleaned from the contributions of the sky background emission and the dark current, the counts have to be calibrated in fluxes. The magnitude

of an object of specific flux f_ν is given by

$$m = -2.5 \log \int_0^\infty f_\nu S_\nu d\nu + ZP - EXT, \quad (3.2)$$

where S_ν is the sensitivity of the telescope system, including filter characteristics and the receiving efficiency, EXT is the correction for the extinction of the atmosphere, and ZP defines the zero point of the photometric system.

The standard photometric systems are based on Vega or a mean A0V star as the calibrator for zero magnitudes and zero colors. Usually the photometric system consists of several standard stars, calibrated relative to the zero magnitude star. In the ideal case, these standard stars are distributed over the sky so that each observation is provided with a nearby calibrator. In practice, the exposures taken for the standard stars are reduced like the object frames. The total counts received from the standard star per unit integration time are measured by integrating over an aperture suitably large to account for the effects of point-spreading (Sect. 3.1). From the known magnitude m_{star} of this star, the ZP is derived by using Equation (3.2) in the form

$$ZP = m_{\text{star}} + 2.5 \log(\text{counts}) + EXT. \quad (3.3)$$

Tabulated values for the mean extinction per air mass are provided by the Paranal observatory (see Table 1). Since the standard star observations and the object observations are usually affected by different air masses, it is convenient to combine all extinction effects in the form of a corrected zero point $ZP_c = ZP + EXT_{\text{star}} - EXT_{\text{obj}}$. Using this definition of a corrected zero point, the counts per unit integration time of any object integrated over any aperture translate into a magnitude

$$m_{\text{obj}} = -2.5 \log(\text{counts}) + ZP_c. \quad (3.4)$$

If the pixel scale of the detector is used to convert the counts per pixel into counts per arcsec², Equation (3.4) results in surface brightnesses μ , according to

$$\mu_{\text{obj}} = -2.5 \log(\text{counts}) + 5 \log(\text{pixel scale}) + ZP_c, \quad (3.5)$$

where the pixel scale is defined in arcseconds per pixel.

The integral in Equation (3.2) shows that the measured flux does not only depend on the filter and detector characteristics of the telescope system but also on the spectral slope of the object. These color terms are less important in narrow-band photometry but can be significant in broad-band photometry. The calibration measurements for any photometric system are influenced by the same factors. This means that each photometric system is bound to a particular filter-detector configuration. Color transformations between the photometric systems have to be determined from studies comparing the magnitudes and colors of the same stars in different systems. The calibration of ISAAC imaging in the range from 1 μm to 2.5 μm is mainly based on the LCO/Palomar NICMOS system of faint NIR standards (Persson et al. 1998). Unfortunately, color transformations between both filter systems have not yet been experimentally analyzed but are assumed to be negligible for the J -, H -, and K_s -band filters (ISAAC reduction guide).

Besides the LCO system, three photometric systems will be used for interpreting and discussing the ISAAC data on I Zw 1: the UKIRT system (Hawarden et al. 2001), the

2MASS system⁶, and the Bessell & Brett (BB) system (Bessell & Brett 1988). The comparison of the UKIRT and LCO systems shows no color terms but an offset in zero points (Hawarden et al. 2001). The other transformation terms are computed from the data given on the 2MASS web page⁶. The error bars reported by (Hawarden et al. 2001) and on the web page are left out here to make the formulae more transparent. The multiplication factors in the first column on the right-hand side have errors of less than 5%, while the additive terms in the last column have errors between about 30% and 150%.

UKIRT → LCO

$$\begin{aligned} (J)_{\text{LCO}} &= (J)_{\text{UKIRT}} + 0.034 \\ (H)_{\text{LCO}} &= (H)_{\text{UKIRT}} + 0.027 \\ (K)_{\text{LCO}} &= (K)_{\text{UKIRT}} + 0.015 \end{aligned}$$

2MASS → LCO

$$\begin{aligned} (Ks)_{\text{LCO}} &= (Ks)_{2\text{MASS}} + 0.015 - 0.00198(J - Ks)_{2\text{MASS}} \\ (J - Ks)_{\text{LCO}} &= 0.988(J - Ks)_{2\text{MASS}} + 0.0069 \\ (H - Ks)_{\text{LCO}} &= 0.985(H - Ks)_{2\text{MASS}} - 0.00296 \end{aligned}$$

BB → LCO

$$\begin{aligned} (Ks)_{\text{LCO}} &= (K)_{\text{BB}} - 0.024 - 0.00094(J - K)_{\text{BB}} \\ (J - Ks)_{\text{LCO}} &= 0.971(J - K)_{\text{BB}} - 0.0109 \\ (H - Ks)_{\text{LCO}} &= 0.957(H - K)_{\text{BB}} - 0.0305 \end{aligned} \tag{3.6}$$

The absolute magnitude measured for the same galaxy in a certain band changes with the distance of the galaxy as a consequence of the increasing redshift of the spectrum. Depending on the slope of the spectral energy distribution (SED) in the observation band, this change can be rather significant. The corrective term which has to be applied to retrieve the true rest-frame magnitude $m_{\text{rest}}(A)$ in band A from the measured magnitude $m_{\text{obs}}(A)$ is called K -correction

$$m_{\text{rest}}(A) = m_{\text{obs}}(A) - KC. \tag{3.7}$$

Accordingly, the rest-frame colors of a galaxy in bands A and B follow from

$$(A - B)_{\text{rest}} = (A - B)_{\text{obs}} - KC_{(A-B)}. \tag{3.8}$$

The K -correction depends on the sensitivity of the filter curve used for the observations and on the shape of the SED of the object under study. In fact, an accurate correction also has to take into account the evolution of the SED distribution with redshift. Complicated by the fact that the SEDs of QSO host galaxies display mixtures of QSO and galaxy spectra, the K -correction models will be used to provide general trends rather than exact corrective terms.

3.3 Additional Features of Spectroscopy

In long-slit observations, the spectroscopic frames consist of two-dimensional images with one spectral and one spatial axis. The slit is inserted into the beam just behind the

⁶see <http://www.astro.caltech.edu/~jmc/2mass/v3/transformations/>

entrance window of the camera. In the case of ISAAC, the slits are $120''$ long and available at widths of $0''.3$, $0''.6$, $1''.0$, and $2''.0$. The slit position is specified by a position angle defined in the conventional way that angles are positive from north to east. A better control of the slit position is possible by aligning it along two bright sources in the field-of-view. Two gratings are available as diffraction elements for low-resolution and medium-resolution spectroscopy. The final spectral resolving power of the instrumental setup (Sect. 3.1), depends on the width of the slit, the kind of grating, and the observation wavelength.

In spectroscopy below $2.2 \mu\text{m}$ ($22\,000 \text{ \AA}$), the sky background emission is mainly resolved into the OH lines. Consequently, the photon noise from the sky background is low between the lines so that read noise becomes a more dominant factor. At low resolution, integration times above 60 s are sufficient to reach the background-limited case. At medium resolution, longer integration times are necessary. But the effects of hot pixels and cosmic rays also increase with integration time. The most suitable choice of integration times depends on the particular observation program. Integration times recommended by the ISAAC user manual are shown in Table 1.

In analogy to the on-off imaging technique, a series of object frames is taken at alternating positions along the slit. The positions are defined by a nod throw plus a small random offset so that the spectra at the two nodded positions do not overlap. The series is usually used for removing the sky by double sky subtraction. This means that both, positive and negative differences, are computed by subtracting the frames at one position from the frames at the other position and vice versa. Before the subtracted frames are aligned and added up, they have to be corrected for distortion which occurs along both, the spatial and the spectral axis.

Like for imaging observations, darks, flats, and standard star frames, are provided by the ISAAC calibration plan. Arc spectra of xenon and argon lamps are additionally observed for wavelength calibration. For medium-resolution spectra, wavelength calibration can alternatively be done, using the atmospheric OH lines contained in the object frames themselves. At low resolution, the numerous OH lines are blended so that the arc spectra provide the more reliable calibration.

The one-dimensional spectra are extracted from the reduced two-dimensional images by tracing the spectrum of a certain spatial region along the spectral axis. The S/N of the spectrum can be improved by averaging a number of lines of pixels within a spatial extraction aperture.

Spectra of standard stars are required for flux calibration and for removing telluric lines. The standard star frames are reduced like the object frames, and spectra are extracted using the same apertures as for the object spectra. It is possible to use the same star as flux and telluric standard. Preferentially, telluric standards are main-sequence stars of type A0, since they have a black body continuum and nearly no lines at NIR wavelengths. Alternatively, it is possible to use early-type G stars, for which the pure telluric spectrum can easily be recovered from intrinsic stellar lines by fitting a template of the well-known solar spectrum. The object spectrum is divided by the telluric spectrum after the line strengths have been matched by a suitable scaling. The standard star for flux calibration is treated in the same way before it is fitted with a black body or template spectrum, scaled to the known magnitude of the standard star. This results in a sensitivity function which can be applied to the object spectrum for flux calibration.

Table 2: Summary of the NIR observations for I Zw 1 carried out with ISAAC at the VLT in summer 2001. Column 1: Observation mode marked as BB-I for broad-band imaging, LR-S for low-resolution spectroscopy, and MR-S for medium-resolution spectroscopy, Column 2: Target (position angle of the long-slit in the case of the spectroscopic data), Column 3: Filter name and central wavelength [μm], Column 4: Date of observations, Column 5: Detector integration time (DIT), Column 6: Number of exposures pre-averaged on the chip (NDIT), Column 7: Number of exposures stored (NEXP), Column 8: Conditions of air mass during the observations.

Mode	Target	Filter	Date	DIT [s]	NDIT	NEXP	Air Mass
BB-I	I Zw 1	<i>J</i> , 1.250	2001-08-19	6.000	10	5	1.26
	GSPC S234-E	<i>J</i> , 1.250	2001-08-19	3.550	3	5	1.33–1.34
	I Zw 1	<i>H</i> , 1.650	2001-08-19	6.000	10	5	1.25–1.26
	GSPC S234-E	<i>H</i> , 1.650	2001-08-19	3.550	3	5	1.34–1.35
	I Zw 1	<i>Ks</i> , 2.160	2001-08-19	3.545	20	5	1.25
	GSPC S234-E	<i>Ks</i> , 2.160	2001-08-19	3.550	3	5	1.35–1.36
LR-S	I Zw 1 (0°)	<i>SK</i> , 2.200	2001-07-02	60.000	1	30	1.34–1.28
	HD 166224	<i>SK</i> , 2.200	2001-07-02	5.000	6	2	1.44
	HD 166224	<i>SK</i> , 2.200	2001-07-02	5.000	6	2	1.16
	SAO 92129	<i>SK</i> , 2.200	2001-07-02	40.000	1	8	1.23
	I Zw 1 (43°)	<i>SK</i> , 2.200	2001-09-22	60.000	1	30	1.33–1.27
	SAO 92128	<i>SK</i> , 2.200	2001-09-22	3.550	5	8	1.40–1.38
	SAO 92129	<i>SK</i> , 2.200	2001-09-22	10.000	4	8	1.24–1.23
	I Zw 1 (43°)	<i>SH</i> , 1.650	2001-09-22	70.000	1	24	1.25–1.27
	SAO 92128	<i>SH</i> , 1.650	2001-09-22	3.550	5	8	1.29–1.30
	SAO 92129	<i>SH</i> , 1.650	2001-09-22	40.000	1	8	1.23–1.22
MR-S	I Zw 1 (0°)	<i>SK</i> , 2.434	2001-08-02	200.000	1	8	1.28–1.32
	HD 3379	<i>SK</i> , 2.434	2001-08-02	5.000	6	2	1.45–1.46
	SAO 92128	<i>SK</i> , 2.434	2001-08-02	40.000	1	8	1.42–1.44

4 ISAAC Observations of I Zw 1

The NIR program for I Zw 1 was carried out with ISAAC at the Very Large Telescope in summer 2001. A complete list of all relevant observations is presented in Table 2. The imaging observations include broad-band imaging in the *J*-, *H*-, and *Ks*-bands. The spectroscopic observations are done with the $1''$ -wide slit in low-resolution mode, using the *SH*- and *SK*-filters which are the spectroscopic order-sorting equivalents of the imaging broad-band *H*- and *Ks*-filters. This configuration provides resolutions of $R_s \approx 500$ at $1.65 \mu\text{m}$ and $R_s \approx 450$ at $2.16 \mu\text{m}$. The medium-resolution grating was used in combination with the $0''.6$ -wide slit and the *SK*-filter, which gives $R_s \approx 4400$. All observations are complemented with exposures of photometric and/or telluric standard stars.

The data are reduced by means of the tools provided by the software packages IRAF (Image Reduction and Analysis Facility) and DPUSER. IRAF is developed and maintained at the National Optical Astronomy Observatories (NOAO) in Tucson, Arizona (USA), and

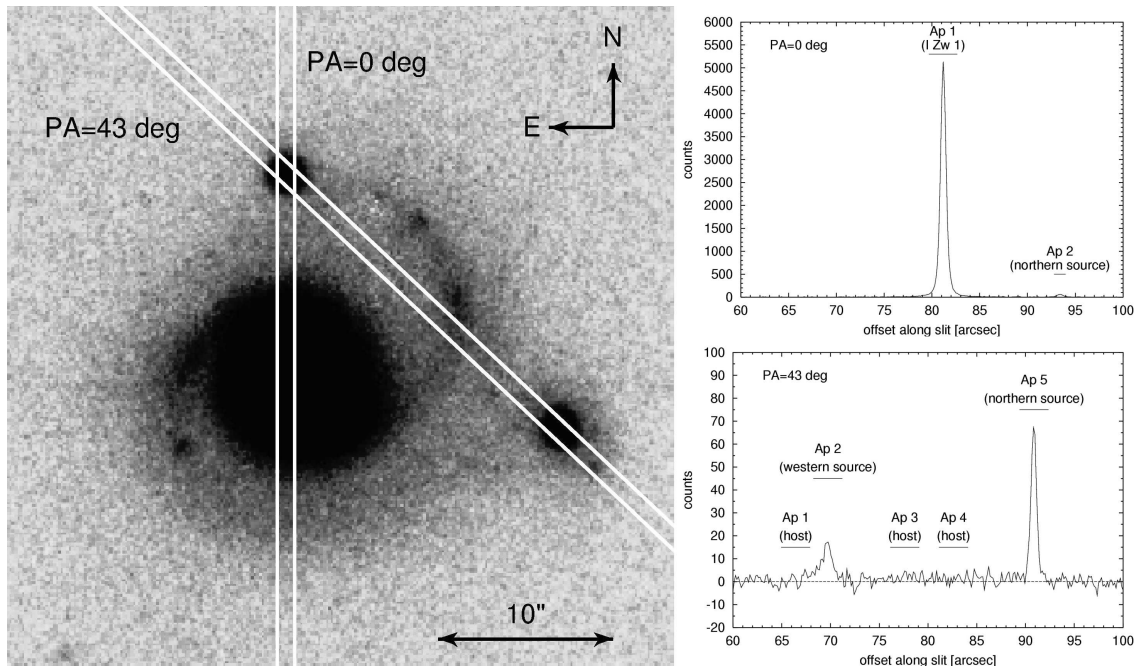


Figure 5: ISAAC J-band image of I Zw 1 overlaid with the two slit settings used for the ISAAC long-slit spectroscopy. The slit for $PA = 0^\circ$ includes the QSO of I Zw 1 and the northern source, the slit for $PA = 43^\circ$ the northern source and the likely western companion. The panels on the right-hand side show cuts along the spatial axes of the respective slits. Several apertures used for the extraction of the one-dimensional spectra are marked.

available at <http://iraf.noao.edu>. DPUSER is written by Dr. Thomas Ott and available at <http://www.mpe.mpg.de/~ott/dpuser/index.html>.

4.1 Spectroscopy

The long-slit spectroscopy for I Zw 1 includes observations for two slit settings at position angles of $PA = 0^\circ$ and $PA = 43^\circ$ (see Table 2). These settings are indicated in Fig. 5 together with cuts along the spatial axes of the spectra. The slit at position angle $PA = 0^\circ$ contains the I Zw 1 QSO nucleus and the northern source, the slit at position angle $PA = 43^\circ$ the western companion and the northern source.

4.1.1 Data Reduction

As described in Sect. 3.3, the telescope is nodded along the slits to obtain a series of exposures with object spectra at different positions. Besides the standard method of double sky subtraction (see Sect. 3.3), the procedures of data reduction are adapted to the particular data in the following way:

- The flat field provided by the ISAAC reduction pipeline is taken for flat fielding of the sky-subtracted frames.
- The distortion is corrected using a modified version of an IRAF script kindly provided by Dr. Richard Davies. In this script, the distortion along the spectral axis is

determined from the object spectra. The distortion along the spatial axis is traced via the atmospheric OH lines. At the same time the spectral axis is calibrated in wavelengths, using the known line positions of xenon and argon in the provided arc-frames. The solutions for the distortion and dispersion correction result in a transformation matrix which is applied to the sky-subtracted frames.

- The final two-dimensional spectra are obtained by median-combining the corrected and aligned frames.
- One-dimensional spectra are extracted at interesting regions (right panels in Fig. 5). The S/N is improved by averaging over suitable spatial apertures.

4.1.2 Telluric Correction and Calibration

The exposures of the photometric and telluric standard stars of the different long-slit observation-runs are reduced parallel to the object exposures. The same aperture sizes are used for the extraction of the spectra. The mean telluric spectra are obtained as the mean of all telluric standard star spectra available for each run. They are cleaned from the continuum slope and from the spectral lines of the telluric standard star by fitting the respective stellar spectrum from the Pickles stellar spectral flux library (Pickles 1998). Finally, the object spectra and the spectra of the photometric standard stars are divided by the scaled and shifted telluric spectra to remove telluric lines and the fingerprint of the filter curve. All the observational settings for ISAAC spectroscopy on I Zw 1 make use of A0 main-sequence stars as telluric standards. Although this stellar type is usually used for telluric corrections because of its small number of absorption lines, the *SH*- and *SK*-filters contain a number of higher-series Br absorptions and a Br γ absorption, respectively. Partially, these lines remain as artefacts when dividing by the template spectrum. Such artefacts will be pointed out in the analysis.

For the final photometric calibration, the cleaned spectra of the standard stars are used to determine the sensitivity function. By means of the IRAF task *STANDARD*, the spectra are integrated over calibration bandpasses. The flux in each bandpass is obtained from a blackbody model parameterized by the known magnitudes and spectral types of the calibration stars. Based on the list of bandpass information for each standard star, the IRAF task *SENSFUNC* is used to fit a mean sensitivity function provided as a spectrum-like one-dimensional image. The final step of flux calibration is done with the task *CALIBRATE* which divides the spectra by the sensitivity spectrum.

4.1.3 Spectral Quality and Resolution

As determined from the FWHM of the arc lines for each observing run, the final spectral resolution of the low-resolution spectra is similar to 40 \AA ($\sim 570 \text{ km s}^{-1}$) for the *SK*-filter and to 30 \AA ($\sim 545 \text{ km s}^{-1}$) for the *SH*-filter. All spectra discussed below are smoothed to resolutions of 55 \AA ($\sim 750 \text{ km s}^{-1}$) for the *SK*-filter and 38 \AA ($\sim 690 \text{ km s}^{-1}$) for the *SH*-filter, in order to improve the S/N.

There is no global measure for the S/N of the spectra, as it depends on the detailed extraction apertures and further reduction procedures. It also varies along the dispersion axis in the final one-dimensional spectra. The spectra extracted for the host galaxy, using the apertures *Ap 1*, *Ap 3*, and *Ap 4* in the lower right panel of Fig. 5, are dominated by

noise and not considered in the further analysis. Useful spectra are obtained for the bright nucleus of I Zw 1 (*Ap 1* in the upper right panel of Fig. 5), the northern source (*Ap 2* and *Ap 5* in the upper and lower right panels of Fig. 5, respectively), and the likely companion galaxy (*Ap 2* in the lower right panel of Fig. 5). Their respective S/N characteristics are discussed in the individual sections, along with the analysis of the results.

The medium-resolution spectra are characterized by a S/N, insufficient for analysis purposes. They were intended for an analysis of the ^{12}CO (2-0) and ^{12}CO (3-1) bandheads, which are redshifted close to the long-wavelength limit of the *SK*-filter in the case of I Zw 1. The limited spectral coverage of 1220 Å at medium resolution made it necessary to use a grating central wavelength of 24 343 Å. The corresponding spectral range overlaps with the declining sensitivity of the *SK*-filter and is additionally influenced by the increasing thermal background.

4.2 Imaging

Since the field around I Zw 1 is uncrowded, there is no need for separate sky exposures (Sect. 3.2.2). Sky subtraction is done by using the sequence of object exposures with shifted object positions on the detector array.

4.2.1 Data Reduction

The image reduction refers to two different reduction cycles, *Cycle A* and *Cycle B*, both based on different combinations of standard procedures. In order to avoid photometric offsets as a possible consequence of the different reduction methods, the color analysis in Sect. 5.5 is based on the *J*-, *H*-, and *Ks*-band images consistently reduced in *Cycle B*. The independent profile analysis Sect. 5.6 refers to the *J*-band image of *Cycle A*. A check with *Cycle B* image is shown there.

In detail, the reduction procedure applied to the *J*-band image in *Cycle A* is the following:

- Flat-fielding is omitted, as the flat-field shows variations of less than 1%, measured in several 5×5 pixel boxes. This prevents from the additional noise introduced during the division step.
- Sky-subtraction is done by subtracting the object frames from each other, using all possible permutations.
- The sky-subtracted and aligned object frames of the *J*-band observations are combined by using a median algorithm. It has the advantage to effectively remove negative imprints resulting from a sky-subtraction based on shifted object frames.

In *Cycle B*, the images are reduced in the following way:

- The flat-field is obtained by subtracting the first from the last frame of the sequence of available twilight flats. It is normalized by dividing the flat-field by its median. Dead pixels, identified as those pixels with counts larger than two or smaller than zero, are corrected by interpolating from a boxcar average. The final flat-field results from a second normalization of the dead-pixel corrected flat-field.

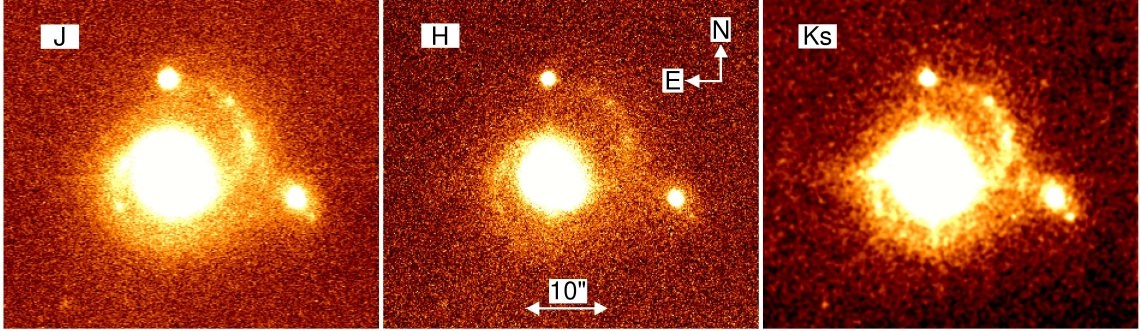


Figure 6: ISAAC J -, H -, and Ks -band images of I Zw 1, resulting from the reduction in Cycle B. The images are adjusted to the maximum common angular resolution of $0''.62$. The color scaling is arbitrarily set to pronounce the prominent features in each individual image.

- The sky is computed from the median of the object frames after having them adjusted to a zero offset. The latter is done by subtracting the median pixel value from each frame.
- A dead pixel list is obtained from the median sky, using the DPUSER routine DPIX-CREATE. This routine allows to identify these pixel values deviating by more than a certain threshold from the mean pixel values displayed by the sky frame. For a final dead pixel list, this list is added to the list resulting from the flat-field.
- The sky-subtracted, dead-pixel corrected, and flattened object frames are aligned and combined, using an average algorithm.

4.2.2 Calibration

GSPC S234-E from the catalog of faint NIR LCO/Palomar NICMOS standards (Persson et al. 1998) with magnitudes of $m_J = 12.464 \pm 0.011$, $m_H = 12.127 \pm 0.008$, and $m_K = 12.070 \pm 0.007$ is observed as a photometric standard star for all three bands. The star exposures are reduced identically to the respective object exposures in *Cycles A* and *B*. In *Cycle A*, the flux of the standard star is measured in the sky-subtracted frames before image combination. This results in five measurements for the star at its different positions on the detector array. Since the star is shifted along similar positions like the object, the small standard deviation of the five flux measurements provides an independent test that the errors introduced by omitting the flat-fielding are small. The average of the five flux measurements is used for the final calibration. In *Cycle B*, photometry of the standard star is only done in the final combined image.

4.2.3 Image Quality and Photometric Significance

Calibration factors and measures of quality (see Sect. 3.1) for the reduced images of I Zw 1 are listed in Table 3. The J -, H -, and Ks -band images are shown in Fig. 6. All images are convolved to the maximum common angular resolution of *Cycle B* as determined by the J -band resolution of $0''.62$.

The four-spiked feature in the Ks -band image is a result of stray light from the mounting of the secondary mirror of the ISAAC unit telescope UT1. This effect becomes no-

Table 3: Characteristics of the J -, H -, and Ks -band images obtained from the reductions of Cycles A and B. Column 1: Name of image (the Ks -band image convolved to the lower angular resolution of the J - and H -band images is listed additionally), Column 2: Extinction corrected zero point as defined in Sect. 3.2.3, Column 3: FWHM of the assumed Gaussian PSF, Column 4: Limiting magnitude at 1 σ - and 3 σ -levels of the background noise, Column 5: Limiting surface-brightness at 1 σ - and 3 σ -levels of the background noise.

Image	ZP_c	FWHM ["]	$m_{\text{lim}}^1 \sigma$ ($m_{\text{lim}}^3 \sigma$) [mag]	$\mu_{\text{lim}}^1 \sigma$ ($\mu_{\text{lim}}^3 \sigma$) [mag arcsec ⁻²]
<i>Cycle A</i>				
J	25.11	0.67	26.7 (25.5)	22.5 (21.3)
<i>Cycle B</i>				
J	25.11	0.62	26.6 (25.4)	22.4 (21.2)
H	24.75	0.62	24.7 (23.5)	20.6 (19.4)
Ks	24.24	0.36	24.4 (23.2)	20.2 (19.1)
$Ks^{\text{FWHM}(J,H)}$	24.24	0.62	25.9 (24.7)	21.8 (20.5)

ticeable in the case of exceptionally bright sources like the QSO nucleus of I Zw 1. The I Zw 1 nucleus is saturated in the H - and Ks -band images which are, thus, only used for photometry on the host galaxy and the two bright sources to the north and to the west. In these measurements, the regions contaminated by stray light are avoided. The brightest pixels in the J -band image could be slightly saturated and in the critical region of detector non-linearity. Since the J -band image of *Cycle A* is used for the profile analysis (Sect. 5.6), the brightest pixels are edited, using the correction formula $f_{\text{true}} = f_{\text{obs}} + 4.75 \times 10^{-11} f_{\text{obs}}^3$. This formula taken from the ISAAC reduction guide is reported as untested. It results in a very small correction for the brightest nuclear pixels and it is uncertain whether a bias remains. The possible saturation or non-linearity has a negligible effect on the profile analysis as it is based on Gaussian fits adjusted to the wings of the central luminosity peak.

The photometric calibration of the images is tested for consistency with previous photometry in Table 4. The photometry in the ISAAC images is done by integrating over apertures with diameters of 2'', 3'', 5'', and 10'' centered on the QSO of I Zw 1, the northern source, and the western source. The mean photometric error is given as ± 0.1 mag. This estimate is derived from the photometric variations in the sky-subtracted frames before image combination. The magnitudes are compared to the measurements presented by Eckart et al. (1994) and taken from the 2MASS All-Sky Point Source Catalog (PSC) (available at the IPAC Infrared Science Archive (IRSA), Caltech/JPL, via <http://irsa.ipac.caltech.edu>).

As all objects are treated as point sources, the magnitudes of the northern and the western source are affected by a bias for larger aperture sizes (see superscript a in Table 4). The magnitudes of the northern source are biased by contributions from the underlying host galaxy of I Zw 1. The same is true for the magnitudes of the western source, in which case the circular apertures additionally misrepresent the elongated shape. The point source approach is, nevertheless, chosen to provide consistency with the approach used for the literature data. The photometric method on which the 2MASS data are based is a pure

point-source approach which becomes unreliable in the case of an extended source (see the 2MASS All-Sky Data Release Explanatory Supplement⁷). As described in this document, the basic aperture taken for the measurements is 4''-wide. Photometry in 3''- to 14''-wide apertures sampled in steps of 1'' is used to determine whether a curve-of-growth correction is necessary. This means that the 2MASS data are comparable to ISAAC magnitudes measured in apertures of sizes of about 5'' and larger.

The photometric systems of the 2MASS data and the data presented by Eckart et al. (1994) differ from the LCO/Palomar NICMOS system used for the calibration of the ISAAC data. The 2MASS-to-LCO transformation is given by the appropriate transformation terms from Equation (3.6). The Eckart et al. (1994) data are observed with the MPE SHARP camera at the New Technology Telescope (NTT) of the European Southern Observatory (ESO) and flux-calibrated, using HD 1160 as a photometric standard. Since the transformation terms for this particular photometric system are undetermined, the standard Bessell & Brett system is assumed. Since the transformation depends on color terms, it can only be done for those data providing the full *JHKs* color information. The data transformed to the LCO system are marked by the superscript *LCO* in Table 4. However, as shown in Table 4, the respective transformations change the magnitudes by less than 0.01 mag for the colors of I Zw 1. In particular, the differences between the *K*-filter used by Eckart et al. (1994) and the *Ks*-filter of the LCO system are small. Differences of less than ± 0.1 mag in extreme cases are verified by a study comparing the *K*- and *Ks*-magnitudes of stars with a wide spread of colors (Persson et al. 1998). Since this is below the accuracy level of about ± 0.1 mag of the photometric measurements, the distinction between *K* and *Ks* will be omitted for the remaining analysis of the imaging data.

The basic results provided by the comparison in Table 4 are the following:

- The ISAAC *J*-band magnitudes derived from the reductions in *Cycle A* and *B* agree within the mean photometric error of ± 0.1 mag.
- For all available common measurements, the 2MASS and the ISAAC magnitudes agree, while the data by Eckart et al. (1994) show a tendency towards about 0.3 mag to 0.5 mag brighter magnitudes. This could be a manifestation of the NIR variability of I Zw 1 (see e.g. Neugebauer et al. 1989; Neugebauer & Matthews 1999). The observations reported by Eckart et al. (1994) observations were done in 1992, almost ten years before the ISAAC and 2MASS observations. However, a systematic offset is suggested by the fact that the *K*-band magnitudes of the northern source show a similar offset.
- As expected, the 2MASS magnitudes of the western source agree with the ISAAC magnitudes measured in 5''-wide apertures. The same is true for the *J*- and *H*-band magnitudes of the northern source.
- Aperture diameters of 5'' to 10'' are required to reproduce the *J*-band flux of the I Zw 1 nucleus and the *K*-band flux of the northern source. The need for a slightly larger aperture diameter here is likely caused by the method of photometry applied to the 2MASS data. It could also be a manifestation of a slight bias in the central nuclear pixels of the ISAAC *J*-band image caused by non-linearity or saturation.

⁷http://www.ipac.caltech.edu/2mass/releases/allsky/doc/sec4_4c.html

Table 4: Photometry for I Zw 1, the northern and the western source. The mean photometric error of the ISAAC magnitudes is estimated as ± 0.1 mag. An extrapolated magnitude of the I Zw 1 host galaxy without contribution from the QSO is added for completeness. The latter is derived from the average of several measurements on the host disk, integrated over apertures of $3''$ in diameter, which are extrapolated to a larger aperture corresponding to the assumed diametrical size of about $24''$ of the disk. 2MASS magnitudes and the magnitudes reported by Eckart et al. (1994), (E94), are added for comparison. Using the method described in the text, these data are also shown after transformation to the LCO/Palomar NICMOS system of the ISAAC data as indicated by the superscript LCO. Column 1: Photometric target, Column 2: Data source, Column 3: Diameter of the photometric aperture, Columns 4 to 7: J -, H -, and K_s -band magnitudes from the Cycle A and Cycle B reductions

Target	Data	Aperture [$''$]	$m_J^{\text{Cycle A}}$ [mag]	$m_J^{\text{Cycle B}}$ [mag]	$m_H^{\text{Cycle B}}$ [mag]	$m_{K_s}^{\text{Cycle B}}$ [mag]
I Zw 1	ISAAC	2.0	12.9	12.8	(11.8) ^b	(11.0) ^b
		3.0	12.7	12.7	(11.7) ^b	(10.9) ^b
		5.0	12.6	12.5	(11.5) ^b	(10.8) ^b
		10.0	12.4	12.4	(11.4) ^b	(10.7) ^b
	2MASS		12.45	12.45	11.49	10.35
	2MASS ^{LCO}		12.44	12.44	11.48	10.36
	E94	5.0	12.1	12.1	11.0	9.9
E94 ^{LCO}	5.0	12.0	12.0	11.0	9.9	
Northern source	ISAAC	2.0	16.1	16.0	15.4	15.2
		3.0	16.0	15.9	15.3	15.1
		5.0	15.9 ^a	15.8 ^a	15.2 ^a	15.0 ^a
		10.0	15.6 ^a	15.5 ^a	15.0 ^a	14.5 ^a
	2MASS		15.90	15.90	15.26	14.97
	2MASS ^{LCO}		15.91	15.91	15.26	14.98
	E94					~ 14.3
Western source	ISAAC	2.0	17.3	17.3	16.5	16.1
		3.0	17.0	17.0	16.2	15.8
		5.0	16.6 ^a	16.6 ^a	15.8 ^a	15.4 ^a
		10.0	16.0 ^a	16.0 ^a	15.2 ^a	14.8 ^a
	2MASS		16.72	16.72	16.11	15.88
2MASS ^{LCO}		16.73	16.73	16.11	15.89	
I Zw 1 host	ISAAC	24.0		13.2 ± 0.3	12.4 ± 0.3	12.0 ± 0.3

^a Possible bias for larger aperture sizes (see text for details)

^b Saturated (see text for details)

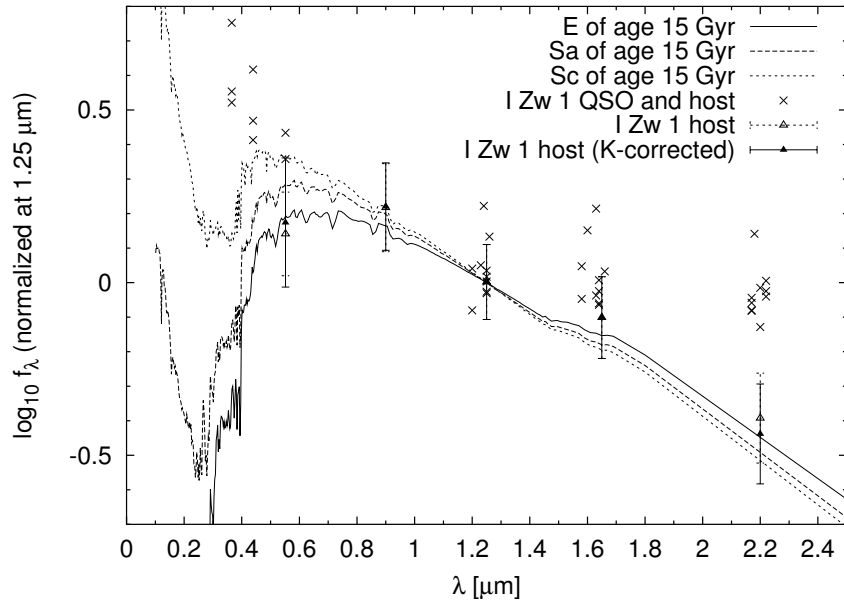


Figure 7: Comparison of the SEDs of the 15 Gyr old model galaxies used by Poggianti (1997) for determining K -correction terms (lines), the global SED of I Zw 1 (QSO plus host galaxy) as taken from NED⁸ (crosses), and the original (open triangles) and K -corrected (filled triangles) SED of the I Zw 1 host only. The K -correction makes use of the terms applying to an Sa galaxy at $z = 0.06$ as provided by Poggianti (1997). The method for deriving the SED of the I Zw 1 host galaxy is described in the text.

4.3 The K -Correction for I Zw 1

In order to compare the magnitudes measured for I Zw 1 with data from local galaxies, it is necessary to apply the K -correction (Sect. 3.2.3). Several authors provide K -correction terms based on predictions from model spectral energy distributions (SEDs) for standard types of galaxies. The terms differ depending on the applied models and the assumed filter response curves. Two solutions for I Zw 1 are compared. They are based on data provided by Poggianti (1997) and by Fioc & Rocca-Volmerange (1999). Poggianti (1997) provides K -corrections for models for E, Sa, and Sc galaxies from ultra-violet to infrared bands. The K -corrections applying to the Sa and Sc models at a redshift of $z = 0.06$ are listed in Table 5. The model SEDs are plotted in Fig. 7. This plot also shows the SED of I Zw 1 including contributions from the QSO and the host galaxy. The corresponding data are taken from the NASA/IPAC Extragalactic Database⁸ (NED). The graph is complemented with the SED of the host galaxy only, plotted before and after applying the K -correction suggested for an Sa galaxy at $z = 0.06$ by Poggianti (1997). The NIR fluxes are derived as explained in Table 4. For comparison with the model SEDs which are based on the Bessell & Brett photometric system, the disk magnitudes are transformed into this system via Equations (3.6). Magnitudes are converted into fluxes in Jansky, using $f_\nu = 10^\epsilon 10^{-0.4m}$, where 10^ϵ is the respective flux zero point of the Bessell & Brett system, given by $\epsilon_J = 3.207$, $\epsilon_H = 3.021$, and $\epsilon_K = 2.812$ (<http://www.supernova.lbl.gov/~aldering/UNITITS>). The specific flux f_λ follows from the relation $f_\nu d\nu = f_\lambda d\lambda$ which results in $\log f_\lambda =$

⁸<http://nedwww.ipac.caltech.edu>

Table 5: K -correction terms for the redshift of I Zw 1 according to Poggianti (1997) and Fioc & Rocca-Volmerange (1999). The corrections $KC_{(A-B)}$ have to be subtracted from the measured colors to derive the colors in the rest frame ($(A - B)_{\text{rest}} = (A - B)_{\text{obs}} - KC_{(A-B)}$).

SED	KC_V	KC_I	KC_J	KC_H	KC_K	$KC_{(J-H)}$	$KC_{(H-K)}$
Poggianti 1997							
Sa (15 Gyr)	+0.087	+0.008	-0.034	-0.016	-0.089	-0.018	+0.073
Sc (15 Gyr)	+0.048	-0.004	-0.042	-0.024	-0.091	-0.018	+0.067
Fioc & Rocca-Volmerange 1999							
E, S0, Sa, Sb, Sc			-0.018	-0.006	-0.168	-0.012	+0.162

$\log(f_{\nu}c/\lambda^2) + C$, where C is a constant depending on the chosen units. The V - and I -band data are derived from a new reduction of archived imaging data, obtained with the $F555W$ and the $F814W$ filters of the Hubble Space Telescope. These images are flux calibrated as described in the Wide Field and Planetary Camera 2 Instrument Handbook, using the calibration parameters given in the respective image headers. The handbook also provides terms for the transformation into the Johnson photometric system. These transformations are tabulated for typical colors of main sequence O5 to M6 stars. In particular, the $F814W$ - and the Johnson I -filters do not match well, so that the transformation strongly depends on the assumed spectral type. For the I Zw 1 host, a spectral slope, similar to a late-type M6 star, as suggested by the JHK colors, is assumed. This assumption could induce a systematic source of error for the calibration.

The K -corrected SED of the I Zw 1 host is basically consistent with the models of the 15 Gyr-old Sa and Sc galaxies used by Poggianti (1997). This suggests that this kind of K -correction is suitable for the I Zw 1 host spectrum. By comparing the original to the K -corrected SEDs of the I Zw 1 host, it becomes evident that the effects of the K -correction are small for the relatively low redshift of I Zw 1, in particular at NIR wavelengths. Additionally, the different model SEDs exhibit very similar slopes in the NIR, so that the K -corrections are only weakly influenced by the Hubble type. Nevertheless, the K -correction is important for the $(H - K)$ color. The $(J - H)$ correction is given by -0.018, the mean $(H - K)$ correction of the Sa and Sc models is 0.070.

Fioc & Rocca-Volmerange (1999) present linear relations between the K -correction terms and redshift. They are given for all galaxies of types E up to Im and valid for $z < 0.1$ (see their Table 1). The corrections derived for the relevant models at the redshift of I Zw 1 are shown in the lower part of Table 5. Also in the models used by Fioc & Rocca-Volmerange (1999), the corrective terms at NIR wavelengths are equal for the galaxy types E through Sc. The corrections result in slightly redder colors than the corrections suggested by Poggianti (1997).

The compromise solution of the Poggianti (1997) and Fioc & Rocca-Volmerange (1999) models results in a K -correction of $KC_{(J-H)} \approx -0.015$ and $KC_{(H-K)} \approx 0.12$ for the I Zw 1 host. The K -correction is mostly ignored in previous studies about I Zw 1. This is acceptable, since the corrective terms are small when compared to the uncertainties inherent to the correction models and the photometric calibration. But the K -correction implicates

a systematic shift in colors, which is particularly significant in $(H - K)$. Therefore, the photometric data will be left uncorrected, but the K -correction will be used to reveal basic trends in the NIR colors.

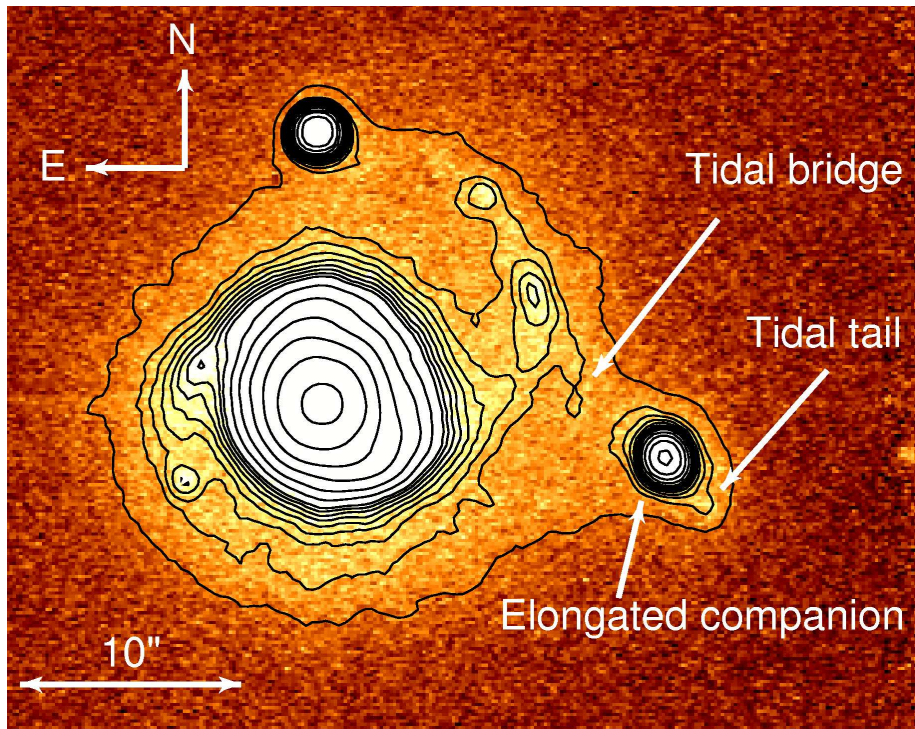


Figure 8: The ISAAC J -band image of I Zw 1 obtained from reduction Cycle B. The image has an angular resolution of about $0''.62$ (see Sect. 4.2.3 and Table 3). The contour levels are at 3σ , 5σ , 6σ , 7σ , 8σ , 9σ , 10σ , 11σ , 12σ , 15σ , 20σ , 30σ , 50σ , 100σ , and 1000σ . This corresponds to surface brightnesses in mag arcsec^{-2} of 21.20, 20.65, 20.45, 20.29, 20.14, 20.01, 19.90, 19.80, 19.70, 19.46, 19.15, 18.71, 18.15, 17.4, and 14.9. The tidal features suggesting an interaction with the western galaxy are indicated.

5 Results

In this section, the new results obtained from the ISAAC imaging and spectroscopy observations of I Zw 1 are presented and compared to published results. The section includes the discussion of the J -band image, the analysis of the ISAAC spectra for the I Zw 1 nucleus and for the northern and the western source, the investigation of the NIR colors displayed by the I Zw 1 host galaxy and the western source, and the decomposition of the I Zw 1 host. The J -band imaging together with the decomposition is partly published in Scharwächter et al. (2003).

5.1 The J -Band Image

Fig. 8 shows the J -band image obtained from the reduction procedure in Cycle B. The J -band image, as the one least affected by saturation and stray-light features, shows the I Zw 1 host and the two nearby objects at a spatial resolution of $0''.62$.

Consistent with previous imaging observations (e.g. Surace et al. 2001; Canalizo & Stockton 2001), the J -band image reveals the known two-armed spiral of the I Zw 1 host. As typical of observations at NIR wavelengths, the spiral arms as well as the knotty chain of H II regions along the arms have less contrast than in optical images. This is caused by mainly two facts. On the one hand, the extinction by dust is less significant at NIR

wavelengths. On the other hand, the NIR traces the emission from a late stellar population of G to M stars, and not from the hot OB stars, predominant in the star forming regions along the spiral arms.

The northern source remains unresolved at the resolution of the J -band image. This indicates that the source could indeed be a projected foreground star. A more detailed analysis of the properties of the northern source is presented in Sect. 5.3 on the basis of the new spectral data.

In contrast to the northern source, the western object seems to be involved in a tidal interaction with the I Zw 1 host. As known from major merger systems, the basic effect of tidal interactions between two galaxies is the formation of tidal bridges between the galaxies and tidal tails at the respective far ends of each galaxy (see also Sect. 7.1.2). Although much weaker than in major merger systems, a tidal bridge is present between the north-western spiral arm of I Zw 1 and the western source in Fig. 8. The western companion itself is elongated towards the I Zw 1 disk and also shows an indication for a tidal tail at its far end.

The likely tidal origin of the features in the interaction zone is consistent with the previous indications for an interaction with the companion, such as the small velocity difference between I Zw 1 and the companion or the extensions found in HI (Canalizo & Stockton 2001; Lim & Ho 1999, and Sect. 2.2).

5.2 The Nuclear Spectrum of I Zw 1

The nuclear K -band spectrum of I Zw 1 (Fig. 9) is dominated by the hydrogen recombination lines Pa α , Br δ , and Br γ and shows indications of the high-excitation coronal lines [Si VI] and [Al IX]. The spectrum is extracted in an aperture of $3''$ in diameter, centered on the I Zw 1 nucleus and smoothed to a resolution of 55 \AA ($\sim 750 \text{ km s}^{-1}$). As explained in Sect. 4.1.2, the spectrum contains a Br γ feature originating from the telluric line correction with an A0V telluric standard. It is just a matter of coincidence that this line mimics an [Al IX] line at the systemic velocity of I Zw 1.

The noise RMS is measured as $\sigma = 5 \times 10^{-17} \text{ erg s}^{-1} \text{ cm}^{-2} \text{ \AA}^{-1}$ or about 1.5% of the continuum level. Multiplied by the spectral resolution, this results in $3 \times 10^{-15} \text{ erg s}^{-1} \text{ cm}^{-2}$ as an estimate for the error, inherent to flux measurements. According to this estimate the Pa α , Br δ , and Br γ lines are detected at levels of more than 5σ . The two high-excitation lines [Si VI] and [Al IX] are marginally detected at levels of less than 4σ .

In comparison with the spectrum presented by Schinnerer et al. (1998), the flux densities in Fig. 9 are systematically smaller by a factor of about 1.3. The former is reported to be calibrated, by using the integrated flux densities given by Edelson & Malkan (1986). As also discussed in Eckart et al. (1994), the magnitudes given by Edelson & Malkan (1986) are, by about 0.1 mag to 0.2 mag, fainter than the ones derived by Eckart et al. (1994). By this, there is still an offset of about 0.2 mag to 0.3 mag between the magnitudes given by Edelson & Malkan (1986) and the new ISAAC and the 2MASS data (see Table 4). Therefore, the disagreement of the flux densities in the spectra is another manifestation of the magnitude offset discussed in (Sect. 4.2.3).

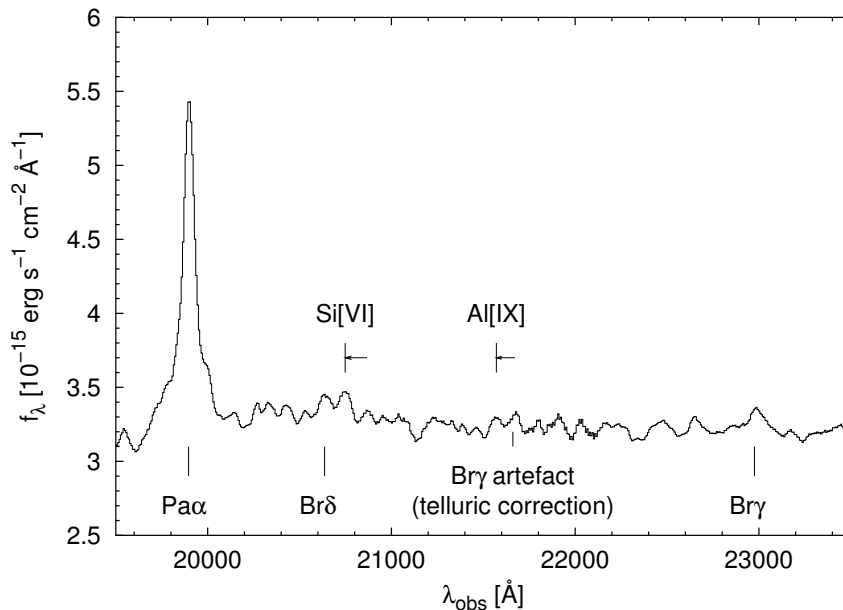


Figure 9: *Hydrogen emission lines and high excitation lines of ionized gas in the nuclear spectrum of I Zw 1 derived from the ISAAC spectroscopy runs. The spectrum is extracted with a 3''-wide aperture along the spatial axis and smoothed to a resolution of 55 Å ($\sim 750 \text{ km s}^{-1}$). The arrows pointing at the lines of [Si VI] and [Al IX] indicate the blueshifts with respect to the theoretical rest-wavelengths at the redshift of I Zw 1. The spectrum is affected by a small Br γ artefact originating from the telluric correction, based on the spectrum of an A0 star (see Sect. 4.1.2).*

5.2.1 Hydrogen Emission Lines

The hydrogen lines are centered at the systemic velocity of I Zw 1 and indicate a narrow profile with a broader underlying component. The comparison of the line profiles of the Pa α , Br δ , and Br γ emission is shown in Fig. 10. The line profile of Br δ has already been cleaned from blending with [Si VI]. The profiles are very similar and slight deviations are most probably due to the contamination of the low S/N Br δ and Br γ lines by residuals from the [Si VI] blending or from the telluric line correction.

The basic shape of the hydrogen emission lines suggests the need for a broad component in addition to the narrow component, typical of narrow-line Seyfert 1s. This agrees with findings by Véron-Cetty et al. (2004). They also report the need for a very broad Gaussian component with an FWHM of 5600 km s^{-1} in addition to a narrow Lorentzian component with an FWHM of 1100 km s^{-1} in order to obtain a good fit of the optical Balmer lines. Fig. 11 shows the two-component decomposition of the hydrogen lines based on a narrow and a broad Gaussian line profile. Providing the highest S/N, the Pa α line is used to determine the respective FWHMs of the Gaussian components by a non-linear least-square fitting. The resulting FWHMs are used to fit the total fluxes of the low S/N lines of Br δ and Br γ , the former having been cleaned from blending with [Si VI] beforehand. The fit results of this decomposition are listed in Table 6.

All three lines suggest a similar composition with a flux contribution of about 50% to 70% from the broad Gaussian component and of about 30% to 50% from the narrow component. However, fitting uncertainties and the low S/N of the Br lines prohibit detailed

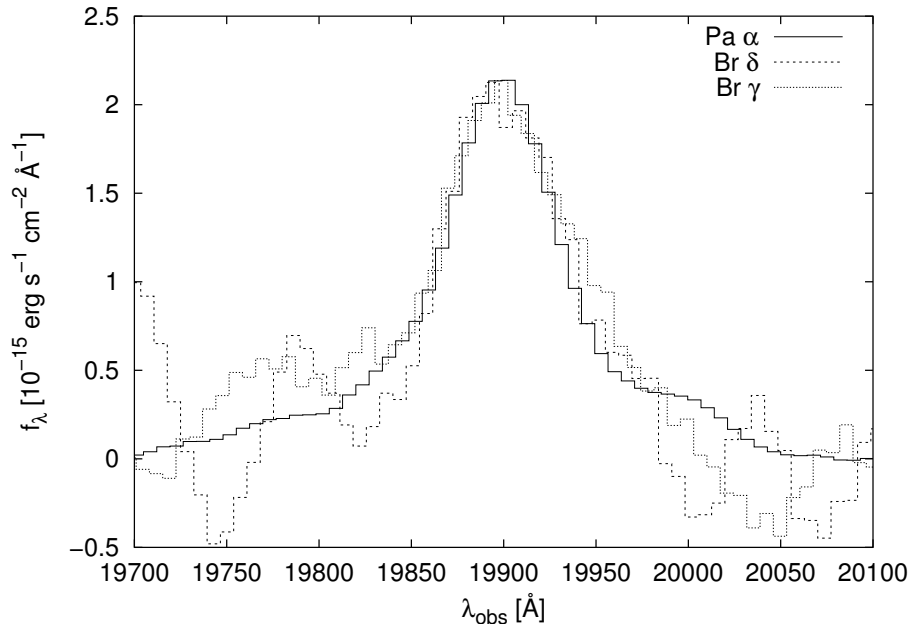


Figure 10: Comparison of the line shapes of the hydrogen recombination lines. The $Br\ \delta$ and $Br\ \gamma$ lines are shifted to the center and scaled to the peak flux of the $Pa\ \alpha$ line. The $Br\ \delta$ line is cleaned from the contamination by the neighboring $[Si\ VI]$ line.

conclusions, based on the two-component model. Likewise, a more complex decomposition for a direct comparison with the four-component optical spectra found for I Zw 1 (Véron-Cetty et al. 2004, and Sect. 2.2) is unfeasible.

Line ratios are only computed for the total line fluxes. This results in $Pa\ \alpha/Br\ \gamma \approx 12$ and $Pa\ \alpha/Br\ \delta \approx 13$. Assuming a *Case B* recombination⁹ in a hydrogen plasma of temperature $T_e = 10^4$ K and density $n_e = 10^4\ \text{cm}^{-3}$, theoretical calculations yield ratios of $Pa\ \alpha/Br\ \gamma \approx 12.07$ and $Pa\ \alpha/Br\ \delta \approx 18.34$ (Hummer & Storey 1987). The ratios found for the I Zw 1 hydrogen lines are similar to the ones expected for the typical conditions of H II regions. A consistent result for $Pa\ \alpha/Br\ \gamma$ is reported by Schinnerer et al. (1998), who interpret its typical value as an indication for low extinction towards the QSO nucleus. Their derived $Pa\ \alpha/Br\ \delta$ of about 76 (see Table 6), however, is much larger than the one resulting from the ISAAC measurements. The inconsistencies in the $Pa\ \alpha/Br\ \delta$ ratios probably originate from the $[Si\ VI]$ blending of the $Br\ \delta$ line. As the lower value, the new $Pa\ \alpha/Br\ \delta$ ratio is closer to the theoretical value.

5.2.2 Coronal Lines

In comparison with the previous spectrum by Schinnerer et al. (1998), the marginal detections at 20 748 Å and at 21 571 Å seem to coincide respectively with the blueshifted $[Si\ VI]$ and $[Al\ IX]$ lines reported by these authors. If the detections are real, their line positions correspond to blueshifts of about 1200 km s⁻¹ with respect to the systemic velocity of

⁹In *Case A*, any produced photon is assumed to immediately leave the plasma. In *Case B*, the photons are locally scattered, so that any Lyman photon finally results in a Lyman α and higher-series photons, the latter being radiated away without scattering.

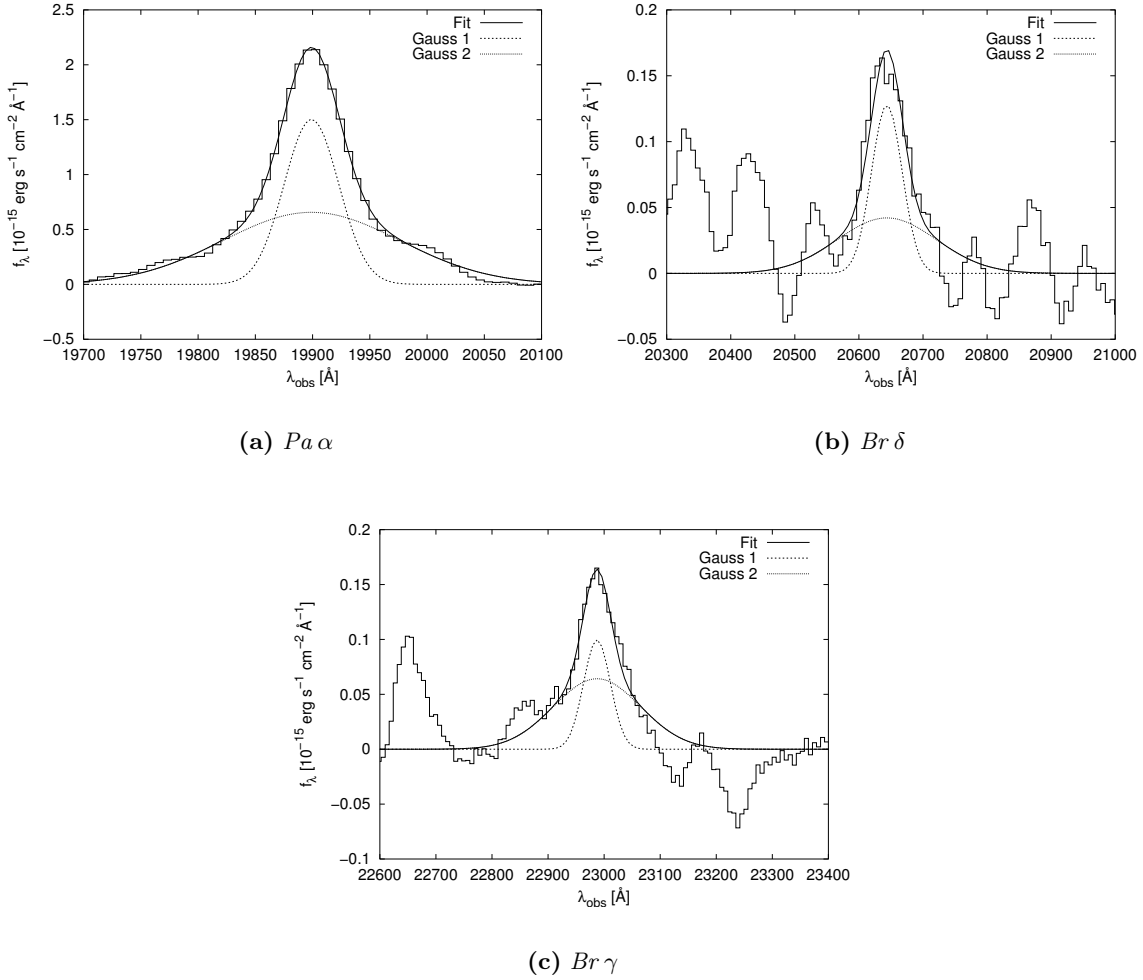


Figure 11: Decomposition of the hydrogen emission lines based on a model consisting of two Gaussian components. The FWHMs of the narrow and the broad Gaussian components are determined from fitting the high S/N $Pa \alpha$ line, which clearly shows a narrow shape with broad wings. These widths are used to subsequently fit the low S/N $Br \delta$ and $Br \gamma$ lines. Results of the fits are shown in Table 6.

Table 6: List of lines identified in the nuclear K-band spectrum of I Zw 1 (Fig. 9). Values in brackets are uncertain measurements only listed for completeness. Column 1: Line and rest wavelength, Column 2: Comment about the component of the line, Column 3: Gaussian FWHM, Column 4: Observed wavelength, Column 5: Flux measured from the ISAAC spectrum, Column 6: Flux published by Schinnerer et al. (1998).

Line	Component	FWHM ^a [km s ⁻¹]	λ_{obs} [Å]	Flux ^b [10 ⁻¹⁵ erg s ⁻¹ cm ⁻²]	Flux (Schinnerer et al. 1998) [10 ⁻¹⁵ erg s ⁻¹ cm ⁻²]
Permitted lines with narrow and broad components					
Pa α λ 18 756	narrow	1230		90	
	broad	3980		128	
	total		19899	218	284 \pm 12
Br δ λ 19 451	(narrow)	1230		8)	
	(broad)	3980		8)	
	total		20644	16	3.7 \pm 1.8
Br γ λ 21 661	(narrow)	1230		6)	
	(broad)	3980		12)	
	total		22987	18	26 \pm 8
Narrow forbidden lines with blueshift					
[Si VI] λ 19 634	blue	1230	20 748	< 12	3.5 \pm 1.8
(+H ₂ S(3) λ 19 576	systemic		\sim 20 769)		
[Al IX] λ 20 400	blue	1230	21 571	< 4	3.2 \pm 3.2
(+H ₂ S(2) λ 20 338	systemic		\sim 21 578)		

^a The spectral resolution is 750 km s⁻¹.

^b The 1 σ -error of the flux is 3×10^{-15} erg s⁻¹ cm⁻².

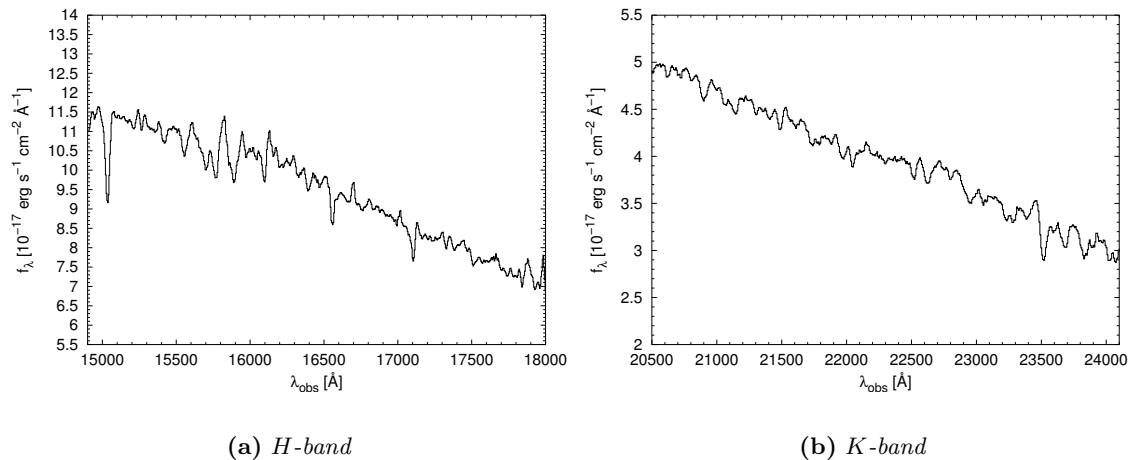


Figure 12: Spectra of the northern source. Both spectra are smoothed by 5 pixels to resolutions of 38 \AA ($\sim 690 \text{ km s}^{-1}$) and 55 \AA ($\sim 750 \text{ km s}^{-1}$) in *H* and *K*, respectively.

I Zw 1. This blueshift is similar to the one of 1350 km s^{-1} derived by Schinnerer et al. (1998).

According to Eckart et al. (1994), both lines are blended with H_2 emission found at the systemic velocity of I Zw 1. This blending comes from $\text{H}_2 \nu = 1 - 0 \text{ S}(3)$ for the blueshifted [Si VI] line and from $\text{H}_2 \nu = 1 - 0 \text{ S}(2)$ for the blueshifted [Al IX] line. The flux of $\text{H}_2 \nu = 1 - 0 \text{ S}(1)$ in I Zw 1 of $6.8 \times 10^{-16} \text{ erg s}^{-1} \text{ cm}^{-2}$ (Eckart et al. 1994) is below the detection limit of the ISAAC spectrum compared to the 1σ flux error of $3 \times 10^{-15} \text{ erg s}^{-1} \text{ cm}^{-2}$. Since the strengths of $\text{H}_2 \nu = 1 - 0 \text{ S}(3)$ and $\text{H}_2 \nu = 1 - 0 \text{ S}(2)$ are similar or lower than the strength of $\text{H}_2 \nu = 1 - 0 \text{ S}(1)$, the contributions to [Si VI] and [Al IX] should be negligible.

Véron-Cetty et al. (2004) speculate that the extremely blueshifted NIR coronal lines could originate from the two high-excitation narrow-line systems found in their four-component fit of the optical spectrum (Sect. 2.2). The lines belonging to these systems at optical wavelengths ($\text{H}\alpha$, $\text{H}\beta$, [O III], [Ne III], [Fe VII], [N II], and [S II]) are relatively broad and blueshifted by up to 1450 km s^{-1} . The existence of a blueshifted system of [O III] and [Ne III] lines has also been reported in previous publications (Phillips 1976; Oke & Lauer 1979; Laor et al. 1997).

5.3 The Spectrum of the Northern Source

The *H*- and *K*-band spectra of the northern source are shown in Fig. 12. Since the northern source is contained in both slits, the one for $PA = 0^\circ$ and the one for $PA = 43^\circ$, the quality of the *K*-band spectrum is improved by finally averaging both independently reduced *K*-band spectra. This opportunity is not provided for the *H*-band spectra, since the *SH* filter is only used in combination with the $PA = 43^\circ$ setting.

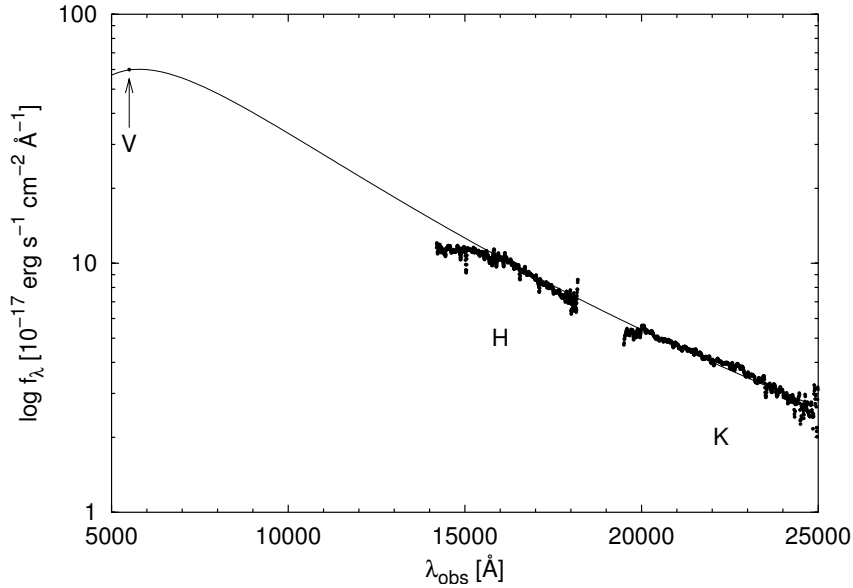


Figure 13: Continuum of the northern source as measured with ISAAC in the H - and K -bands. The measurements are complemented with the flux corresponding to the V -band measurement of $m_V \approx 17$ from Hutchings & Crampton (1990). The specific flux in the three bands is fitted with a blackbody of temperature $T \approx 5000$ K.

5.3.1 Continuum

The continuum fluxes measured in the H - and K -band spectra of the northern source correspond to magnitudes of $m_H \approx 15.3$ and $m_K \approx 14.9$. For this simple approximation, the magnitudes are just estimated from the specific continuum flux f_ν at $16\,500$ Å (1.8×10^{14} Hz) and $22\,000$ Å (1.4×10^{14} Hz), respectively, and the small effects of any color terms (Sect. 3.2.3) are neglected. Fluxes are converted to magnitudes via $m = 2.5 \times (\epsilon - \log f_\nu)$, using the flux zero-points $\epsilon_H = 3.021$ and $\epsilon_K = 2.812$ of the Bessell & Brett photometric system. As evident from Table 4, the magnitudes estimated from the spectra of the northern source agree with the magnitudes obtained from imaging as well as the 2MASS magnitudes. They also confirm the offset from the Eckart et al. (1994) data, which has already been discussed in Sect. 4.2.3.

The mean slope of the H - and K -band fluxes of the northern source, complemented by a V -band measurement (Hutchings & Crampton 1990), are consistent with the continuum spectrum of a blackbody of temperature $T \approx 5000$ K. The corresponding blackbody fit is shown in Fig. 13. The obvious decrease in fluxes towards the respective band limits is a calibration artefact, since calibration becomes imprecise at the edges of the filter curves where the sensitivity rapidly declines.

The temperature of $T \approx 5000$ K is typical of a main-sequence late-type G or early-type K star. This agrees with the derived $(V - K)$ color of about 2.1, which suggests a K1 star (Koornneef 1983). The fact that Eckart et al. (1994) find a slightly later stellar type of K5 again reflects the basic photometric calibration offset between their data and the ISAAC data (Sect. 4.2.3). Their magnitudes are by about 0.6 mag brighter. Referring to the same V -band magnitude of $m_V \approx 17$ (Hutchings & Crampton 1990), this results in a by 0.6 mag redder $(V - K)$ color.

5.3.2 Spectral Lines and Redshift

By comparing the H -band and the averaged K -band spectrum of the northern source with the spectra of G- and K-type main-sequence stars, it is suggested that the source is a local object and most likely an early K-type star.

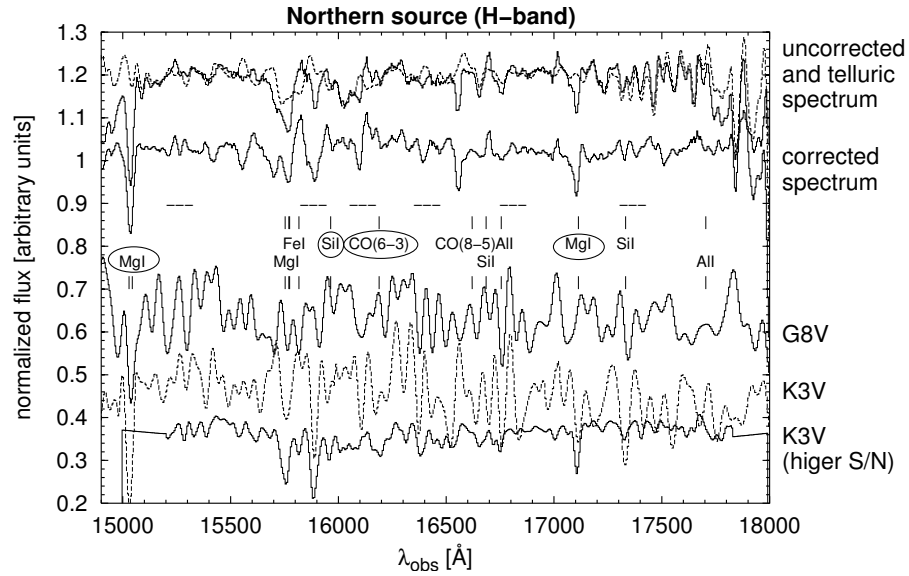
In consequence of their relatively cool temperatures, these types of stars are dominated by absorption lines from neutral metals. Towards hotter stars, i.e. towards early-type G and F stars, neutral metals are replaced by ionized metals. Towards cooler stars of type M, molecular lines, like e.g. the CO bandheads, become increasingly important. A detailed comparison of the spectra of the northern source with reference spectra of late-type G and early-type K stars is presented in Fig. 14.

The H -band spectrum of the northern source is plotted in the upper panel of Fig. 14. The corrected spectrum is shown in the second row. The overlay of the same spectrum before calibration and telluric line correction on the telluric spectrum, shown in the upper row, provides a straight way for distinguishing real absorption features from residual telluric lines or artefacts caused by the telluric correction. It should be noted that the telluric spectrum is plotted before having been fine-tuned in shift and scale to match the telluric lines in the object spectrum (see Sect. 4.1.2). In comparison to the corrected spectrum, the overlay in the upper row allows to easier distinguish between lines and reduction artefacts. The dashed horizontal lines show the regions where the spectrum is affected by the Br absorptions contained in the spectrum of the A0V star used as telluric standard (see Sect. 4.1.2). Three reference spectra are shown in the lower rows of Fig. 14. The spectra of the G8V and K3V stars HD141272 and HD190470 (from Lancon & Rocca-Volmerange (1992)) at lower S/Ns and lower spectral resolutions than the ISAAC spectrum are complemented by another K3V spectrum (from Meyer et al. (1998)) at an ISAAC-like quality but with a cut-off wavelength close to 15 200 Å. The spectra are not smoothed to the worst spectral resolution in order to conserve the resolution of the ISAAC spectrum. The same kind of representation is used for the K -band spectrum in the lower panel of Fig. 14. Here, the reference spectra of the G8V and K2V stars HR4496 and HR1084, taken from Wallace & Hinkle (1997), have been smoothed from medium resolution to match the resolution of the ISAAC spectrum.

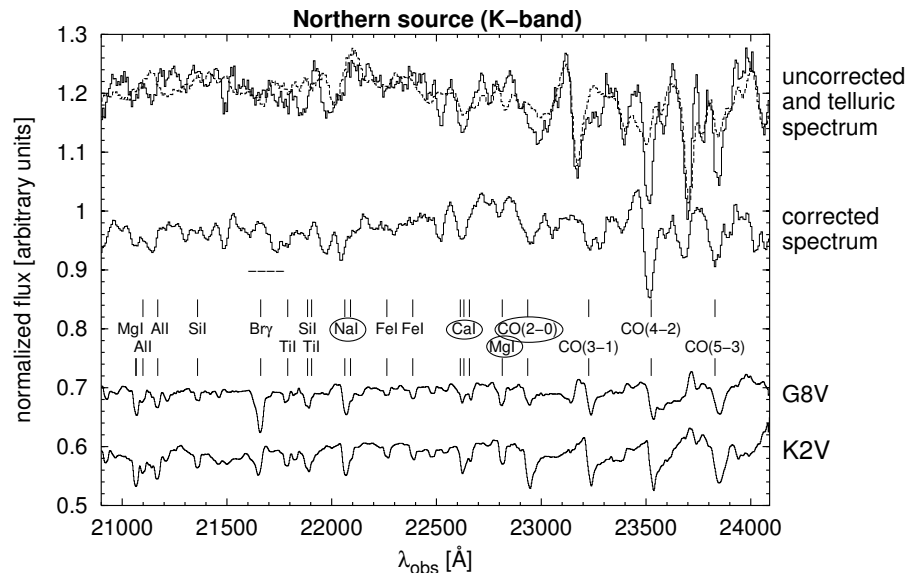
As can be seen from the reference spectra, the most prominent absorption lines of the considered stellar types are the Mg I lines at $\lambda = 15\,029$ Å, $15\,044$ Å, $15\,052$ Å, and at $\lambda = 17\,113$ Å (wavelengths from Table 2 in Lancon & Rocca-Volmerange (1992)). They are clearly identified in the spectrum of the northern source at 11 σ - and 7 σ -levels, respectively. Most importantly, these lines are found at a redshift of $z = 0$. The feature at $\lambda \approx 16\,550$ Å in the H -band image of the northern source is likely to be a reduction artefact.

The individual CO bandheads are only detected at about 3 σ -levels in the spectra of the northern source. However, their identification seems to be confirmed by the fact that all expected bandheads are visible. The presence of CO bandheads is another indication for a cool stellar type.

The detection of other lines is hampered by difficulties arising from the telluric line correction. The K -band spectrum shows indications of the strongest metallic lines Mg I $\lambda = 22\,814$ Å, Ca I $\lambda = 22\,614$ Å, $22\,631$ Å, $22\,657$ Å, and Na I $\lambda = 22\,062$ Å, $22\,090$ Å (wavelengths from Table 2 in Lancon & Rocca-Volmerange (1992)). These lines, in particular, become evident from the overlay of the uncorrected spectrum on the telluric spectrum.



(a) ISAAC H-band spectrum of the northern source at a resolution of 38 \AA ($\sim 690 \text{ km s}^{-1}$).



(b) ISAAC K-band spectrum of the northern source at a resolution of 55 \AA ($\sim 750 \text{ km s}^{-1}$).

Figure 14: Both plots show the uncorrected spectrum before telluric correction and calibration overlaid on the telluric spectrum in the upper row and the final corrected spectrum in the second row. The plots are complemented with reference spectra of stars (see text for references). All spectra are normalized by a low-order polynomial fit. The regions affected by telluric artefacts are marked by the dashed horizontal lines. The line identifications discussed in the text are highlighted by circles. See text for further details.

The missing of the Br γ seems to be a consequence of the telluric correction (Sect. 4.1.2). Since the Br γ absorptions in the spectra of the northern source and the telluric standard just coincide, the line is artificially removed when dividing by the telluric spectrum.

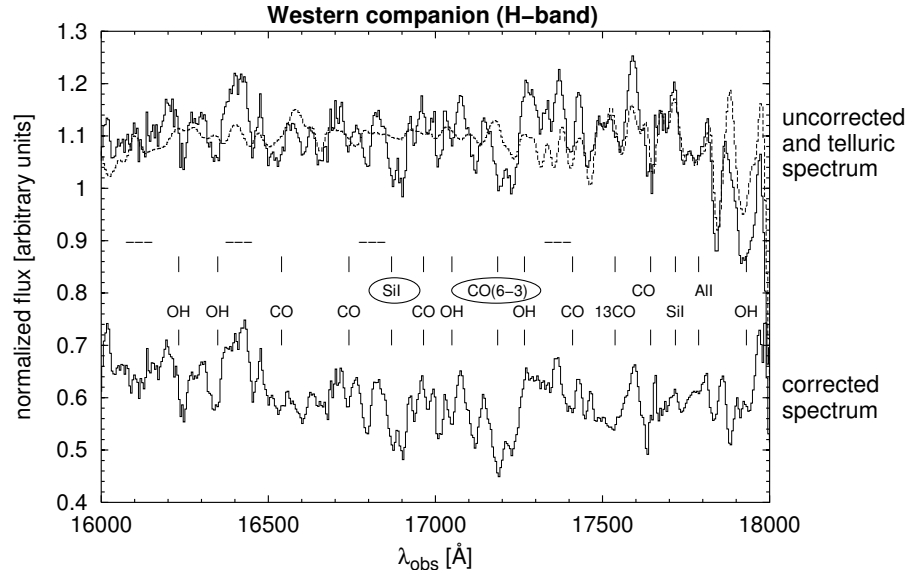
The results of the spectra are consistent with the previous assumption that the source to the north of I Zw 1 is a projected foreground star. Based on the depths of the Mg lines and the CO bandheads, its type is most likely close to K1. This is consistent with the temperature of $T \approx 5000$ K, derived from continuum fitting in the previous section.

The contrasting scenario suggested by Davies et al. (2003), in which the northern source is interpreted as a tidal dwarf galaxy or as the likely nucleus of an interacting galaxy at the redshift of I Zw 1, implies an extreme flux density and stellar mass. Davies et al. (2003) report the source to be resolved in their H -band image with a FWHM of $0''.186$ corresponding to about 220 pc at the redshift of I Zw 1. Assuming that the northern source is located at the redshift of I Zw 1, the H -band flux of $m_H \approx 15.3$ (Sect. 5.3.1 or Table 4) results in an absolute H -band magnitude of $M_H \approx -21.67$. This is computed from the basic relation $M_H = m_H - 5 \log(D_L) + 5$, where $D_L = 242 \times 10^6$ pc is the luminosity distance of I Zw 1. The sun has an absolute H -band magnitude of $M_{H\odot} = 3.32$ (Binney & Merrifield 1998, Table 2.1). This means a number of $10^{-0.4(M_H - M_{H\odot})} \approx 1 \times 10^{10}$ solar-type stars, or equivalently a luminosity of $10^{10} L_\odot$. The mass-to-light ratio is an uncertainty of this estimate. Assuming a moderate solar H -band mass-to-light ratio of about $1 M_\odot/L_\odot$, the resulting total mass of $10^{10} M_\odot$ already exceeds the typical mass estimates of a few $10^9 M_\odot$ for the condensations of tidal dwarf progenitors (Braine et al. 2001; Bournaud et al. 2004b; Duc et al. 2004). This suggests that the scenario of a projected foreground star, which is indicated by the ISAAC spectra, is the more plausible one.

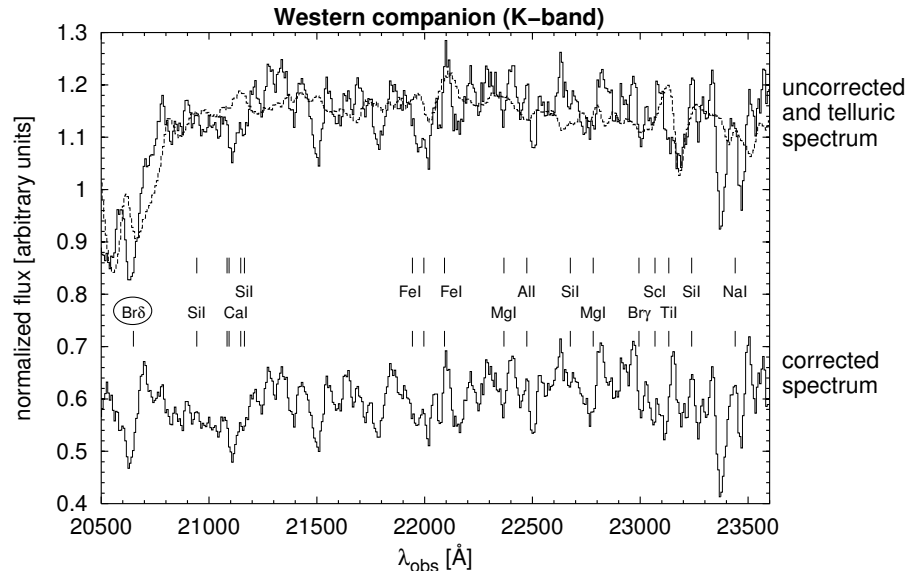
5.4 The Spectrum of the Likely Western Companion

The NIR spectra of normal galaxies are dominated by a combination of absorption features from CO and OH molecules and absorption lines from neutral metals, which is typical of a stellar population predominantly consisting of late-type K and M stars. The spectra of elliptical galaxies are characterized by absorption features only. Hydrogen emission lines become increasingly important along the Hubble sequence towards late-type spiral galaxies, according to the increasing fraction of a young and hot stellar population. The spectra of galaxies with active nuclei, as exemplified by the nuclear spectrum of I Zw 1 in Fig. 9, typically consist of strong hydrogen emission lines as well as permitted and coronal lines from the narrow-line and coronal-line regions.

In the following section, the companion spectrum is investigated with respect to these considerations. The flux of the companion galaxy is, by more than a factor of 2, lower than the one of the northern source. Consequently, the companion spectra are characterized by the lowest S/N of all spectra discussed here. As the low S/N does not only degrade the detection of lines intrinsic to the companion but likewise the detection of telluric lines, the telluric line correction is more complicated than the one of high S/N spectra. It is, therefore, extremely difficult to distinguish noise peaks and telluric line artefacts from real lines. In order to account for these difficulties, the analysis is first of all based on a conservative qualitative discussion of the spectra. In a second step, it is attempted to quantify some apparent detections.



(a) ISAAC *H*-band spectrum of the western source at a resolution of 38 \AA ($\sim 690 \text{ km s}^{-1}$)



(b) ISAAC *K*-band spectrum of the western source at a resolution of 55 \AA ($\sim 750 \text{ km s}^{-1}$).

Figure 15: The representation is the same as the one in Fig. 14. Instead of reference spectra, the plot contains marks for absorption features which are typically found in the spectra of normal elliptical and spiral galaxies. The theoretical line positions are shifted to the companion redshift of $z = 0.0616$ (Canalizo & Stockton 2001).

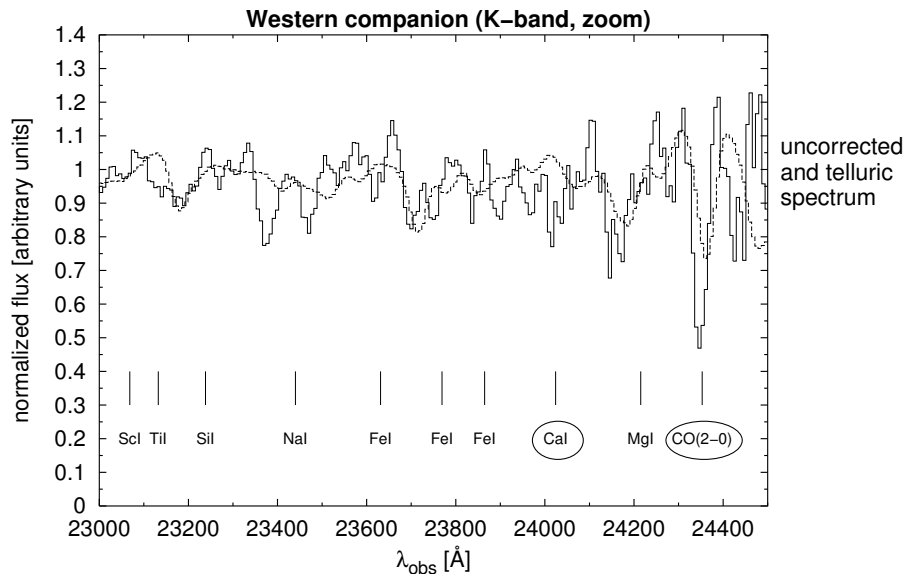


Figure 16: Magnification of the long-wavelength end of the K -band spectrum of the companion. The figure shows the overlay of the companion spectrum before telluric correction and calibration (solid line) on the telluric spectrum (dashed line). The spectra have resolutions of 55 \AA ($\sim 750 \text{ km s}^{-1}$). The theoretical line positions are shifted to the companion redshift of $z = 0.0616$ (Canalizo & Stockton 2001).

5.4.1 Qualitative Analysis

The H - and K -band spectra of the companion as well as a close-up on the long-wavelength K -band regime are plotted in Figs 15 and 16, respectively. The spectra are shown as uncorrected and corrected spectra, using the same kind of representation as in Sect. 5.3.2. Instead of reference spectra, the figures are complemented with marks for those absorption lines which could be expected in the spectra of old stellar populations. The corresponding line positions are adapted to the companion redshift of $z = 0.0616$ (Canalizo & Stockton 2001).

The conservative conclusion from the spectra of the companion is that there is no significant indication of emission lines. The mere absence of strong emission lines rules out any scenario for nuclear activity or star formation activity in the companion. In contrast, the weak indications of some typical absorption lines rather suggest a predominantly old stellar population. Evidence for this can be found in the K -band spectrum (lower panel of Fig. 15) which shows a feature consistent with the $\text{Br } \delta$ line in absorption. The overlay of the uncorrected and the telluric spectrum suggests that this feature is a real detection, although the spectrum at these wavelengths is strongly affected by telluric absorptions. Indications, however less reliable ones, are displayed for the strongest expected absorption lines, such as Si I at $\lambda_{\text{obs}} = 16870 \text{ \AA}$, Ca I at $\lambda_{\text{obs}} = 24000 \text{ \AA}$, or the $^{12}\text{CO} (6-3)$ and $^{12}\text{CO} (2-0)$ bandheads at $\lambda_{\text{obs}} = 17180 \text{ \AA}$ and at $\lambda_{\text{obs}} = 24340 \text{ \AA}$, respectively. These lines are marked by circles in the three figures.

5.4.2 A Tentative Quantitative Analysis

According to Origlia et al. (1993), there are three absorption features which provide useful classification diagnostics in the case of cool stars: the Si I feature at $\lambda = 15\,900\text{ \AA}$ measured by Origlia et al. (1993) between $\lambda = 15\,870\text{ \AA}$ and $\lambda = 15\,910\text{ \AA}$, the $^{12}\text{CO}(6-3)$ feature at $\lambda = 16\,200\text{ \AA}$ measured between $\lambda = 16\,175\text{ \AA}$ and $\lambda = 16\,220\text{ \AA}$, and the $^{12}\text{CO}(2-0)$ feature at $\lambda = 22\,900\text{ \AA}$ measured between $\lambda = 22\,924\text{ \AA}$ and $\lambda = 22\,977\text{ \AA}$. These features are not only caused by the contributors which are used for the naming. Origlia et al. (1993) give the example of the Si I feature which is present for virtually all stellar types, but only caused by the Si I line in the case of stellar types between G4 and M2. In hotter stars, the feature is due to hydrogen, in cooler stars it is mainly caused by OH.

The basic variations in equivalent widths with spectral type are shown in the underlying image of Fig. 17. This image is a reproduction of Fig. 5a in Origlia et al. (1993).

- The equivalent width of the absorption feature of Si I is empirically found to be constant for G0 through M7 type stars, although OH becomes the main contributor at stellar types cooler than M2. The Si I absorption alone is, therefore, no clear indicator of the stellar type.
- The $^{12}\text{CO}(6-3)$ bandhead is only present in stars cooler than K0 and its equivalent width increases almost linearly towards M7 types.
- The equivalent width of the $^{12}\text{CO}(2-0)$ bandhead increases towards M stars and stays almost constant for late-type M stars. It is known that this increase is hardly dependent on the change in stellar temperature.
- The ratio of the equivalent widths of the $^{12}\text{CO}(6-3)$ bandhead and the Si I absorption is sensitive to temperature. This is a direct consequence of the fact that the equivalent width of the $^{12}\text{CO}(6-3)$ bandhead increases, the cooler the stellar type, while the Si I absorption stays nearly constant. Since the $^{12}\text{CO}(2-0)$ bandhead is also nearly independent of the stellar temperature, the same is true for the ratio of the equivalent widths of $^{12}\text{CO}(6-3)$ and $^{12}\text{CO}(2-0)$.

In order to attempt a quantitative comparison with the weak line detections in the companion spectrum, the noise is simply estimated from the RMS in the individual spectral ranges corresponding to the spectra in Figs 15 and 16. The *H*-band spectrum in Fig. 15 displays a noise of $\sigma \approx 0.05$ in the normalized flux units. For the given spectral resolution of 38 \AA , this corresponds to an error of $\pm 2\text{ \AA}$ in equivalent widths. Consequently, absorption lines with equivalent widths larger than 6 \AA are considered as 3σ -detections. The two diagnostic features accessible in the *H*-band spectrum of the companion are the one of the $^{12}\text{CO}(6-3)$ bandhead at a theoretical redshifted line position of $\lambda_{\text{obs}} = 17\,180\text{ \AA}$ and the one of the Si I absorption at $\lambda_{\text{obs}} = 16\,870\text{ \AA}$ (marked by circles in Fig. 15). Since the equivalent width of Si I absorption is below 5 \AA for all spectral types (see Fig. 17 and Origlia et al. 1993), the 3σ upper limit of an equivalent width of 6 \AA does not allow a stringent conclusion about the stellar type. The upper limit and the possible range of spectral types are indicated by the solid and dashed arrows in Fig. 17. In the *H*-band spectrum, a 4σ -detection is only possible for the $^{12}\text{CO}(6-3)$ feature. Using the redshifted equivalent of the wavelength range defined for this feature by Origlia et al. (1993), the feature is found with an equivalent width of $(8 \pm 2)\text{ \AA}$. In the overlay in Fig. 17

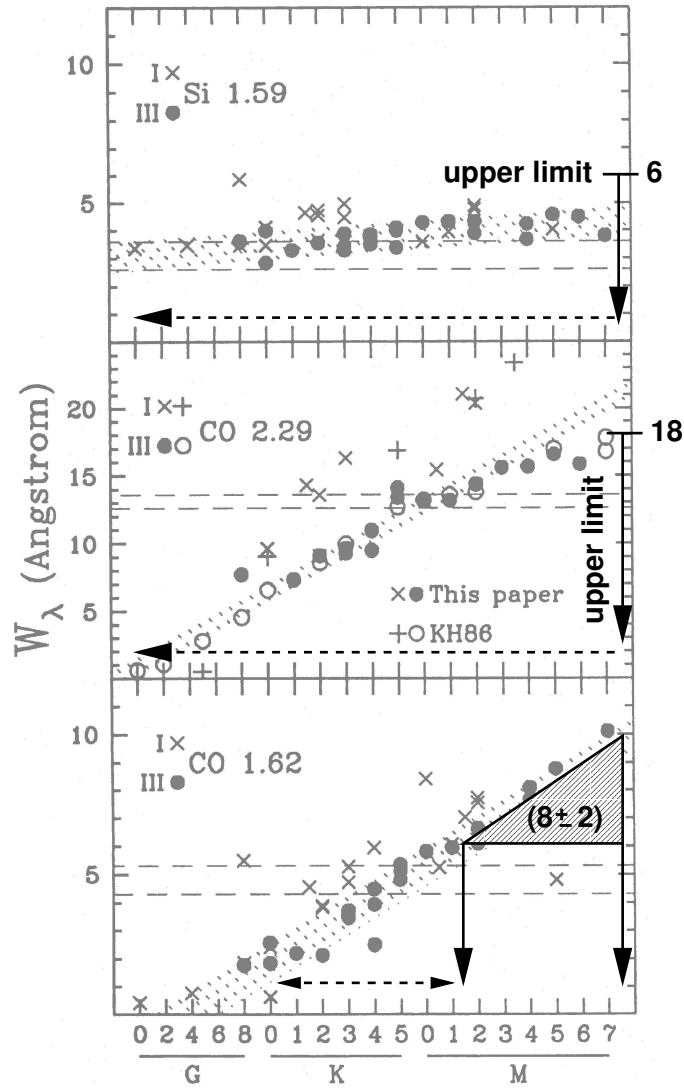


Figure 17: Overlay of the tentative line measurements obtained from the companion spectra on a reproduction of Fig. 5a from Origlia et al. (1993). The figure shows the basic variations of the observed equivalent widths of the Si I absorption at $\lambda = 15\,900 \text{ \AA}$, and of the $^{12}\text{CO}(6-3)$ and $^{12}\text{CO}(2-0)$ bandheads at $\lambda = 16\,200 \text{ \AA}$, and $\lambda = 22\,900 \text{ \AA}$, respectively, with spectral type. Giants are marked by circles, supergiants by crosses. See Origlia et al. (1993) for a detailed description of the plotted data. In the case of the undetected Si I and $^{12}\text{CO}(2-0)$ absorptions, the overlaid solid arrows indicate the 3σ -level. The dashed arrows show that the whole range of stellar types is possible. In the case of $^{12}\text{CO}(6-3)$ the shaded triangle shows the range of stellar types possible within the error limits of the equivalent width. The dashed arrow indicates that in the weakest statement, the mere presence of the $^{12}\text{CO}(6-3)$ bandhead means a stellar type cooler than about K0.

this value is compared with the relation derived by Origlia et al. (1993). As the companion is likely to have a mixture of different stellar types, the equivalent width of $^{12}\text{CO}(6-3)$ is expected to be lower than the one measured for an individual star. This means that the lower error limit of 6 \AA represents the youngest possible stellar type. However, within the errors, stellar types close to M7 are also possible. In the weakest statement, the mere presence of the $^{12}\text{CO}(6-3)$ bandhead already indicates a stellar type cooler than K0. This is shown by the dashed arrow.

The K -band spectrum of the companion in the range plotted in Fig. 16 displays a noise of $\sigma \approx 0.1$ in the normalized flux units. For the given spectral resolution of 55 \AA , this corresponds to an error of $\pm 6 \text{ \AA}$ in equivalent widths and a 3σ detection level of 18 \AA . The $^{12}\text{CO}(2-0)$ bandhead at $\lambda_{\text{obs}} = 24340 \text{ \AA}$, as the third diagnostic line studied by Origlia et al. (1993), is only found at a detection level of about 2σ . The 3σ detection level of 18 \AA can, therefore, be taken as an upper limit estimate. This estimate just coincides with the maximum equivalent widths displayed by the stellar types in Fig. 17. Based on the depth of the $^{12}\text{CO}(2-0)$, bandhead all stellar types are possible.

The most stringent result from these tentative measurements is provided by the mere presence of the $^{12}\text{CO}(6-3)$ bandhead, which already suggests a mean stellar type cooler than K0 for the companion. In comparison to the relation published by Origlia et al. (1993), the measured depth of $(8 \pm 2) \text{ \AA}$ indicates a stellar population dominated by M1 to M7 stars. By suggesting an old evolved stellar population for the western companion galaxy, the ISAAC spectra are consistent with the optical spectrum discussed by (Canalizo & Stockton 2001). This spectrum also suggests a predominantly old stellar population.

5.5 Near-Infrared Colors

NIR colors and their changes across a galaxy provide insights into the presence and distribution of dust and give an estimate of the ages of the prevailing stellar populations.

The colors discussed here are obtained from the ISAAC J -, H -, and K -images (Fig. 6). In order to guarantee spatial consistency among the three images, they are all convolved to the lowest angular resolution of $0''.62$, displayed by the J -band image. The color measurements are presented in two-color diagrams which contain color data from certain positions in the J -, H -, and K -images. These data are based on photometry using apertures of $3''$ in diameter for the flux integration. The colors immediately result from the respective magnitude differences or, alternatively, from flux ratios. The regions which are biased by saturation or by the four-spiked features (see Sect. 4.2.3) are avoided during the measurements.

5.5.1 The I Zw 1 Host

The NIR colors of the I Zw 1 host measured at different positions in $3''$ -wide apertures are plotted in the two-color diagram in Fig. 18. Within the mean error of ± 0.1 mag, all colors from the different positions are distributed around a mean color of $\langle(J-H)\rangle = 0.8 \pm 0.1$ and $\langle(H-K)\rangle = 0.5 \pm 0.1$. This corresponds to K -corrected colors (Sect. 4.3) of $\langle(J-H)\rangle_{\text{rest}} = 0.8 \pm 0.1$ and $\langle(H-K)\rangle_{\text{rest}} = 0.4 \pm 0.1$. A mean reddening by dust is suggested by the fact that these colors are redder than the colors displayed by nearby normal galaxies. The K -corrected colors measured for I Zw 1 are compared to the colors of nearby normal galaxies (Fioc & Rocca-Volmerange 1999) in Table 7. As the reddening

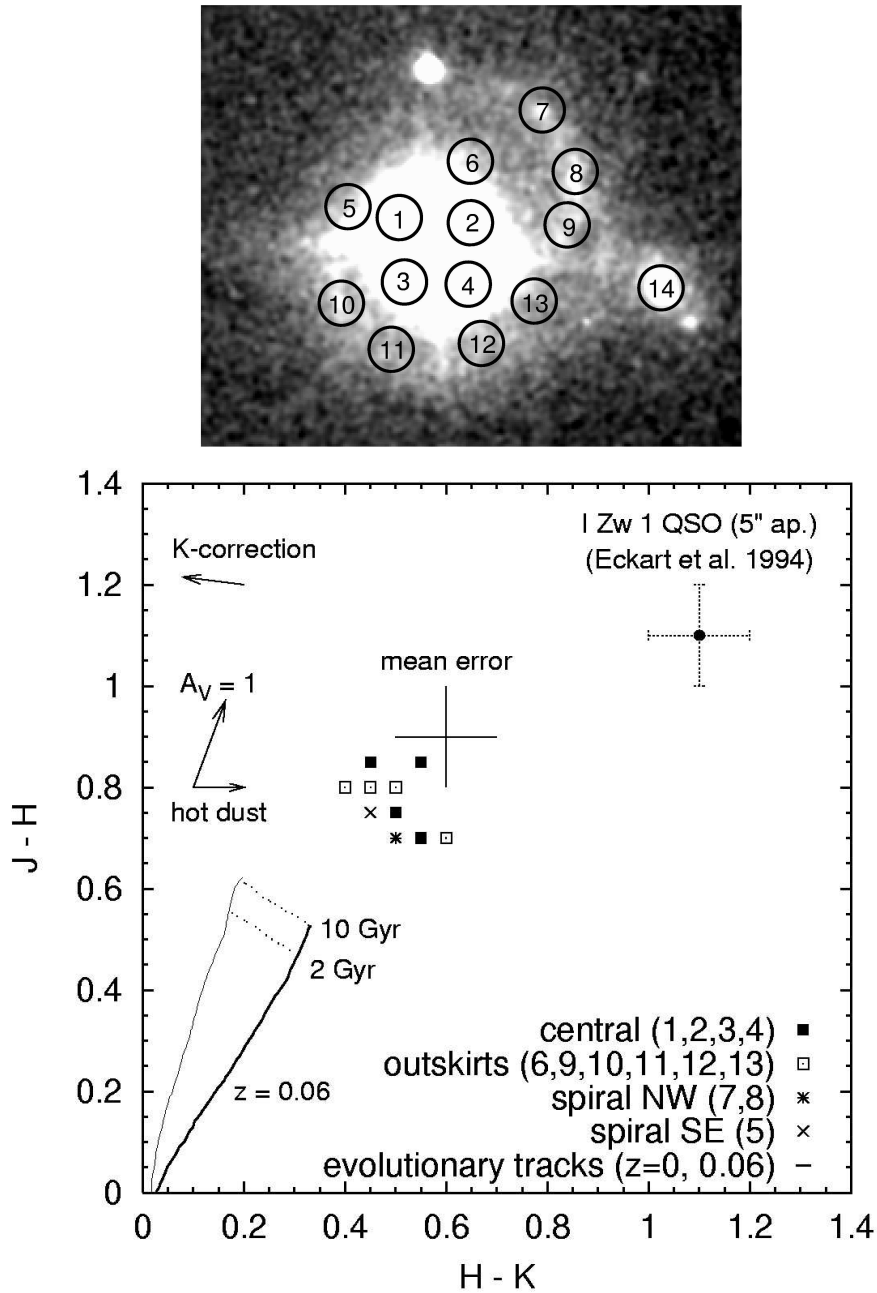


Figure 18: *JHK* colors from different regions of the I Zw 1 host. The colors plotted in the lower panel are measured in apertures of $3''$ in diameter, as indicated in the realistically scaled overlay on the *Ks*-band image shown in the upper panel. Only the apertures 1 to 13 are plotted here, the color of the companion (aperture 14) is discussed separately (Sect. 5.5.2). The mean error of the color measurements of ± 0.1 mag is indicated. The arrow for the *K*-correction shows the change in color for a transformation from $z = 0.06$ to the rest-frame color for $z = 0$ (see Sect. 4.3). A second arrow indicates the reddening which corresponds to 1 mag of visual extinction under the assumption of the standard interstellar extinction law (Rieke & Lebofsky 1985). In addition, the reddening produced by hot dust is visualized. The color of the I Zw 1 QSO is added from literature (Eckart et al. 1994). Evolutionary tracks from Gissel stellar population models for $z = 0$ and $z = 0.06$ are reproduced from Hutchings & Neff (1997), Fig. 2. The tracks result from a 1 Gyr starburst followed by passive evolution.

Table 7: Comparison of the mean NIR colors obtained from color measurements at different positions on the I Zw 1 host with the NIR colors of nearby normal galaxies (Fioc & Rocca-Volmerange 1999).

Galaxy type	$(J - H)^a$ [mag]	$(H - K)^a$ [mag]	$\langle(J - H)\rangle_{\text{rest}}^b$ [mag]	$\langle(H - K)\rangle_{\text{rest}}^b$ [mag]
E	0.71	0.20		
S0	0.72	0.22		
Sa	0.74	0.27		
Sb	0.78	0.25		
Sbc	0.77	0.22	0.8 ± 0.1	0.5 ± 0.1
Sc	0.72	0.21		
Sd	0.72	0.21		
Im	0.57	0.23		

^a Total colors reported by Fioc & Rocca-Volmerange (1999) in their Tables 3 and 4. These measurements have errors in the range of ± 0.01 mag to ± 0.05 mag. The errors are not reproduced for the purpose of this discussion.

^b Mean colors measured for the I Zw 1 host.

effect is most evident in $\langle(H - K)\rangle_{\text{rest}}$, it could indicate a certain contribution from hot dust.

A certain amount of reddening is consistently suggested by the location of the I Zw 1 host colors with respect to the theoretical evolutionary track of a stellar population at $z = 0.06$ (Fig. 18). The evolutionary tracks are reproductions of the tracks shown in Fig. 2 of Hutchings & Neff (1997). Assuming a mean visual extinction of about 1 mag plus a varying amount of hot dust, all aperture colors are shifted to the upper end of the $z = 0.06$ evolutionary track. This location in the two-color diagram corresponds to an evolved stellar population of about 10 Gyr. It is an important fact that the reddening vector and the evolutionary track have about the same slopes so that reddening and aging effects are indistinguishable. However, the central region of I Zw 1 is significantly extinguished (Eckart et al. 1994; Schinnerer et al. 1998, and Sect. 5.6.7) and, therefore, stronger reddened than the large-scale host disk. Consequently, the data for the positions 1, 2, 3, and 4 are likely to require a stronger extinction correction than the remainder of the color measurements. By this, they are shifted towards significantly younger ages on the model evolutionary track. This finding is in agreement with the proposed scenario of a heavily reddened, young, and, most likely, starbursting population towards the bulge and the nuclear region (Eckart et al. 1994; Schinnerer et al. 1998).

5.5.2 The Likely Western Companion

The companion shows NIR colors of $(J - H) = 0.8 \pm 0.1$ and $(H - K) = 0.4 \pm 0.1$, similar to the mean colors measured for the I Zw 1 host (Fig. 18) but slightly bluer in $(H - K)$. Since the redshift of the companion is close to the redshift of I Zw 1 ($z = 0.0616 \pm 0.0001$, Canalizo & Stockton 2001), the colors are subject to the same K -correction. This results

in K -corrected colors of $(J - H)_{\text{rest}} = 0.8 \pm 0.1$ and $(H - K)_{\text{rest}} = 0.3 \pm 0.1$. Unlike the I Zw 1 host, the companion is a typical representative of nearby E through Sd galaxies in both colors (see Table 7). This suggests that hot dust does not play a significant role in the case of the companion. Since the spectrum of the companion suggests an evolved mean stellar population (Sect. 5.4), its colors, close to the usual colors of nearby galaxies or close to the upper end of the evolutionary track in Fig. 18, suggest that a possible visual extinction is small.

Within the errors, the $(H - K)$ color measured for the companion is consistent with the color taken from Fig. 9 in Schinnerer et al. (1998). The broad band spectrum, shown there together with the data errors indicated in the plot, provides an upper limit of the $(H - K)$ color of about 0.7.

5.6 Structural Decomposition of the I Zw 1 Host Galaxy

In this section, a decomposition of the I Zw 1 host into bulge, disk, and dark halo contributions is discussed and analyzed with respect to mean mass-to-light ratios which are indicative of trends in the ages of stellar populations. For the decomposition the J -band surface-brightness profile and the gas rotation curve of the I Zw 1 host are fitted with analytical profiles based on Miyamoto-Nagai gravitational potential models. Since the surface brightness of the host galaxy is required, the flux contribution from the QSO nucleus has to be artificially removed.

As the band least affected by saturation (Sect. 4.2.3), the J -band is chosen for a one-dimensional investigation of the surface-brightness profile. Radial symmetry can be considered as a valid assumption for three main reasons.

- (i) The I Zw 1 host is characterized by a low inclination.
- (ii) In the NIR, the spiral arms are less pronounced than in the optical (see Sect. 5.1), so that their presence means only a small error for the assumption of radial symmetry.
- (iii) Previous ellipse fitting to a NIR image of I Zw 1 resulted in an almost constant ellipticity of only 0.1 throughout the disk (Peletier et al. 1999). The comparison between the radially averaged profile obtained from the J -band image and the profile obtained by Peletier et al. (1999) from ellipse fitting is shown in Fig. 19. The good agreement between both profiles emphasizes that the errors implied in the assumption of radial symmetry are small.

A procedure for radial averaging along circles is provided by the IRAF task PRAD-PROF. The thus derived profile is further binned logarithmically and error bars are computed from the standard deviations of the data points within the bins.

5.6.1 Subtraction of the QSO Nucleus

The bright QSO nucleus inhibits the investigation of the underlying host galaxy and has to be artificially subtracted. For the subtraction it is usually assumed that the QSO is a point source and characterized by the point spread function (PSF), (see Sect. 3.1). The PSF is built from stars in the image and subtracted at the position of the QSO nucleus after a suitable scaling. Without knowing the flux contribution from the QSO component, there is a wide range of possible scaling factors. In most cases, the scaling factor is derived by

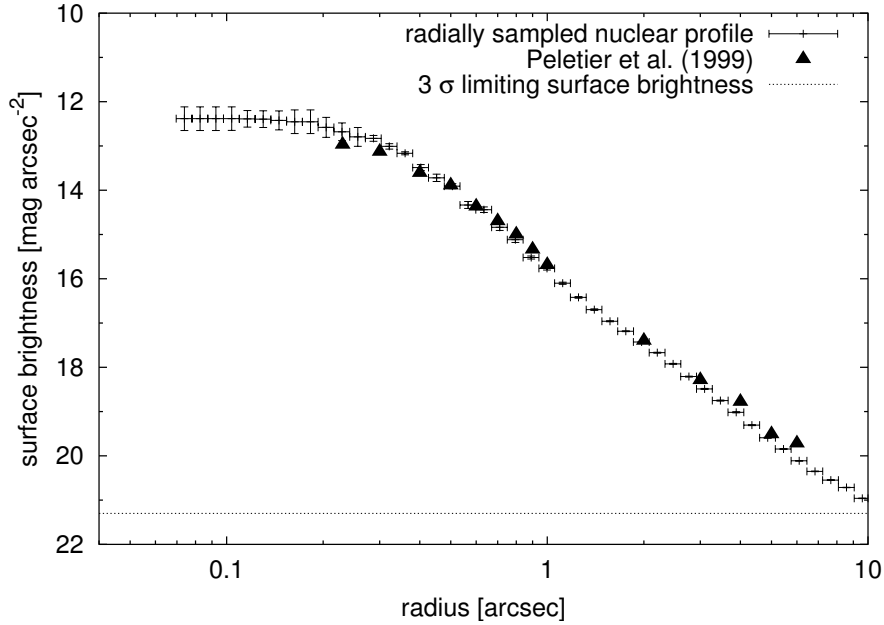


Figure 19: Radial profile of the J -band surface brightness of I Zw 1 before QSO subtraction (data and error bars). The profile is obtained along circles of increasing radius, centered on the I Zw 1 QSO and binned logarithmically. The error bars represent the standard deviation of the binned data points. Previous data obtained from ellipse fitting by Peletier et al. (1999) are added for comparison (filled triangles). The dotted line indicates the 3σ limiting surface brightness.

presuming either a particular brightness distribution of the host galaxy or certain model brightness distributions as input for fitting algorithms (e.g. Bahcall et al. 1995; Hunt et al. 1999; Percival et al. 2001). Each of these methods implies its own uncertainties and the resulting shape of the central host brightness is rather arbitrary between the limits given by the original brightness distribution and the extreme case of a flat brightness distribution.

In the case of I Zw 1 a range of scaling factors can be estimated from previous results about the stellar and the non-stellar fraction of the nuclear NIR flux in I Zw 1 (Eckart et al. 1994; Schinnerer et al. 1998). Analyzing NIR colors, Eckart et al. (1994) find that about 15% of the nuclear K -band flux in a $5''$ -wide aperture are contributed by stars. An upper limit of 24% stellar contribution to the total nuclear K -band flux in a $3''$ -wide aperture and a stellar contribution of $(27\% \pm 6\%)$ to the total nuclear H -band flux in a $3''$ -wide aperture are derived by Schinnerer et al. (1998) from the depths of the Ca I triplet and a ^{12}CO (6-3) bandhead in K - and H -band spectra of I Zw 1.

The percentages X translate into magnitudes via $m^{\text{stell}} = m^{\text{total}} - 2.5 \log(X/100)$ and $m^{\text{QSO}} = m^{\text{total}} - 2.5 \log(1 - X/100)$, respectively. The corresponding J -band magnitudes and magnitude differences $\Delta m_J = m_J^{\text{QSO}} - m_J^{\text{total}}$ are computed, using $(J - H) = 0.95$ and $(H - K) = 1.14$ according to the colors of a mean zero-redshift QSO (Hyland & Allen 1982). The different scaling factors corresponding to the initial assumptions about the stellar flux contribution are given as magnitude differences Δm_J in Table 8. Large Δm_J correspond to strong stellar contributions and, therefore, bright host bulges after the subtraction. If the K -correction for the zero-redshift QSO colors is taken into account, the results show a trend towards larger Δm_J , as indicated by the values enclosed in brackets. As the nucleus

Table 8: Results for the PSF scaling factor expressed as magnitude differences $\Delta m_J = m_J^{\text{QSO}} - m_J^{\text{total}}$. The factors are based on the different assumptions about the stellar contribution to the total nuclear flux available from Eckart et al. (1994) and Schinnerer et al. (1998). The column for Δm_J^{KC} shows the respective results if the K -correction according to Sect. 4.3 is applied. See text for details.

Initial Assumption	Δm_J [mag]	Δm_J^{KC} [mag]
15% stellar in K	0.1	0.2
24% stellar in K	0.2	0.3
$27\% \pm 6\%$ stellar in H	0.1 – 0.3	0.1 – 0.3

of I Zw 1 is saturated in the ISAAC H - and K -band images, all estimates of J -band magnitude differences shown in Table 8 are computed from the nuclear H - and K -band magnitudes given for $5''$ -wide apertures by Eckart et al. (1994). This is done irrespective of the fact that the Schinnerer et al. (1998) percentages of stellar contributions refer to smaller apertures. This causes an additional uncertainty to the basic uncertainty implied in the estimates of stellar contributions. From the range of values an analytical magnitude difference of $\Delta m_J = 0.13$ is finally chosen to scale the peak flux of the Gaussian PSF of the J -band image.

It is intrinsic to the PSF fitting procedure that the pixel values of the northern foreground star as well as of the QSO component display a scatter around the Gaussian model. This inevitably results in a small number of negative pixel values after the subtraction. In the very center of the QSO brightness peak, negative values might also result from the possible saturation (Sect. 4.2.3). The effects of pixel scattering are eliminated by the restriction to one-dimensional radially averaged profiles in the further analysis.

The radially averaged sampling of the nuclear profile and the Gaussian PSF, scaled to the used magnitude difference of $\Delta m_J = 0.13$, are shown in Fig. 20. The subtraction for the J -band image from *Cycle A* is done in the two-dimensional images, by using the PSF obtained from an analytical Gaussian fit to the northern foreground star. The radially averaged results of this two-dimensional subtraction are crosschecked by a one-dimensional subtraction procedure based on profiles from the *Cycle B* J -band image (Sect. 4.2.3). The comparison of both profiles is shown in Fig. 21. The profiles basically agree in their central shapes.

As suggested by the rather flat shapes of the central surface brightnesses of the QSO-subtracted profiles, the profiles are likely to trace a lower limit of the central surface brightness of the I Zw 1 host galaxy. The corresponding magnitude difference of $\Delta m_J = 0.13$ used for scaling the PSF, therefore, seems to represent nearly an upper limit of the QSO contribution to the nuclear flux. A stronger QSO contribution would result in a physically unlikely decrease of the QSO-subtracted profile towards the center.

Based on the comparison of the one-dimensionally and the two-dimensionally subtracted profiles in Fig. 21, both profiles seem likewise suitable for the further analysis of the host galaxy and the two-dimensional one is used for the fitting presented below. Both profiles show deviations from a smooth shape, like the depressions at about $0''.15$ and $0''.4$ in the one-dimensionally and the two-dimensionally subtracted profile, respectively. These depressions are likely subtraction artefacts, since they do not coincide in radius in the two

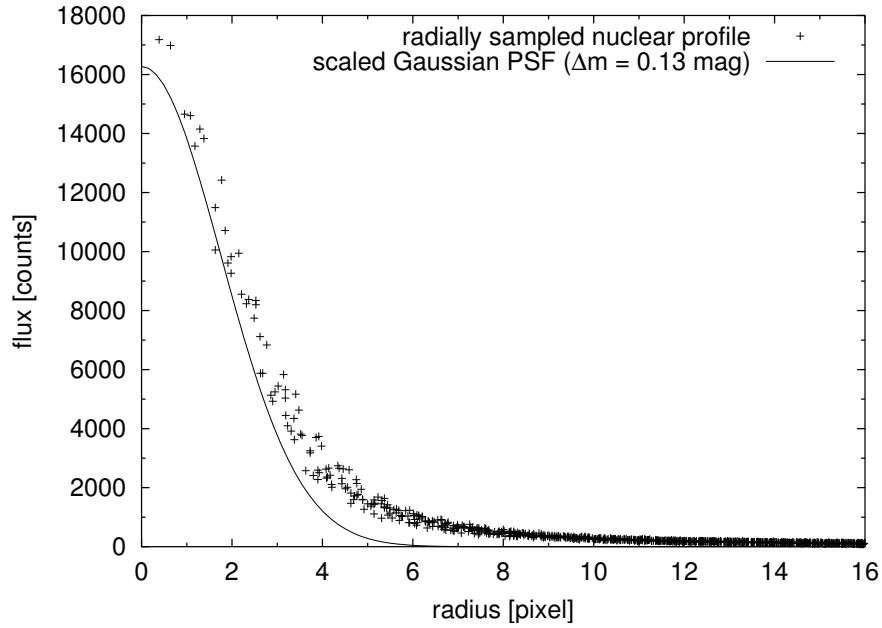


Figure 20: Radially averaged J -band profile of the I Zw 1 nucleus and Gaussian PSF, scaled to the assumed QSO contribution to the total nuclear flux. The magnitude difference of $\Delta m_J = 0.13$ means a factor of $10^{-0.4\Delta m_J} = 0.887$ in counts. The ISAAC pixel scale is given by $0''.1484/\text{pixel}$.

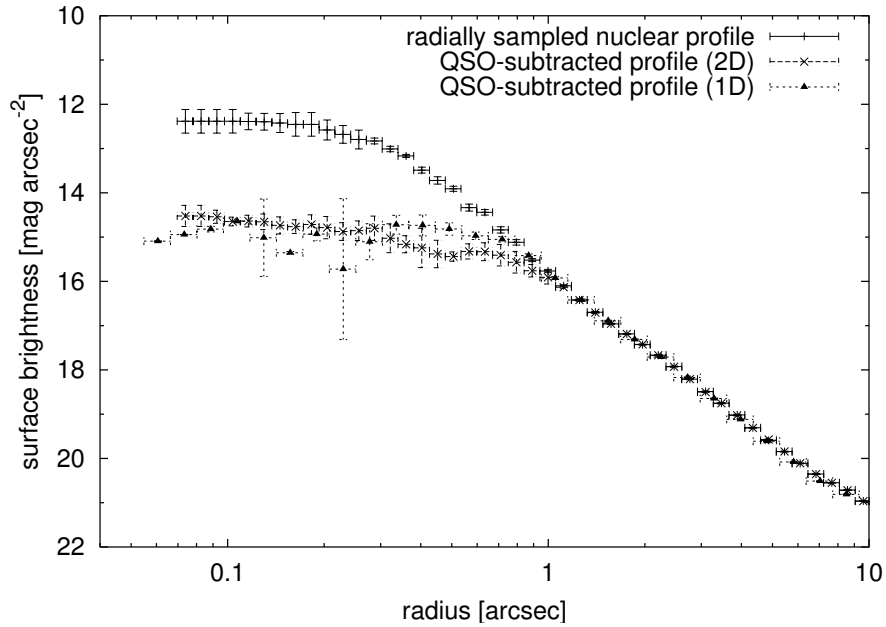


Figure 21: Radial profile of the J -band surface brightness of I Zw 1 before and after QSO subtraction. The QSO subtraction based on the two-dimensional subtraction from the J -band image from reduction Cycle A is compared to the subtracted profile obtained from a one-dimensional procedure based on the Cycle B J -band image (triangles). All profiles are obtained along circles of increasing radius, centered on the position of the I Zw 1 QSO and binned logarithmically. The error bars represent the standard deviation of the binned data points.

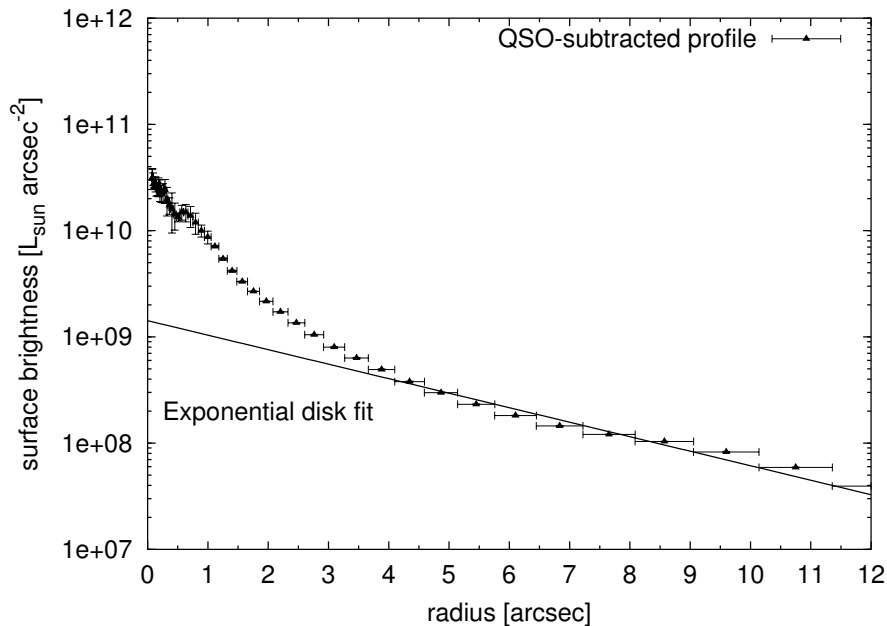


Figure 22: Radial profile of the J -band surface brightness of the I Zw 1 host galaxy after QSO subtraction. The profile is calibrated in solar luminosities as described in the text. The flat disk region of the profile is fit with an exponential disk.

profiles. This shows that the uncertainties implied in the QSO-subtraction are too large to allow for a small-scale investigation of the radial profile of the host galaxy. However, the host profile is valuable for an investigation of the global properties of the bulge and the disk component. Based on smooth brightness models for the bulge and the disk, this kind of analysis is only marginally affected by profile deviations.

5.6.2 First-Order Analysis of the Surface-Brightness Profile and the Gas Rotation Curve of the I Zw 1 Host

The final profile of the I Zw 1 host galaxy after QSO subtraction and calibration in solar luminosities is shown in Fig. 22, together with the analytical profile of an exponential disk fitted to the disk region.

The transformation of magnitudes into units of solar luminosities is given by

$$L = 2.0066 \times 10^{16} \times 10^{-0.4m} L_{\odot}. \quad (5.1)$$

This relation is a compound of three calibration steps.

- As an approximation for the small redshift of I Zw 1, it is assumed that the luminosity L_{ν} at the frequency ν can be derived from the specific flux f_{ν} at the same frequency via $L_{\nu} = 4\pi D_L^2 \times f_{\nu}$. The luminosity distance (see Appendix C) of I Zw 1 is nearly the same as the angular-size distance and given by $D_L = 242$ Mpc.
- The flux calibration is done in the UKIRT photometric system (see Sect. 3.2.3), using $f_{\nu} = 10^{\epsilon} \times 10^{-0.4m}$. The corresponding UKIRT flux zero point in the J -band, already corrected for the transformation from the LCO/Palomar NICMOS system to the UKIRT system, according to Equation (3.6), is given by $\epsilon = 3.217$.

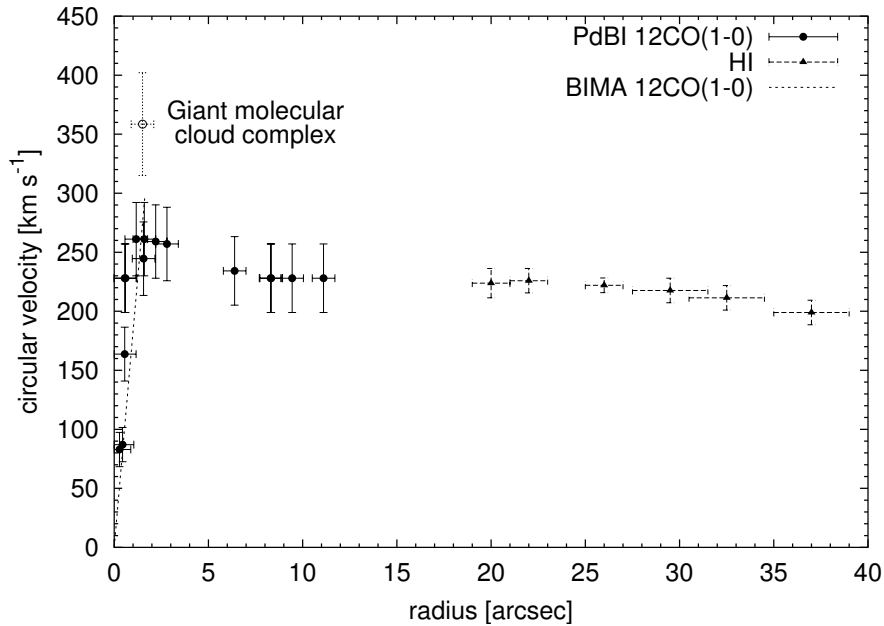


Figure 23: Rotation curve of I Zw 1 compiled from different sets of $^{12}\text{CO}(1-0)$ and HI observations, and corrected for the constant inclination of 38° (Schinnerer et al. 1998). The method of compilation and the characteristics like the giant molecular cloud complex are explained in Scharwächter (2001). The Plateau de Bure (PdBI) data points refer to Schinnerer et al. (1998). The BIMA (Berkeley Illinois Maryland Association) and the HI data points refer to data kindly provided by Dr. Johannes Staguhn and Dr. Jeremy Lim, respectively, (see also Lim & Ho 1999; Staguhn et al. 2004).

- The solar J -band luminosity is estimated from the data in Binney & Merrifield (1998), Table 2.1, divided by the filter band width.

With respect to the Freeman classification of galaxy structures (Freeman 1970), the first-order analysis in Fig. 22 reveals the I Zw 1 host as a *Freeman type I* galaxy as well as a high-surface-brightness galaxy. *Freeman type I* means that the bulge and the disk are present as clearly distinct components. High-surface-brightness galaxies are classified by a central disk surface brightness of $\mu_0(B) < 21.65 \text{ mag arcsec}^{-2}$. Since the criterion is given for the B -band, the central disk surface brightness of $\mu_0(J) = 17.9 \text{ mag arcsec}^{-2}$, measured from the exponential disk fit in Fig. 22, is extrapolated to $\mu_0(B) \approx (19.5 \pm 0.5) \text{ mag arcsec}^{-2}$, according to published magnitudes and colors of the I Zw 1 host galaxy (Hutchings & Crampton 1990; Schinnerer et al. 1998).

The classification as a high-surface-brightness galaxy is consistent with the shape of the gas rotation curve of the I Zw 1 host galaxy (Fig. 23). The rotation curve is explained in detail in Scharwächter (2001). It shows the central steep increase and the flat outer part, typical of the universal rotation curve of high-surface-brightness galaxies (Persic et al. 1996). This kind of galaxies is likely to be associated with a negligible dark matter content within the optical disk region (Palunas & Williams 2000; Ratnam & Salucci 2000).

Table 9: Characteristics of the Plummer and Kuzmin models used for the decomposition of the surface-brightness profile and the gas rotation curve of the I Zw 1 host galaxy. The symbol R indicates the radius in cylindrical coordinates, the symbol $r = \sqrt{R^2 + z^2}$ indicates the radius in spherical coordinates.

	Plummer	Kuzmin
Potential	$\frac{-GM_{\text{P}}}{\sqrt{r^2+a_{\text{P}}^2}}$	$\frac{-GM_{\text{K}}}{\sqrt{R^2+(z+a_{\text{K}})^2}}$
Density	$\frac{3M_{\text{P}}a_{\text{P}}^2}{4\pi(r^2+a_{\text{P}}^2)^{5/2}}$	
Surface density	$\frac{M_{\text{P}}a_{\text{P}}^2}{\pi(R^2+a_{\text{P}}^2)^2}$	$\frac{M_{\text{K}}a_{\text{K}}}{2\pi(R^2+a_{\text{K}}^2)^{3/2}}$
Surface brightness	$\frac{L_{\text{P}}a_{\text{P}}^2}{\pi(R^2+a_{\text{P}}^2)^2}$	$\frac{L_{\text{K}}a_{\text{K}}}{2\pi(R^2+a_{\text{K}}^2)^{3/2}}$
Circular speed	$\sqrt{\frac{GM_{\text{P}}R^2}{(R^2+a_{\text{P}}^2)^{3/2}}}$	$\sqrt{\frac{GM_{\text{K}}R^2}{(R^2+a_{\text{K}}^2)^{3/2}}}$

5.6.3 Gravitational Potential Models

The decomposition of the I Zw 1 host galaxy is based on spherical potential models for the bulge and the dark matter halo, and a thin-disk potential model for the disk. The one-dimensional fitting of the J -band surface brightness profile and the gas rotation curve requires the characteristics of the model potentials to be given in terms of surface brightnesses and in-plane circular speeds.

The basic relations of potential theory are taken from Binney & Tremaine (1987). The density ρ of a given potential Φ follows from the Poisson Equation $\rho = (4\pi G)^{-1}\nabla^2\Phi$. Projected along a certain line of sight in the z direction, the density distribution corresponds to a surface density $\Sigma = 2\int_0^\infty \rho dz$. In the case of a thin-disk potential, the total mass $M = \int \rho d^3\vec{x}$ and the surface density are obtained by using Gauss's theorem $\int \rho d^3\vec{x} = (4\pi G)^{-1} \int \vec{\nabla}\Phi d^2\vec{S}$. The circular speed v_c of a particle orbiting at a projected radius R in the plane of the model is given by $v_c^2(R) = R\partial\Phi/\partial R$.

The special potentials used for the decomposition of I Zw 1 are based on the Miyamoto-Nagai gravitational model (Miyamoto & Nagai 1975)

$$\Phi(R, z) = \frac{-GM}{\sqrt{R^2 + \left(a_1 + \sqrt{z^2 + a_2^2}\right)^2}}, \quad (5.2)$$

where G is the gravitational constant and a_1 and a_2 are two scale lengths. The Miyamoto-Nagai potential has the advantage that it provides one consistent description of the spherical Plummer potential and the thin-disk Kuzmin potential. The Plummer potential, resulting from the case $a_1 = 0$, is used as a model for the bulge and the dark matter halo of I Zw 1. The Kuzmin potential, resulting from the case $a_2 = 0$, is used as a model for the disk component. The characteristics of these potentials, computed by means of the formulae mentioned at the beginning of this section, are listed in Table 9. Assuming a constant factor of mass-to-light conversion for each model, the relations for the surface

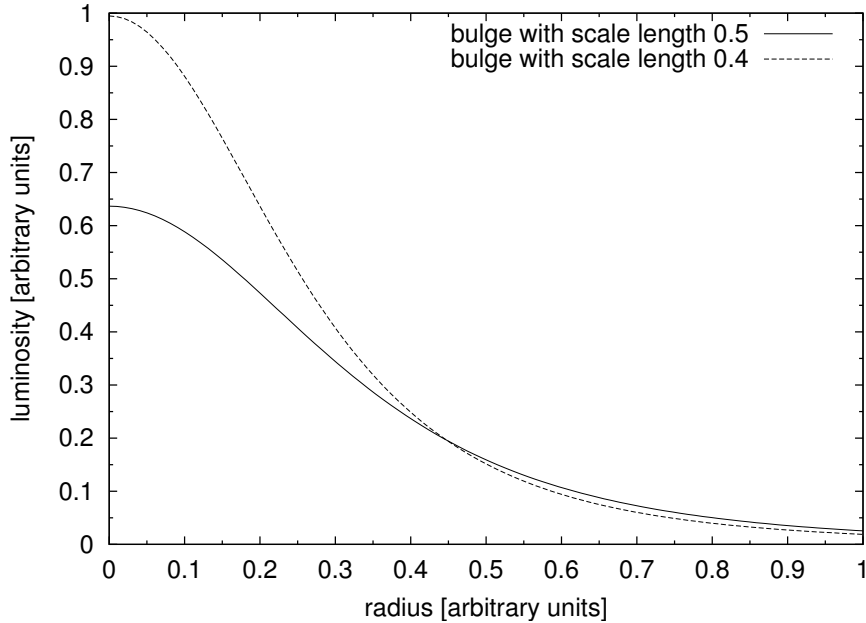


Figure 24: Comparison of two bulge models having the same luminosity parameter but different scale lengths. The units of radius and luminosity are arbitrary.

brightnesses μ can be derived from the relations for the surface densities by replacing masses with luminosities L .

The surface-brightness curve only traces luminous matter. Accordingly, it is modeled by a superposition of a Plummer potential for the bulge and a Kuzmin potential for the disk. This means $\mu_{\text{total}} = \mu_{\text{bulge}} + \mu_{\text{disk}}$, if the surface brightness is given in linear units. In contrast, the dynamics of the gas rotation curve is additionally influenced by the dark matter contained in the halo. This component is modeled by a second Plummer potential so that the circular speed curve is given by $v_{c\text{total}}^2 = v_{c\text{bulge}}^2 + v_{c\text{disk}}^2 + v_{c\text{halo}}^2$.

There are basically two kinds of correlations between the model parameters. First, it is inherent to each individual model that the luminosity or mass parameter and the scale length are correlated with respect to the peak amplitude. As shown in Fig. 24, two bulge models with the same luminosity parameter but different scale lengths have different peak amplitudes.

Second, the two or three potentials for the surface-brightness model and the circular speed model are correlated among themselves by the superposition. This means that an increase in the contribution from one potential requires a decrease in the contributions of other components to adjust the superposition.

5.6.4 Solutions for the Decomposition

The structural decomposition based on the surface-brightness profile and the gas rotation curve requires a two-step curve fitting procedure¹⁰. The first step is the fitting of the stellar brightness distribution with the bulge and disk model, providing the scale lengths and the luminosity parameters of the bulge and the disk component. The scale lengths

¹⁰All fits are done with the GNUPLOT implementation of a non-linear least-squares fitting.

thus derived are used as fixed input parameters for the rotation curve fitting in the second step. This step provides the mass-to-light ratios of the bulge and the disk model together with the scale length and the mass of the additional dark halo component. Uncertainties in both steps of the fitting process are a priori implied in the fixed choice of the model potentials.

Possible scale lengths and luminosity parameters of step one, resulting from different fitting methods for the surface-brightness profile, are presented in Table 10 and visualized in the upper row of Fig. 25. As the surface brightness in the bulge region is directly correlated with the uncertainties in the QSO subtraction, the disk component is adjusted first. This is done by fitting the profile at radii larger than the assumed border radius r_{BD} between the bulge and the disk with the Kuzmin disk model. The upper limit of the fitting range is restricted to $r = 9''$, at which the surface brightness is still clearly above the 3σ limiting surface brightness of the J -band image used for the decomposition. Subsequently, the surface brightness model is adjusted by fitting the bulge parameters in the bulge region $0''.1 < r < r_{\text{BD}}$. As a natural consequence of fitting the disk model first, the final surface brightness model is characterized by a brightness excess in the disk region so that the derived luminosity for the disk represents an upper limit. The resulting fit parameters depend on the radius r_{BD} , chosen as the border between the bulge and the disk. The smaller this radius, the smaller are the disk and bulge scale lengths, the larger is the luminosity parameter of the disk, and the smaller is the luminosity parameter of the bulge. A limited space of possible parameters is studied by testing three different border radii given by $r_{\text{BD}} = 1''.5$ in *Fit A*, $r_{\text{BD}} = 2''.3$ in *Fit B*, and $r_{\text{BD}} = 2''.8$ in *Fit C*.

The rotation curve fitting in the second step is known to be a non-unique problem (e.g. Bosma 2004, and references therein). Similar chi-squares of the fit can be achieved with a range of mass-to-light ratios, depending on which amount of mass is attributed to the dark matter halo. In the case of spiral galaxies like I Zw 1, an independent estimate for the mass in the disk component can be derived from density wave theory. For the case of the medium solution given by *Fit B*, the details of this dynamical argumentation are worked out in the following section 5.6.5.

The solutions for the rotation curve fits starting from the three different bulge and disk scale lengths, yielded by *Fits A*, *B*, and *C*, are presented in Table 10 and Fig. 25. For the sake of lucidity, a naming-convention, directly related to dynamical reasoning, is introduced to classify the fit solutions. In this convention, the disks are named by their maximum circular speeds relative to the maximum disk which is referred to as the case of 100% maximum circular speed (see Fig. 25). This naming convention is suggested, since the scale length of the disk is a fixed parameter in the rotation curve fitting so that the maximum in circular speed always occurs at the same radius. The three fitting methods applied to the rotation curve are the following:

- (i) The extreme maximum disk fit in the second row in Fig. 25 results from a procedure in which only the disk component is fitted to the data at $2'' < r < 12''$ in the first instance. The bulge model is added in the fitting range $0''.2 < r < 12''$. Finally, the whole profile from $0''.2$ to $40''$ is superposed with the halo model. The composite model, therefore, overshoots the measured rotation curve in the disk region.
- (ii) The full solution in the third row of Fig. 25 results from a procedure in which all free parameters of the model components are fitted simultaneously. The fitting range is constrained by $0''.4 < r_{\text{fit}} < 40''$.

Table 10: Parameters of the decomposition resulting from the three solutions of the surface-brightness model given by Fit A, Fit B, and Fit C. The table lists the scale lengths a , the luminosity parameters L , and the mass-to-light ratios M/L for the bulge (B) and the disk (D) component as well as the scale length a and the mass M of the dark matter halo. According to the naming-convention introduced in the text, the solutions of the rotation curve fitting are labeled with respect to the maximum circular velocity of the maximum-disk solution. The solutions are plotted in Fig. 25.

	a_B [$''$]	L_B [$10^{10} L_\odot$]	M_B/L_B [M_\odot/L_\odot]	a_D [$''$]	L_D [$10^{10} L_\odot$]	M_D/L_D [M_\odot/L_\odot]	a_H [$''$]	M_H [$10^{10} M_\odot$]
Fit A ($r_{BD} = 1''.5$)								
100%	0.85	5.35	0.21	2.38	15.49	0.85	23.17	48.17
80%	0.85	5.35	0.32	2.38	15.49	0.55	18.18	44.62
53%	0.85	5.35	0.65	2.38	15.49	0.24	15.09	42.93
Fit B ($r_{BD} = 2''.3$)								
100%	0.88	7.16	0.25	3.08	13.60	1.16	26.38	48.76
78%	0.88	7.16	0.32	3.08	13.60	0.70	19.36	44.44
54%	0.88	7.16	0.54	3.08	13.60	0.33	16.04	43.05
Fit C ($r_{BD} = 2''.8$)								
100%	1.00	8.48	0.30	3.76	12.57	1.45	30.59	50.31
68%	1.00	8.48	0.40	3.76	12.57	0.68	18.92	43.45
47%	1.00	8.48	0.55	3.76	12.57	0.32	16.12	42.84

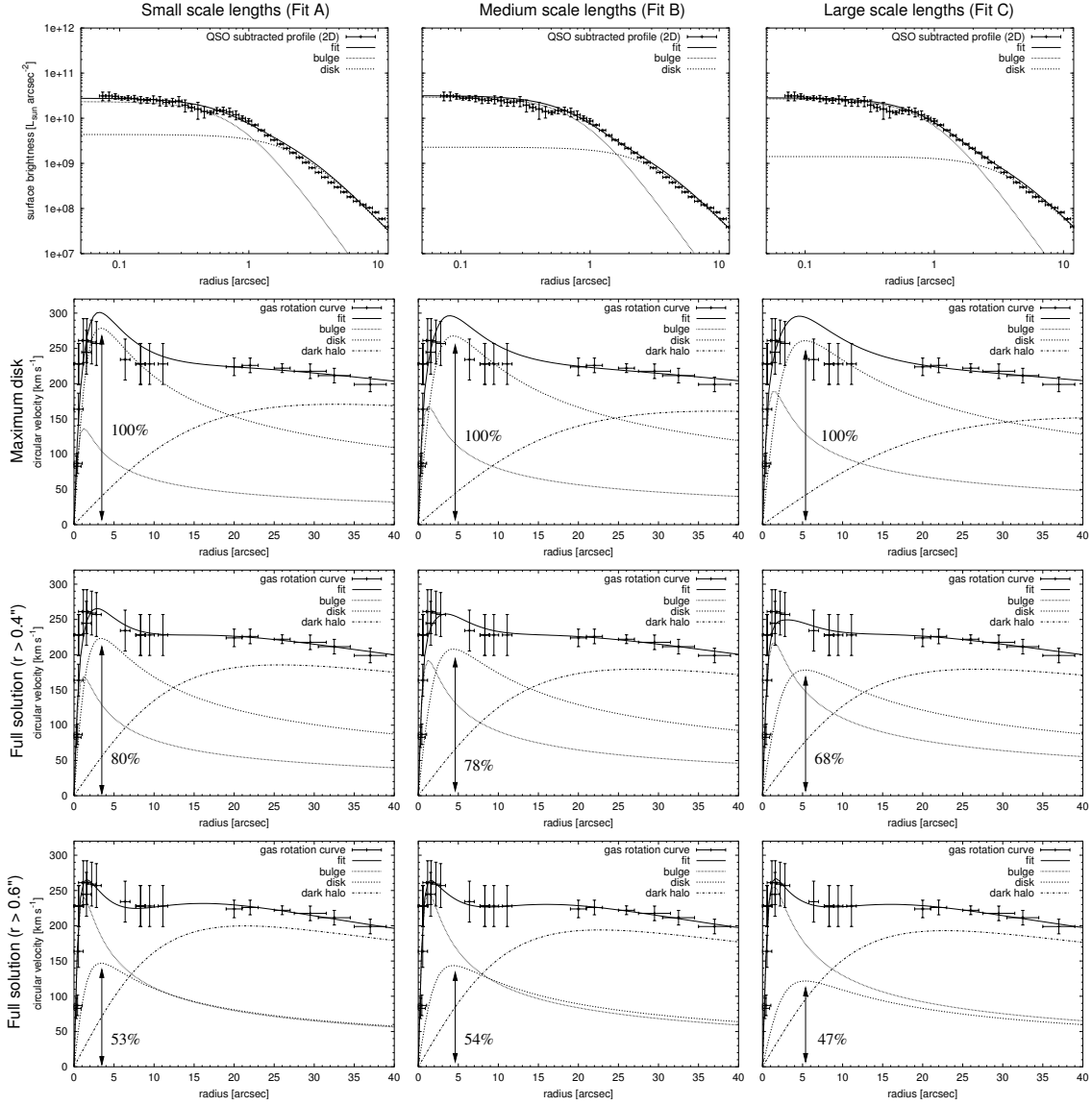


Figure 25: Composite image of the solutions for the decomposition of the surface-brightness profile and the corresponding solutions for the decomposition of the gas rotation curve of the I Zw 1 host. The respective parameters of the fitting solutions are listed in Table 10. The columns show fits based on the scale lengths obtained from Fits A, B, and C of the surface-brightness profile. The respective solution for the surface-brightness fit is plotted in the first row. The corresponding diagrams show the surface brightness in $L_{\odot} \text{ arcsec}^{-2}$ versus the logarithmic radius in arcsec. The solutions for the rotation curve are plotted in the three lower rows. The corresponding diagrams show the circular velocity in km s^{-2} versus the radius in arcsec. As explained in the text, these rotation curve fits include the extreme maximum disk case (second row) and two full solutions (third and fourth row) with fitting ranges starting at $r_{\text{fit}} = 0''.4$ and $r_{\text{fit}} = 0''.6$, respectively. The rotation curve fits along each column are classified according to the naming convention introduced in the text. All plots show the bulge (dotted line), the disk (dashed line), and the dark halo (dash-dot line) as well as the total fit (straight line). A detailed description of the fitting procedures is given in the text.

- (iii) This solution results from the same method as described in (ii) but the fitting range is constrained by $0''.6 < r_{\text{fit}} < 40''$. A comparison with the results obtained from (ii) shows that the solutions differ significantly, depending on the weighting of the data at the smallest radii. The fit in (ii) has a tendency towards a less dominant contribution from dark matter within the disk region.

5.6.5 Dynamical Discussion of the Solution for the Medium Case *Fit B*

The dynamical analysis presented here is based on the theory of swing amplification and provides an independent estimate for the mass contained in the disk component of I Zw 1. The analysis is only done for scale lengths derived from *Fit B*, which represents a medium solution of the three studied cases. As swing amplification does not seem to be at work in the case of a tidally triggered spiral arm (Sundelius et al. 1987), the estimate might not be reliable if the spiral in I Zw 1 is caused by the likely merger process. However, this causality is not yet proved. As the resulting estimate of a 65% disk ranges within the limits given by the rotation curve decomposition, the theory of swing amplification is only considered as a basic consistency check.

Swing amplification is experienced by an initially leading spiral arm when it becomes trailing in consequence of the differential rotation of the galaxy disk. It is a phenomenon of density wave theory and e.g. described in Toomre (1981), Athanassoula (1984), Binney & Tremaine (1987), and Fuchs (2001).

Together with the Toomre parameter Q and the shear rate Γ , the efficiency of swing amplification is determined by the X -parameter. The achieved amplification for different combinations of the three parameters becomes evident from Fig. 26, showing a reproduction of the solutions presented by Athanassoula (1984). The meaning of these parameters, as taken from Athanassoula (1984), and the set most suitable for the case of I Zw 1 is the following:

- The Toomre parameter $Q = \sigma_{\text{obs}}/\sigma_{\text{crit}}$ is defined as the local ratio of the observed stellar velocity dispersion σ_{obs} to the critical velocity dispersion σ_{crit} . The latter is the minimum velocity dispersion required to locally stabilize the disk against gravitational collapse. Spatially resolved measurements of stellar velocity dispersions in distant galaxies just start to become feasible with today's observational techniques. Since no matching data have been obtained for the I Zw 1 host so far, the Toomre parameter remains unknown. However, this lack of information does not degrade the further analysis, since the Toomre parameter only determines the growth factor but not the X at which the growth factor is at maximum. This becomes evident from Fig. 26, showing that the positions of the maxima of the curves do not change with variations in Q .
- The shear rate $\Gamma = -R/\Omega \, d\Omega/dR$ is a dimensionless measure for the change of angular velocity Ω with radial distance R and characterizes the kind of rotation curve. Simple examples are rigid rotation with $\Gamma = 0$, flat rotation with $\Gamma = 1$, and Keplerian rotation with $\Gamma = 1.5$. With a rotation characteristic between that of flat and that of Keplerian rotation, the I Zw 1 host is best approximated by the case $\Gamma \approx 1.2$.
- X is a local parametrization for the contribution of the disk mass to the total mass.

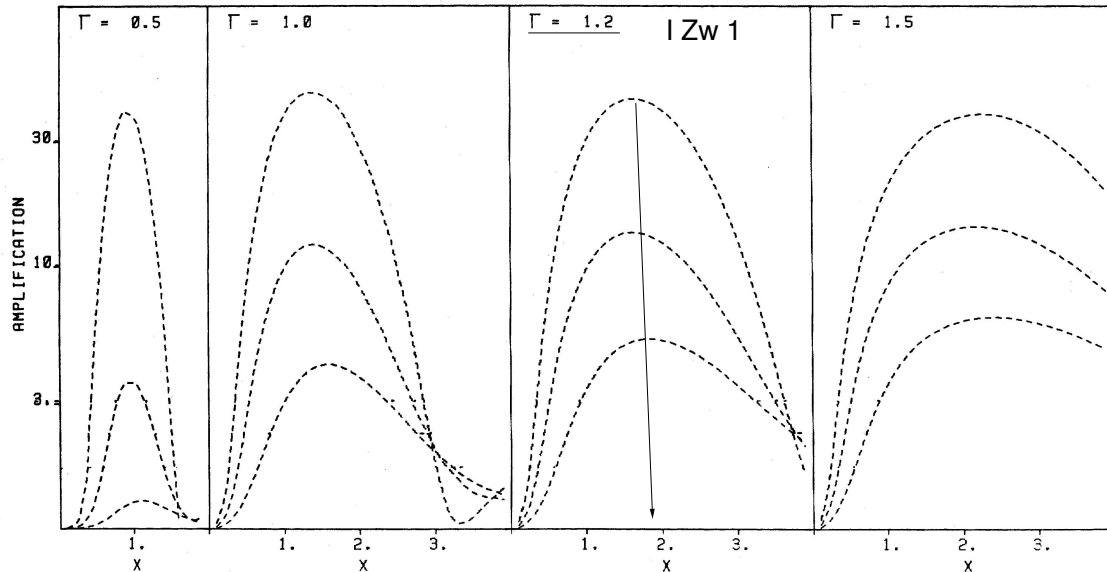


Figure 26: Reproduction of Fig. 26 from Athanassoula (1984), showing the maximum growth factor from a full swing amplification for different sets of the parameters Q , Γ , and X . The values of Γ and X are labeled. The upper, middle, and lower curves correspond to $Q = 1.2, 1.5, 2.0$, respectively. Marks for the approximate set of parameters corresponding to most efficient swing amplification in the case of the I Zw 1 rotation curve are added to the plot.

Fig. 26 shows that for the I Zw 1 host with $\Gamma \approx 1.2$ swing amplification is most efficient at $X \approx 2$.

The disk contribution to the overall mass model depends on the X parameter via the relation

$$X = \frac{R\kappa^2}{2\pi Gm\Sigma_D}, \quad (5.3)$$

where Σ_D , R , κ , G , and m symbolize the disk surface density, the radial distance in the disk, the epicyclic frequency, the gravitational constant, and the number of spiral arms, respectively. In the case of the I Zw 1 host, there are two spiral arms so that $m = 2$. R is taken as the radial distance at which the circular velocity of the Kuzmin disk model for the I Zw 1 host is at its maximum, i.e. $R = \sqrt{2}a_D \approx 4''36$. At this radial distance, the epicyclic frequency can be derived from the rotation curve as $\kappa \approx 73.9 \text{ km s}^{-1} \text{ arcsec}^{-1}$. For this set of parameters and assuming the case of most efficient swing amplification given by $X \approx 2$, Equation (5.3) yields a disk surface density of $\Sigma_D \approx 0.02 \times 10^{10} M_\odot \text{ arcsec}^{-2}$. Translated into the naming convention used for the rotation curve fits, this corresponds to a 65% disk component. As can be seen from Fig. 25 such a solution lies within the limiting cases presented for the medium scale-length *Fit B*.

5.6.6 Dynamical Mass-to-Light Ratios

The discussion of mass-to-light ratios is mainly restricted to the results following from *Fit B* which represents a medium solution for the bulge and disk scale lengths. Depending on the kind of rotation curve decomposition, the mass-to-light ratios in *Fit B* range between $0.25 M_\odot/L_\odot$ and $0.54 M_\odot/L_\odot$ for the bulge component and between $0.33 M_\odot/L_\odot$ and

1.16 M_{\odot}/L_{\odot} for the disk component. This results in mean dynamical J -band mass-to-light ratios of $M_B/L_B = (0.4 \pm 0.2) M_{\odot}/L_{\odot}$ and $M_D/L_D = (0.7 \pm 0.4) M_{\odot}/L_{\odot}$ for the bulge and disk component, respectively. Table 10 shows that *Fit A* tends to result in lower mass-to-light ratios for both components while *Fit C* tends to result in larger ones. It is also evident that the mass-to-light ratios of both components correlate inversely. Larger mass-to-light ratios of the disk involve smaller mass-to-light ratios of the bulge and vice versa.

The bulge mass-to-light ratio of I Zw 1 is at the lower end of the bulge mass-to-light ratios of spiral galaxies reported by Palunas & Williams (2000), while the disk mass-to-light ratio is rather typical. Their results are based on the same Hubble constant as assumed here. Neglecting those entries with a mass-to-light ratio of zero, the data presented in their Table 1 result in a mean mass-to-light ratio of $(1.2 \pm 0.1) M_{\odot}/L_{\odot}$ for the bulge components and of $(2.8 \pm 0.1) M_{\odot}/L_{\odot}$ for the disk components. Their results refer to *maximum disk fits* and the errors given here state the standard deviation of the sample data. The *maximum disk fit* of the *Fits A* through *C* listed in Table 10 result in bulge mass-to-light ratios of $0.2 M_{\odot}/L_{\odot}$ to $0.3 M_{\odot}/L_{\odot}$ and disk mass-to-light ratios of $0.9 M_{\odot}/L_{\odot}$ to $1.5 M_{\odot}/L_{\odot}$. A uncertainty is implied in the fact that the Palunas & Williams (2000) data refer to measurements in the I -band. A direct comparison, thus, strongly depends on the assumed $(J - I)$ color. Since the I - and the J -band are neighboring in the spectrum, the color is expected to be small. An upper limit can be obtained from the magnitude measurements underlying Fig. 7 in Sect. 4.3 or from the spectral energy distribution shown in Fig. 9 of Schinnerer et al. (1998) in consequence of the overlapping error bars. This estimate of 0.9 mag suggests I -band mass-to-light ratios which are at maximum about 2.5 times as large as the J -band ratios. Such a correction factor shifts the disk mass-to-light ratio of I Zw 1 into the range of the mass-to-light ratios found by Palunas & Williams (2000). The bulge mass-to-light ratio of I Zw 1 is still lower than the mean value displayed by the spiral bulges.

5.6.7 Corrections for Stellar Mass-to-Light Ratios

As the mass estimate for the mass-to-light ratios is based on the gas rotation curve, it includes both, the gas mass and the stellar mass. The contribution from the gas has to be subtracted in order to derive stellar mass-to-light ratios. Furthermore, the luminosity derived from the J -band surface brightness has to be corrected for dust extinction. It is obvious that both corrections tend to decrease the mass-to-light ratios: the corrected mass is reduced by subtracting the gas contribution, and the corrected luminosity is increased by adding the light absorbed by dust. As the bulge contains a higher fraction of gas and dust, the corrections are more significant.

- 20% of the total bulge mass is contributed by gas (Schinnerer et al. 1998). The visual extinction of the stellar component in the circum-nuclear region is reported to be about 10 mag (Eckart et al. 1994; Schinnerer et al. 1998). According to the standard interstellar extinction law (Rieke & Lebofsky 1985), this corresponds to a J -band extinction of about 3 mag. Since most of the dust is probably confined to the starburst ring which is only a very central part of the whole bulge component, the mean extinction in the bulge is certainly less than 3 mag. Consequently, the corrected mass-to-light ratio is likely to be between $M_B/L_B = (0.4 \pm 0.2) M_{\odot}/L_{\odot}$ and $(M_B/L_B)_{\text{corr}} \approx 0.02 M_{\odot}/L_{\odot}$.

- The disk component has a mass contribution from cold gas of less than about 7% (Eckart et al. 1994). As the disk is seen almost face-on, the J -band extinction is assumed to be less than about 0.5 mag. Based on these estimates the mass-to-light ratio of the disk is suggested to be in the range of $M_D/L_D = (0.7 \pm 0.4) M_\odot/L_\odot$ and $(M_D/L_D)_{\text{corr}} \approx 0.4 M_\odot/L_\odot$.

In summary, this means for the stellar mass-to-light ratios of the bulge and disk component $0.02 M_\odot/L_\odot \lesssim M_B/L_B \lesssim (0.4 \pm 0.2) M_\odot/L_\odot$ and $0.4 M_\odot/L_\odot \lesssim M_D/L_D \lesssim (0.7 \pm 0.4) M_\odot/L_\odot$.

5.6.8 Mean Stellar Populations

The mass-to-light ratio can be used as an indicator of the mean age of the underlying stellar population. Younger stellar populations which are still composed of an enhanced fraction of hot stars and super-giants have lower mass-to-light ratios than evolved stellar populations.

The stellar mass-to-light ratio of the bulge component of the I Zw 1 host shows a clear trend towards sub-solar values which are likely associated with a young stellar population. This is in agreement with the circum-nuclear starburst activity reported by Schinnerer et al. (1998) as well as the presence of the circum-nuclear molecular ring (Staguhn et al. 2004). Starburst activity close to the active nucleus is also suggested by the strong stellar contribution to the nuclear NIR flux (Eckart et al. 1994; Schinnerer et al. 1998).

As pointed out in Sect. 5.6.4, the method chosen for the decomposition of the surface brightness profile results in a maximum estimate for the total luminosity of the disk component. The same is true for the disk mass yielded by the *maximum disk fit* for the rotation curve. It is, therefore, most likely that the real disk mass-to-light ratio is close to about $1.0 M_\odot/L_\odot$. The fit results even allow for ratios of up to $1.4 M_\odot/L_\odot$. With regard to the fact that the corrections for gas mass and J -band extinction tend to decrease the mass-to-light ratios, these values are still in agreement with the possible younger stellar population suggested by the blue host colors (Hutchings & Crampton 1990) and the star formation activity found for the north-western spiral arm (Schinnerer et al. 1998).

In summary, the mass-to-light ratios seem basically consistent with the conclusions from the two-color diagram (Sect. 5.5.1). Both cases are in agreement with a scenario in which the mean stellar population is younger towards the center of the I Zw 1 host.

Part III

The Case Study of 3C 48

This part deals with the numerical investigation of the merger properties of the 3C 48 host. As outlined in Sect. 2.3, the assumption of a merger process for the 3C 48 host galaxy implies mainly two controversial points: the problem of the apparently missing counter tidal tail and the nature of the second luminosity peak about $1''$ north-east to the QSO. The former problem is essential, since the formation of a significant counter tidal tail would be expected from the merger scenario suggested by the evident north-western tidal extension of the 3C 48 host galaxy. The latter is essential, since 3C 48A could either be the center of a merging galaxy or the hot spot of a jet-gas-interaction, or a peak of light scattered from the QSO nucleus. In the following, the controversies are faced on the basis of a simulation model for the 3C 48 host. The results are published in part in Scharwächter et al. (2004).

6 Methods of Multi-Particle Simulations

Since the first computer simulations for galaxy interactions in the 1970s, multi-particle methods have become an important tool in research on galaxy dynamics. The different approaches range from simple models, assuming galaxies as point masses surrounded by non-selfgravitating disks of test particles, to very sophisticated models, including star formation and following the chemodynamical evolution of a multi-phase medium (Toomre & Toomre 1972; Mihos & Hernquist 1994; Samland & Gerhard 2003). In the multi-particle simulations used here, galaxies are treated as a system of stars, dark matter, and gas, the latter contributing about 10% of the total mass of a spiral galaxy. As the nature of dark matter around galaxies is still unknown (e.g. Bosma 1998), dark matter is modeled in the form of dark stars. Stars and dark matter together form the collisionless component of the galaxies, while the gas requires a hydrodynamical description.

6.1 Basic Dynamics of the Physical System

The following outline of galaxy dynamics shows the physical basis for the numerical treatment by means of multi-particle simulations. It refers to the detailed descriptions given by Binney & Tremaine (1987) and by Combes et al. (1995).

The main interaction between the different mass particles of a galaxy is driven by gravitation. This means that, at any time t , the acceleration exerted on a particle of unit mass is given by

$$\frac{d\vec{v}}{dt} = -\vec{\nabla}\Phi, \quad (6.1)$$

where $\Phi(\vec{x}, t)$ is the gravitational potential generated by all the other mass components. The self-consistent relation between the gravitational potential and the total mass density at any time is described by the Poisson Equation,

$$\nabla^2\Phi = 4\pi G \left[\rho_{\text{gas}} + \int f d^3\vec{v} \right], \quad (6.2)$$

which has already been mentioned in Sect. 5.6.3. While the gas density $\rho_{\text{gas}}(\vec{x}, t)$ is stated explicitly, the density of the dark and luminous mass particles is inferred by integrating the continuous one-particle distribution function $f(\vec{x}, \vec{v}, t)$. As long as the system is collisionless, so that each particle smoothly moves through a mean gravitational potential, this distribution function fully describes the state of the system at any time t in the six-dimensional phase-space. In particular, $f(\vec{x}, \vec{v}, t)$ is constant along any trajectory in the phase-space, as expressed by the Collisionless Boltzmann Equation

$$\frac{\partial f}{\partial t} + \vec{v} \cdot \vec{\nabla} f - \vec{\nabla} \Phi \cdot \frac{\partial f}{\partial \vec{v}} = 0. \quad (6.3)$$

Such a collisionless dynamics is fulfilled in the case of stars in a galaxy. As a consequence of the large number of about 10^{11} stars and the long-range nature of the gravitational force, the accelerations of the individual stars are dominated by the large-scale forces of the system as a whole.

The case is different for the dynamics of the gas component. Besides the gravitational interaction within the gas component and with the stellar system of the galaxy, gas is also governed by the hydrodynamical forces given by pressure gradients and viscosity. The acceleration of a gas element of unit mass follows from the Lagrangian formulation of the Momentum Equation

$$\frac{d\vec{v}}{dt} = -\vec{\nabla} \Phi - \frac{\vec{\nabla} p}{\rho_{\text{gas}}} + \vec{a}^{\text{visc}}, \quad (6.4)$$

where $p(\vec{x}, t)$ is the gas pressure and \vec{a}^{visc} is the acceleration caused by viscous forces. In analogy to the distribution function of the collisionless stellar system, the gas distribution is characterized by the gas density $\rho_{\text{gas}}(\vec{x}, t)$ and the Continuity Equation

$$\frac{\partial \rho_{\text{gas}}}{\partial t} + \vec{\nabla} \cdot (\rho_{\text{gas}} \vec{v}) = 0 \quad \text{or} \quad \frac{d\rho_{\text{gas}}}{dt} = -\rho_{\text{gas}} \vec{\nabla} \cdot \vec{v}. \quad (6.5)$$

The system of hydrodynamical equations is closed by two further equations: the Thermal Energy Equation,

$$\frac{du}{dt} = -\frac{p}{\rho_{\text{gas}}} \vec{\nabla} \cdot \vec{v} \quad (6.6)$$

for the rate of change of thermal energy $u(\vec{x}, t)$ per unit mass, and the Equation of State.

6.2 N-Body Simulations of Collisionless Systems

The numerical method of N-body simulations provides a natural way to simulate a system of masses interacting through gravitational forces. The masses are numerically represented by a number N of particles. Each particle i is attributed with a mass m_i , a position vector \vec{x}_i , and a velocity vector \vec{v}_i and is advanced in time by computing the acceleration caused by the gravitational forces of all other particles j . The computational time required for evaluating the long-range gravitational forces scales as $O(N^2)$. Consequently, the feasible number of particles in N-body simulations¹¹ is, by several orders of magnitude, smaller

¹¹At maximum, several 10^6 to 10^8 particles are feasible with parallelized codes or the special purpose computers GRAPE (GRAvity PipE) which contain a board hard-wired for computing the right hand side of Equation (6.7), (see Makino et al. 2003, and references therein). Approximative algorithms for the force evaluation (Sect. 6.4) allow to treat about 10^4 to 10^5 particles on a PC.

than the number of stars in a galaxy. This means that N-body simulations of collisionless systems are based on a Monte Carlo technique, by incompletely sampling the continuous distribution function $f(\vec{x}, \vec{v}, t)$ with a number of representative particles (see e.g. Dehnen 2001). For this kind of approach, the numerical realization of Equation (6.1) is given by

$$\frac{d^2\vec{x}_i}{dt^2} = - \sum_{j \neq i} Gm_j \frac{\vec{x}_j - \vec{x}_i}{((\vec{x}_j - \vec{x}_i)^2 + \epsilon^2)^{3/2}}, \quad (6.7)$$

where ϵ is the softening length in the case of a softening based on a Plummer sphere. A detailed review about the softening length in N-body simulations and about the problematic of optimal softening can be found in Dehnen (2001). On the one hand, the softening length is required to prevent close encounters between particles and the formation of binaries, which would be artificial in the case of the continuous one-particle distribution function of a collisionless system. On the other hand, softening involves a force error, since it modifies the Newtonian potential for close encounters. The choice of ϵ depends on the conditions and aims of the simulation. A first-order estimate is given by the mean particle separation.

6.3 Smoothed Particle Hydrodynamics (SPH)

The hydrodynamical properties of the gas component in galaxies can be implemented in a numerical N-body treatment, by using *Smoothed Particle Hydrodynamics* (Lucy 1977; Gingold & Monaghan 1977). The following summary is mainly based on the review given by Monaghan (1992).

In SPH simulations, the continuous density distribution of the gas is approximated by a distribution of gas particles. The gravitational attributes of the gas component are directly considered by including the gas particles when computing the gravitational acceleration according to Equation (6.7). The hydrodynamical attributes are recovered from the discrete particle distribution by smoothing the point masses over a smoothing length h , by means of a certain smoothing kernel $W(\vec{x} - \vec{x}_j; h)$. At any time t , the gas density is computed from the total contribution of all smeared masses m_j of the gas particles

$$\rho_{\text{gas}}(\vec{x}) = \sum_{j=1}^N m_j W(\vec{x} - \vec{x}_j; h), \quad (6.8)$$

which directly implies the Continuity Equation (6.5). In analogy, any other hydrodynamical quantity $w(\vec{x}, t)$ as well as the derivative $\vec{\nabla} w(\vec{x}, t)$ can be derived from the smoothed estimates

$$w(\vec{x}) = \sum_{j=1}^N m_j \frac{w_j}{\rho_j} W(\vec{x} - \vec{x}_j; h) \quad \text{or} \quad \vec{\nabla} w(\vec{x}) = \sum_{j=1}^N m_j \frac{w_j}{\rho_j} \vec{\nabla} W(\vec{x} - \vec{x}_j; h), \quad (6.9)$$

respectively. These interpolations can be improved by using different kinds of symmetrizations (see e.g. Monaghan 1992; Hernquist & Katz 1989). One example of an implementation of the hydrodynamical part of the Momentum Equation (6.4) for gas particle i is based on the relation $(\vec{\nabla} p/\rho) = \vec{\nabla}(p/\rho) + (p/\rho^2)\vec{\nabla}\rho$ and given by

$$-\frac{\vec{\nabla} p_i}{\rho_i} + \vec{a}_i^{\text{visc}} = - \sum_{j=1}^N m_j \left(\frac{p_j}{\rho_j^2} + \frac{p_i}{\rho_i^2} + \Pi_{ij} \right) \vec{\nabla}_i W(\vec{x}_i - \vec{x}_j; h), \quad (6.10)$$

where the pressure gradient is symmetrized using an arithmetic mean (Monaghan 1992). The viscous acceleration \vec{a}^{visc} is numerically represented by the artificial viscosity Π_{ij} which is added to the pressure gradient. Artificial viscosity is necessary for the numerical treatment of shocks. The standard implementation (Monaghan 1989) of artificial viscosity is given by

$$\Pi_{ij} = \begin{cases} \frac{-\alpha \bar{c}_{ij} \mu_{ij} + \beta \mu_{ij}^2}{\bar{\rho}_{ij}}, & \text{if } (\vec{v}_i - \vec{v}_j) \cdot (\vec{x}_i - \vec{x}_j) < 0 \\ 0, & \text{if } (\vec{v}_i - \vec{v}_j) \cdot (\vec{x}_i - \vec{x}_j) \geq 0, \end{cases} \quad (6.11)$$

with

$$\mu_{ij} = \frac{(\vec{v}_i - \vec{v}_j) \cdot (\vec{x}_i - \vec{x}_j) h}{|\vec{x}_i - \vec{x}_j|^2 + \eta^2 h^2}. \quad (6.12)$$

In these equations, \bar{c}_{ij} and $\bar{\rho}_{ij}$ are the average sound speed and the average density of the particles i and j , respectively, and η is a small parameter needed to prevent singularities. The parameter α fits the term linear in μ_{ij} , which represents a bulk viscosity. This term is required to suppress post-shock oscillations. The parameter β fits the term quadratic in μ_{ij} , which represents a von Neumann-Richtmyer artificial viscosity. This term is required to handle shocks at high Mach numbers. The exact choice of both parameters is uncritical. Typical combinations used for galaxy simulations are given by $\alpha = 1.0$ and $\beta = 2.0$, or $\alpha = 0.5$ and $\beta = 1.0$ (Hernquist & Katz 1989; Mihos & Hernquist 1994; Hernquist & Mihos 1995).

6.4 The Hierarchical Tree Method

The hierarchical tree method (Barnes & Hut 1986) is an approximative method to overcome the constraints of the $O(N^2)$ scaling of the computation time needed for the force evaluation. The summary is taken from the review of the hierarchical tree method presented by Pfalzner & Gibbon (1997).

The basic idea of the hierarchical tree method is to sort all particles into a nested cell structure, according to their positions in space. Starting from the root cell, which contains all particles, the tree is built in d dimensions by successively subdividing cells into 2^d subcells. Continued as long as there is more than one particle per cell, this sorting naturally adapts to the spatial distribution of particles and, in particular, to the strong density contrasts, present in galaxy simulations. During the force evaluation for a certain particle, each cell for which the ratio of size s to distance D results in $s/D < \Theta_{\text{crit}}$ is treated as a pseudo-particle which contributes to the gravitational force as a whole. The accuracy can be increased by taking into account higher multipole moments of the pseudo-particle cells. For an intermediate accuracy of $0.1 < \Theta_{\text{crit}} < 1.0$, the hierarchical tree method is characterized by a computation time scaling with $O(N \log N)$. This means a considerable gain with respect to the intrinsic $O(N^2)$ scaling of N-body codes. With a small loss of accuracy, the hierarchical tree method provides a software solution for handling particle numbers of up to 10^5 on a single-processor PC.

7 Simulations

There are basically two kinds of research on galaxy dynamics done by means of multi-particle simulations.

In one case, multi-particle simulations serve as a tool to expose model galaxies to a variety of experimental setups like in laboratory experiments. Within the limits given by the physical completeness of the numerical representation, these simulations yield general insights into the physical response of model galaxies on certain input parameters.

The simulations presented here belong to a second kind of research in which multi-particle simulations are used as an interpretative tool for real observational data. This kind of simulation is important since observations of galaxies suffer from two basic restrictions: First, they are restricted to spatial projections as a consequence of the large distance-scales in the Universe. Second, they are restricted to snapshots in time as a consequence of the long evolutionary time-scales. The aim of the simulations, therefore, is a three-dimensional interpretation of the observed projected structures as well as an interpretation of the possible past and future evolution. Since neither the observational data nor the numerical description is unique and complete, the models are rather qualitative than quantitative representations. In particular, the vast parameter space of possible initial conditions for the simulations prohibits a one-to-one time extrapolation of the evolutionary track. As a direct link between real observations and the simulations of the first kind, the qualitative galaxy models help to iteratively improve both, the observational approach and the reliability of the theoretical results about galaxy dynamics.

7.1 The Collisionless Simulation for 3C 48

The subject of the investigation here is the likely galaxy merger 3C 48. A purely collisionless merger simulation, resulting in a 3C 48 model, is presented first. Afterwards a gas component is added to this simulation to analyze the basic effects on a hydrodynamical component. In view of the basic uncertainties intrinsic to the multi-particle modeling, the unknowns of the parameter space for the collisionless model are tackled in a rather heuristic manner. Only one merger simulation with a single set of initial parameters is scanned for a 3C 48 model at different time steps and different projection angles. These initial parameters are suggested by comparing the observational information about 3C 48 with parameter space studies of merger simulations published in literature.

A priori, the possible parameter space is spanned by the number of galaxies involved in the interaction, their individual physical properties, and the orbital configuration of the interaction. As the most straightforward approach to a qualitative model, the simulations for 3C 48 are initialized as a merger between two equal-mass spiral galaxies. This is motivated by the following basic considerations:

- A major merger between two progenitor galaxies of comparable sizes is suggested by the strongly disturbed morphology of the 3C 48 host galaxy as well as the typical star formation clumps in the north-western tidal tail (Canalizo & Stockton 2000).
- Simulations have shown that major mergers between two spiral galaxies result in an elliptical merger remnant (see Sect. 10 and references therein). Since the morphology of the main body of the 3C 48 host is already reminiscent of an elliptical galaxy, it is likely that such a type of galaxy will be the final result of the relaxation process in 3C 48.

Table 11: *Initial parameters of the two identical galaxies in the system of units, suitable for 3C 48. Each galaxy consists of a spherical non-rotating bulge, a rotating exponential disk, and an isothermal halo (Hernquist 1993).*

Parameter	Bulge	Disk	Halo
Number of particles	8 000	8 000	8 000
Mass [$10^{10}M_{\odot}$]	1.86	5.60	32.48
Scale length [kpc]	0.88	3.50	35.0
Scale height [kpc]		0.7	
Maximum height [kpc]		7.0	

- Finally, there is no obvious companion galaxy to 3C 48. Assuming a merger process at all, the 3C 48 host probably is in an advanced state.

7.1.1 The Initial Galaxy Models

Restricting to spiral galaxies by the above considerations, the two progenitor galaxies are initialized identically. Both consist of a bulge, a disk, and a halo. The presence of a compact bulge component in at least one of the progenitor galaxies of 3C 48 is suggested by the strong present starburst activity in an obviously advanced merger state (Canalizo & Stockton 2000). As mentioned by Canalizo & Stockton (2000), the multi-particle simulations presented by Mihos & Hernquist (1996) show that a compact bulge can delay the gas inflow and the associated starburst activity until the final stages of the merger. On the contrary, gas inflows and starbursts in merging galaxies without bulge components happen at a very early phase of the interaction and rapidly subside before the actual merging of the galaxies.

The particle distributions for each of the bulge-disk-halo galaxies is initialized by using the program BUILDGAL (Hernquist 1993). In this program, the bulge is chosen as a spherical mass distribution with the radial density profile

$$\rho(r) = \frac{M}{2\pi} \frac{a}{r(r+a)^3}, \quad (7.1)$$

where a is the scale length of the bulge. The disk is modeled with an exponential radial density profile and the profile of an isothermal sheet in the vertical direction. This mass distribution is mathematically given by

$$\rho(R, z) = \frac{M}{4\pi h^2 z_0} \exp(-R/h) \operatorname{sech}^2(z/z_0), \quad (7.2)$$

where h and z_0 are the radial and the vertical scale length, respectively. The dark matter is represented by an isothermal halo, according to

$$\rho(r) = \frac{M}{2\pi^{3/2}} \frac{\alpha \exp(-r^2/r_c^2)}{r_c(r^2 + \gamma^2)}, \quad (7.3)$$

where r_c and γ are the tidal and the core radius, respectively, and α is a normalization constant given by $\alpha = (1 - \sqrt{\pi}(\gamma/r_c) \exp(\gamma^2/r_c^2)(1 - \operatorname{erf}(\gamma/r_c)))^{-1}$. In the program, the

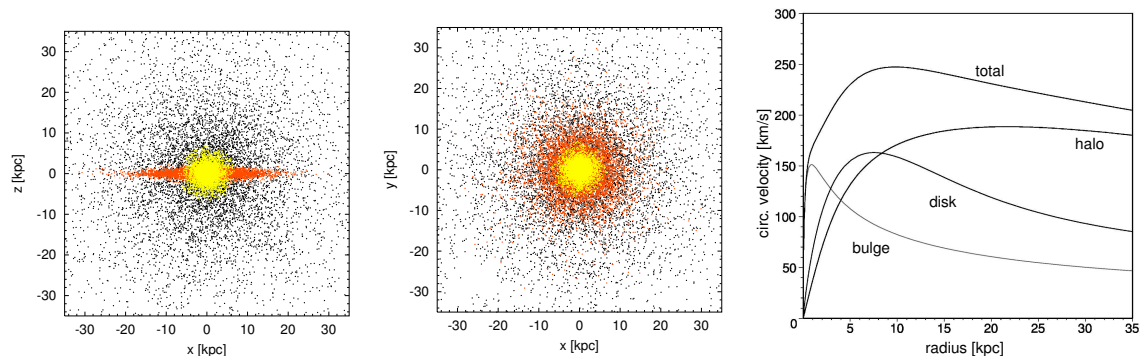


Figure 27: *The initial galaxy model, composed of a bulge, a disk, and a dark halo component. Particle scatter-plots of the galaxy models in an edge-on (x - z plane) and a face-on (x - y plane) view onto the disk component are shown in the left and the middle panel, respectively. Bulge particles are colored yellow, disk particles red, and halo particles black. The total rotation curve of the galaxy model and the individual contributions from the bulge, the disk, and the dark halo component are shown in the right panel. The system of units is the one applying to the 3C 48 model.*

velocities of the particles are initialized, by using moments of the Collisionless Boltzmann Equation (6.3). This approach provides galaxy models sufficiently close to physical equilibrium in order to study galaxy mergers (Hernquist 1993).

The parameters applying to the two identical galaxy models used for the 3C 48 simulations are listed in Table 11. The particle distributions and the corresponding rotation curve are visualized in Fig. 27. With these parameters, both identical models have bulge-to-disk scale length ratios of 0.25 and bulge-to-disk mass ratios of 0.33. Bulge-to-disk luminosity ratios are observationally used as discriminators of Hubble type, although they correlate only weakly and also depend on the observation band (de Jong 1996). By simply assuming a constant mass-to-light conversion of unity, the bulge-to-disk ratio of 0.33 is on average comparable to that of Sb type galaxies (de Jong 1996, see Figs 20 and 21 therein).

7.1.2 The Orbital Configuration

The asymmetric morphology displayed by the 3C 48 host suggests a non-coplanar orientation of the two disk galaxies involved in the likely merger. In consequence of the bi-symmetric nature of tidal forces, galaxy-galaxy interactions are characterized by a tidal bridge between the interaction partners and by a tidal tail at the far sides of each galaxy (Toomre & Toomre 1972). As the merger advances, the tidal bridges disappear between the merging galaxy centers. At first, the tidal tails remain as the most prominent extensions until they finally fall back onto the merger remnant. Assuming a co-planar orbital configuration, such a merger between two equal-mass galaxies is associated with in-plane symmetry of the respective tidal tails. This kind of symmetry is obviously not present in the case of the 3C 48 host, as the significant north-western tidal tail has no similar counterpart. From merger simulations, two scenarios are possible to account for the obvious asymmetry:

- (i) The asymmetry of the tidal tails could be intrinsic to the galaxy merger. It is known that galaxies with massive and steep dark matter halos do not form extended tidal tails during the merger (Dubinski et al. 1999). The authors find that the projected

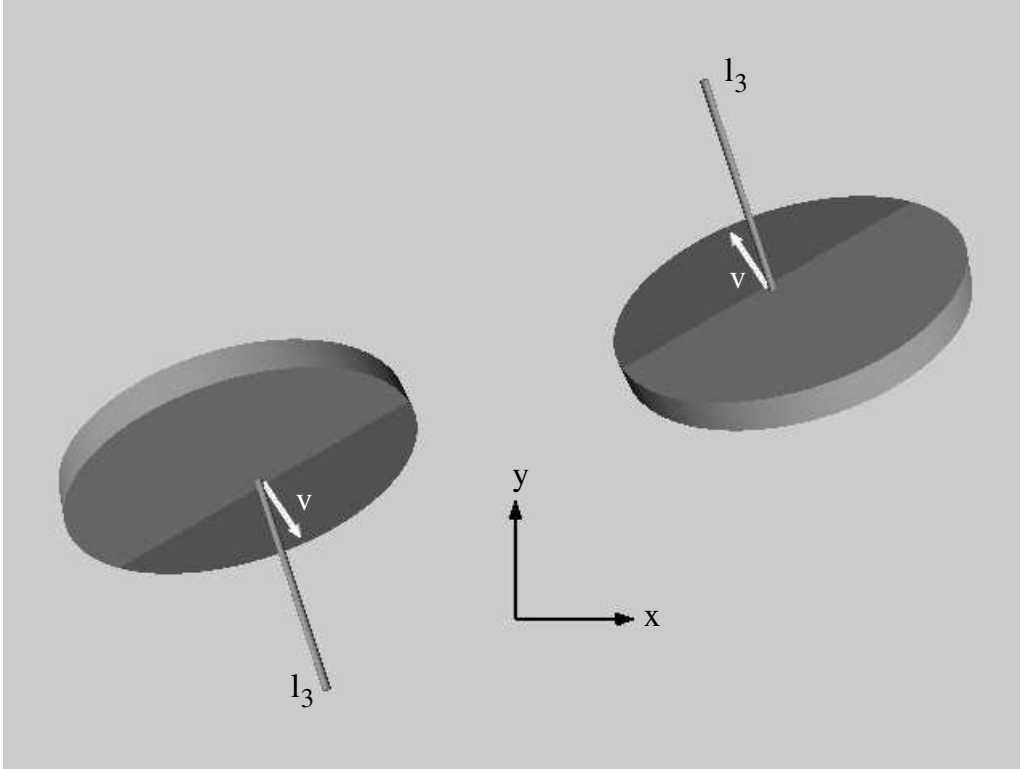


Figure 28: Sketch of the initial orbital configuration of the two disks for the 3C 48 simulations as seen along the positive z -axis onto the orbital plane. The disks are shown with a radius of seven times their scale lengths, i.e. 24.5 kpc, and their positions on the orbit are shown in the same system of units. In order to visualize the small initial orbital velocities of both galaxies, the velocity vectors are scaled by a factor of 12. Their orientation is explained in the text. The spin directions of both galaxies are indicated by the spin vectors l_3 in the coordinate system fixed to the galaxies. (Graphics based on POV-Ray (see <http://www.povray.org/>.)

extension of the tidal tails correlates with the ratio of the escape velocity to the circular velocity at the outermost radii of the galaxy disk. If the ratio is larger than 2.5, tidal tail formation is inhibited by the deep and steep potential wells of the corresponding dark matter halos. In this respect, the rotation curves of galaxies are a discriminator for tidal tail formation: Extended tidal tails are only formed when the merging galaxies have rotation curves which are declining at the outermost radii of the disks.

- (ii) The asymmetry of the tidal tails could be caused by observational projection effects if the tidal tails have complex three-dimensional morphologies. Such morphologies are found in inclined mergers between equal-mass disk galaxies. A standard example for such an inclined merger is the configuration used for simulating the interacting galaxy pair of NGC 4038 and 4039, known as *the Antennae* (e.g. Toomre & Toomre 1972; Barnes 1988).

The simulations for 3C 48 presented here are done to investigate the second scenario. In order to test whether the morphology of the 3C 48 host can be reproduced by a special projection during the merger of two equal galaxies, both galaxies are designed to be able

to form extended tidal tails. This can be seen from the fact that the rotation curves of the model galaxies decline at large radii (Fig. 27).

The inclined orbital configuration for the 3C 48 simulations is sketched in Fig. 28. The orientation of both galaxies is given with respect to a right-handed coordinate system which is fixed by the x - y -direction of the orbital plane and originates in the center-of-mass of each galaxy. Before the set up, both galaxy disks are aligned with the orbital plane and have spin vectors parallel to the fixed z -axis. In the first step of the rotation, the galaxies are inclined by 60° around the x -axis. In the second step, the lines of intersection between the disks and the orbital plane are rotated around the fixed z -axis by 30° and 210° , respectively. The 3C 48 simulation is started near the apocenter of an initially elliptical Keplerian orbit defined by an eccentricity of 0.81 and a pericentric distance of 6 kpc.

7.1.3 The Simulation Run

The time evolution of the interacting galaxy models is computed by using the multi-particle tree-code TREESPH, Version 10, November 7, 1988, (Hernquist & Katz 1989), kindly provided by Prof. Dr. L. Hernquist. The hierarchical tree method is used together with a tolerance criterion of $\Theta_{\text{crit}} = 0.7$ for the force evaluation. The force evaluation includes quadrupole terms of the mass distribution in the cells. The time step is fixed to 1 Myr for all particles and the particle configuration is dumped into snapshot files after each twentieth time step. This means that the evolution of the system is sampled in steps of about 21 Myr for later analysis purposes. Since the mean particle distance increases from the bulge across the disk to the halo components, the particles of each component are assigned to a particular softening length according to $\epsilon_B = 0.21$ kpc, $\epsilon_D = 0.28$ kpc, and $\epsilon_H = 1.4$ kpc, respectively. These softening lengths are kept constant during the simulation.

7.1.4 Methods of Comparison with Observations

The evaluation of the 3C 48 models is done double-tracked, using morphological information on the one hand and stellar kinematical information on the other hand. The observational reference data are taken from Canalizo & Stockton (2000), who show U' - and R' -band images, centered at respective wavelengths of $0.341 \mu\text{m}$ and $0.612 \mu\text{m}$, and who present a stellar-kinematical analysis of optical spectra. An additional near-infrared image of the 3C 48 host, composed of the data discussed in Zuther et al. (2004), was kindly provided by Jens Zuther in digitized form (see Fig. 31).

A contour plot of an R' -band image of the 3C 48 host galaxy, after subtraction of the QSO contribution, is shown in Fig. 1 of Canalizo & Stockton (2000) and reproduced as the underlying graphics in Fig. 29. This plot is used for measuring the basic proportions of the host galaxy by several parameters. As sketched in Fig. 29, the morphology is parametrized by the lengths $L1$ and $L2$, measured along the longest extension of the host galaxy, the widths $W1$ and $W2$, measured perpendicular to the longest extension, and the distance D to the tip of the north-western tidal tail. The longest extension is found along a position angle of 4° with respect to the north-south direction. The dimensionless ratios of these parameters are used as figures of merit for a scale-independent comparison between the models and the observed 3C 48 host.

The length scaling has to be fixed when investigating the models by direct overlays on real images of 3C 48. This kind of direct comparison requires the simulation data

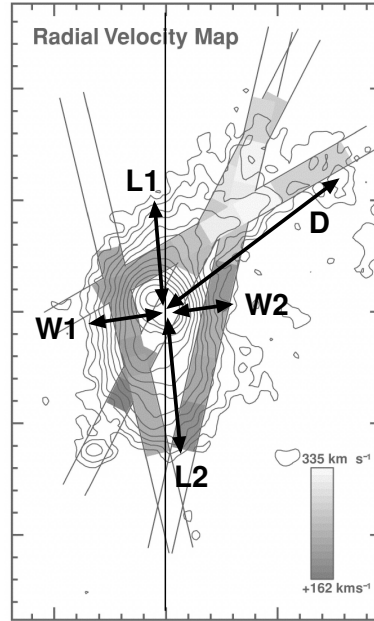


Figure 29: Schematic view of the parameters used for characterizing the dimensions of the 3C 48 host galaxy. The basic morphological parameters are overlaid on the R' -band ($0.612 \mu\text{m}$) image reproduced from Fig. 1 of Canalizo & Stockton (2000). According to the authors, the major tick-marks correspond to $5''$. This figure is presented by Canalizo & Stockton (2000) to visualize the slit settings along which they present mean stellar line-of-sight velocities. The authors show the derived line-of-sight velocities in the form of the grey-shading.

to be available in a pseudo-observational format. Therefore, the three-dimensional simulation data are converted as two-dimensional projections into array images, identical to telescope observations. The program SIM2OBS, developed for this purpose, is described in Appendix B. The pixel luminosity is computed proportional to the number of particles without regard to the different masses of the particles. This choice is motivated by the fact that a number-density weighting is likewise artificial as a mass-density weighting, considering that the actual mass-to-light ratios of the model particles are unknown. In view of the purely qualitative approach to a 3C 48 model, the comparison is done for the basic model morphology only. Besides the particle numbers, SIM2OBS is used to compute the mean particle line-of-sight velocities for each pixel. The data are provided as two-dimensional velocity arrays. Empty array pixels are set to a line-of-sight velocity of zero. This step is implied in the smoothing procedure by first multiplying the mean line-of-sight velocities of each pixel by the respective number of particles. The product is afterwards smoothed by a Gaussian convolution and divided by the equally smoothed particle number array. The derived line-of-sight velocity field is used for a comparison with stellar line-of-sight velocities in the 3C 48 host, derived by Canalizo & Stockton (2000) from optical long-slit spectra along four different settings. The slit settings are indicated in the reproduction of Fig. 1 of Canalizo & Stockton (2000) in Fig. 29. Once the scaling of the model is fixed, the slit settings are reproduced on the model velocity array. The velocity projections along the four slits are compared to the observed stellar line-of-sight velocity projections taken from Table 2 in Canalizo & Stockton (2000).

The three kinds of comparison are carried out for the range of possible projection angles

Table 12: *Model parameters of the gaseous and the collisionless disk used for the 3C 48 gas simulation. The collisionless disk is the same as in the collisionless model described in Table 11. The system of units is the one applying to the 3C 48 model.*

Parameter	Gas disk	Collisionless disk
Number of particles	8 000	8 000
Mass [$10^{10}M_{\odot}$]	0.168	5.60
Scale length [kpc]	2.8	3.50
Scale height [kpc]	0.07	0.7

of model snapshots from consecutive times of the merger simulations. The projection range is first sampled in steps of 20° for all combinations of these rotations which cause a change in the projected appearances of the snapshots. These are the rotations around the fixed axes x and y in terms of the rotations specified in SIM2OBS (Appendix B). The third rotation around the z axis, which is oriented perpendicular to the projection plane, is only adjusted for the final model to match the 3C 48 orientation on the sky.

7.2 The Simulation with Gas

In a second step, the collisionless simulation for 3C 48 is complemented with a gaseous component. The basic parameters, concerning the collisionless part of the initial galaxy models and the orbital configuration, are adopted from the collisionless simulation. The additional gas component is modeled, using the implementation of Smoothed Particle Hydrodynamics (Sect. 6.3) provided by TREESPH.

In order to continue the rather qualitative than quantitative comparison of the collisionless model, the gas is simply considered as a non-gravitating component with hydrodynamical properties. For this purpose, TREESPH is modified so that only stellar particles are loaded into the tree structure when computing the gravitational interaction. The approach allows to qualitatively investigate the gas response to the strong perturbations in the stellar potential occurring during the merger.

7.2.1 The Gas Component of the Initial Galaxy Model

By means of the program BUILDGAL (see Sect. 7.1.1 and Hernquist 1993), gas particles are added to the initial galaxy models used for the collisionless merger simulation for 3C 48. The parameters chosen for the collisionless components of the bulge, the disk, and the halo are the same as listed in Table 11. The gas particles are distributed in a gaseous disk, using the exponential density profile of Equation (7.2) like in the case of the collisionless disk. The models for the gas disk and the collisionless disk are compared in Table 12 and Fig. 30. The gas disk is initialized with a smaller scale length and scale height than the stellar disk. By this, the gas particles are embedded in the gravitational potential of the collisionless disk and not subject to edge effects. In the case of gas particles which are unable to move on intersecting orbits, the exponential disk involves a singularity in the center. In the program BUILDGAL, this singularity is avoided by setting an inner cut-off radius, which is chosen as 0.175 kpc here. Each gas particle is attributed with a constant temperature of 10 000 K.

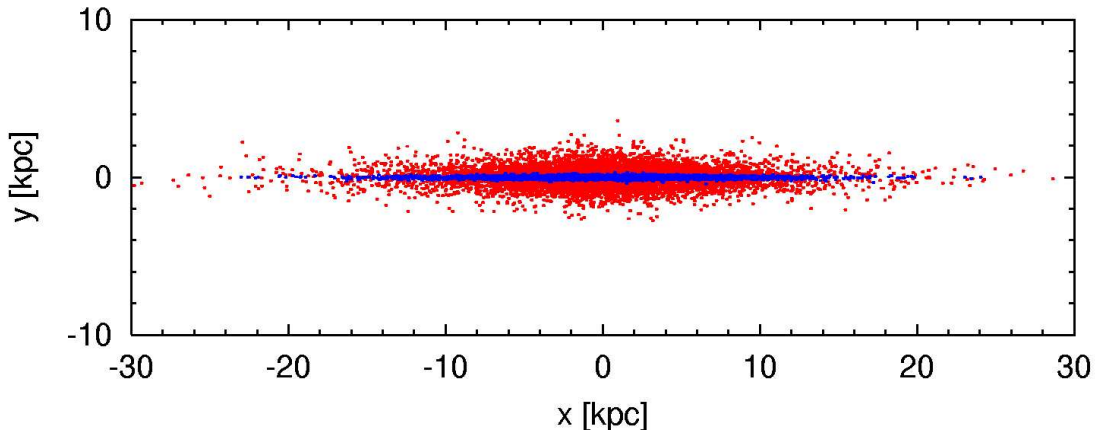


Figure 30: Comparison of the gaseous (blue) and the collisionless (red) disk components of the initial galaxy model with gas. The plot shows an edge-on view in a particle scatter representation. Distances are given in the units of the 3C 48 model.

The errors implied in neglecting the gravitational contribution of the gas are small if the total gas mass is negligible with respect to the stellar mass of the galaxy. Therefore, the gas mass in each of the two model galaxies is chosen as $1.68 \times 10^9 M_{\odot}$, which corresponds to 3% of the stellar mass contained in the galaxy disks. This total gas mass of the simulation is not comparable in quantity to the gas reservoir of a few times $10^{10} M_{\odot}$, resulting from observations of the 3C 48 host (Scoville et al. 1993; Wink et al. 1997). However, the observed gas mass is also uncertain as it is based on an uncertain conversion factor used to compute molecular gas masses from integrated CO intensities.

7.2.2 The Simulation Run

The simulation is started with the same orbital configuration as described for the collisionless simulation in Sect. 7.1.2. Since the gas component is treated as massless, the parameters of the Keplerian orbit are identical to the ones used for the collisionless run.

The Smoothed Particle Hydrodynamics part of TREESPH is based on the methods described in Sect. 6.3. The gas particles have constant softening and smoothing lengths of 0.21 kpc. As the time integration in TREESPH is computed with an explicit leapfrog method, the maximum time step allowed for a stable hydrodynamical description of the gas particles is given by the Courant criterion¹². In the individual time step scheme provided by TREESPH, each particle can adopt time steps of size 2^{-n} times the system time step up to a specified minimum. For the gas simulations here, the smallest possible time step is set to 1/128 of the system time step of 1 Myr. The two smallest time steps remain virtually unpopulated until the 3C 48 model emerges.

Artificial viscosity is used in the form given by Equations (6.11) and (6.12) with $\alpha = 0.5$ and $\beta = 1.0$. The gas is treated as an isothermal component based on the isothermal

¹²The size of the time step Δt is limited by the Courant criterion $\Delta t \leq \Delta x / |\vec{v}|$. It guarantees causality for the given spatial resolution element Δx and the given physical velocity $|\vec{v}|$ of the wave in explicit finite differencing schemes, in which the solution at a computation node at $t + \Delta t$ is derived from the nodes at earlier times. A general description can be found in Press et al. (1992). The detailed form of the Courant criterion applying to TREESPH is explained by Hernquist & Katz (1989).

Equation of State $p = c^2 \rho_{\text{gas}}$. In this case, the gas density ρ_{gas} is directly related to the gas pressure p via the isothermal sound speed c , and the Thermal Energy Equation (6.6) is redundant (see Hernquist & Katz 1989).

8 Results

In the following, the 3C 48 model resulting from the merger simulation is discussed in comparison to observational data and with respect to the model solutions for the second tidal tail and 3C 48A. After the collisionless model, the gas model is presented and compared to observed properties of the molecular gas in 3C 48.

8.1 The Collisionless Model for 3C 48

The simulation of a merger between two equal-mass inclined disk galaxies provides a 3C 48 model at a certain projection angle, 461 Myr after the start of the simulation. This shows that the 3C 48 host galaxy can be explained as the result of a merger process. The 3C 48 model is not a one-to-one look-alike but displays many qualitative similarities to the 3C 48 host.

The merger simulation as well as the projection angle applied to reproduce the 3C 48 model are visualized in Fig. 31 together with a near-infrared image of the 3C 48 host provided by courtesy of Jens Zuther. The plots only show the luminous particles of the bulges and disks. The dark halo particles are suppressed. The upper row demonstrates the time evolution of the merger process viewed perpendicular to the orbital plane. This corresponds to the projection angle for which the merger remnant shows basic similarities to the Antennae galaxies. In the lower row, the merger remnant is rotated to match the projected appearance of the 3C 48 host. The last two panels are shown in a density visualization with decreasing resolution. In terms of astronomical imaging data, this means an increase of background noise.

With respect to the non-rotated frame, which corresponds to a view onto the orbital plane along the positive z -axis (left panel of Fig. 32), the 3C 48 model emerges under a projection in which the orbital plane is tilted southwards, westwards, and counterclockwise by 120° , 160° , and 116° , respectively (right panel of Fig. 32).

8.1.1 Merger Orbit and Time Scales

In consequence of their extended mass distributions, the interacting galaxies follow a decaying orbit instead of the initialized Keplerian one. The decaying orbit of the galaxies is visualized in Fig. 33 in the frame of the reduced one-body system. This means that the plot shows the distance vector between the centers-of-mass of the two galaxies. In one case, the centers-of-mass are computed from the luminous particles of the disk and bulge components. In the other case, the computation is done for the dark halo particles. The time evolution of the decaying orbit can be seen from the intervals of data points which correspond to a fixed time interval of 21 Myr.

The different behavior of the orbit traced by the luminous particles and the one traced by the dark particles emphasizes the different relaxation time scales. As a consequence of the short dynamical time scales in the inner regions of the galaxies, the orbit traced by the luminous particles decays more violently than the one traced by the particles in the extended dark matter halos. Particularly, at the final time step shown in Fig. 33, the centers-of-mass of the luminous particles have already merged, while the dark orbit is still offset from zero. A typical time scale for the relaxation in the inner regions of merger remnants is of the order of 100 Myr, while the outer regions relax on scales of several Gyr (e.g. Mihos 1999).

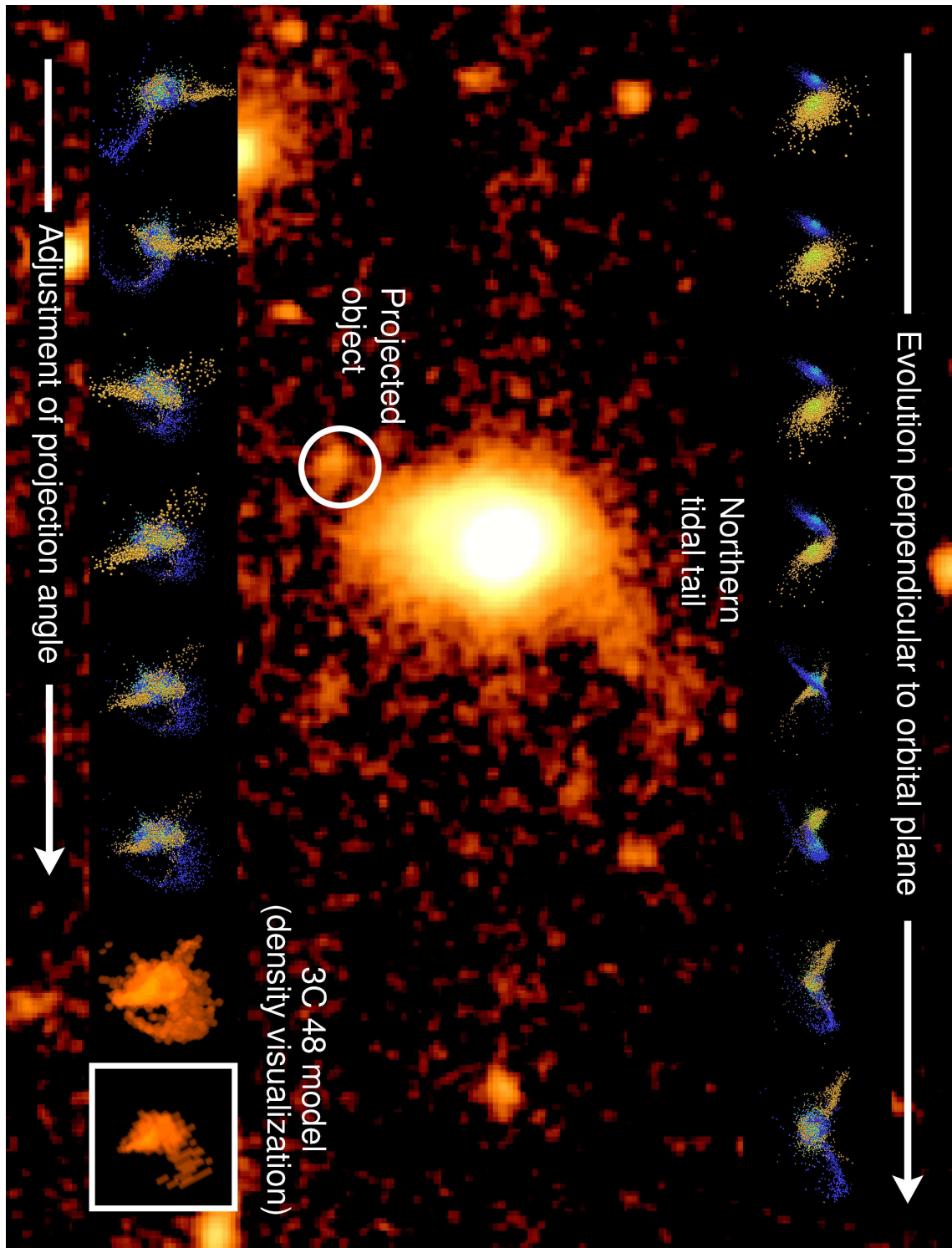


Figure 31: Time evolution of the 3C 48 simulation, viewed perpendicular to the orbital plane, and projection angle of the best-fitting 3C 48 model. The plot is complemented with a near-infrared image of the 3C 48 host provided by courtesy of Jens Zuther. The particle and density visualization of the model results are created by using the Open Visualization Data Explorer together with a special purpose application, kindly developed by Volker Winkelmann from the Regional Computer Center of the University of Cologne (ZAIK/RRZK) in a collaboration on the visualization of galaxy simulations.

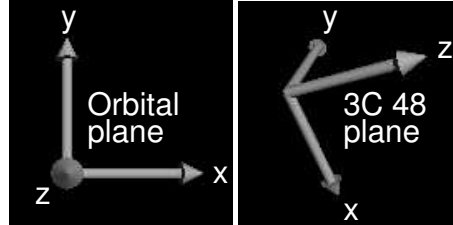


Figure 32: Sketch of projection angles. The left panel shows the view onto the orbital plane, defined as the non-rotated frame. The right panel shows the 3C 48 projection plane, obtained by tilting the orbital plane southwards by 120° , westwards by 160° , and counterclockwise by 116° . (Graphics by means of POV-ray (see <http://www.povray.org/>.)

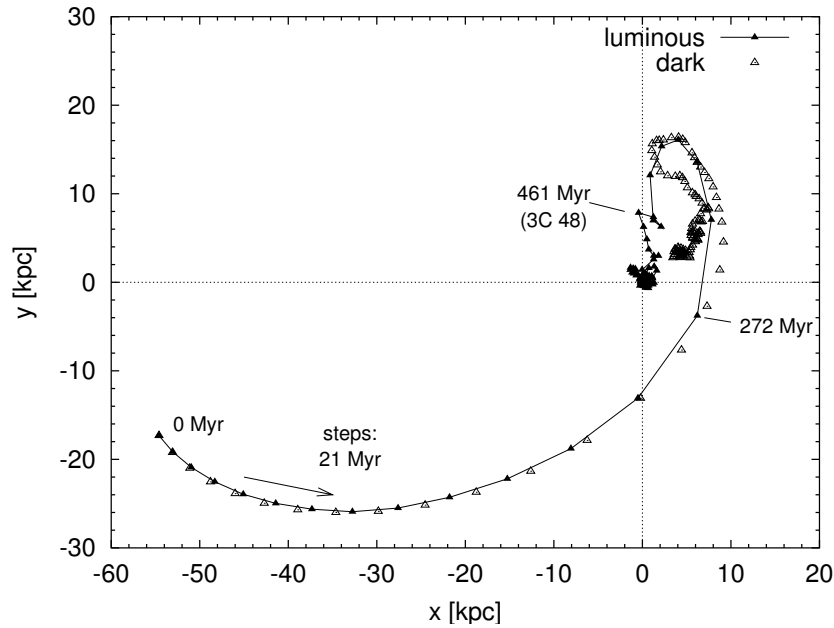


Figure 33: Comparison of the different decaying orbits traced via the centers-of-mass of the disk and bulge components (filled triangles and line), which comprise the luminous particles, and traced by the centers-of-mass of the halo components (open triangles), which comprise the dark particles. The orbits are presented in the reduced one-body system by plotting the distance vector between the centers-of-mass of each galaxy. The data points are shown at fixed time intervals of 21 Myr. Some data points of the orbit traced via the luminous center-of-mass are labeled in absolute time with respect to the start of the simulation. The time step of the 3C 48 model is indicated.

Table 13: The basic morphology of the 3C 48 host compared to the proportions of the 3C 48 model. The observational data are based on the R' -band ($0.612 \mu\text{m}$) contour plot presented by Canalizo & Stockton (2000) which is reproduced in Fig. 29 together with a sketch of the used figures of merit. The last column lists the deviations of the model ratios as percentages of the observed ratios, where "+" and "-" indicate the trend of the deviation.

Ratios	Observation	Model	Deviation [%]
$L1/L2$	0.76	0.70	-8.6
$L1/W1$	1.25	1.44	+15.2
$L1/W2$	1.67	1.86	+11.4
$L1/D$	0.52	0.55	+5.8
$L2/W1$	1.65	2.06	+24.8
$L2/W2$	2.20	2.64	+20.0
$L2/D$	0.69	0.79	+14.5
$W1/W2$	1.33	1.29	-3.0
$W1/D$	0.42	0.38	-9.5
$W2/D$	0.31	0.30	-3.2

The 3C 48 model, discussed here, emerges at a time of 461 Myr after the start of the simulation. At this stage of the merger process, the global morphology and kinematics of the luminous component is still unrelaxed.

8.1.2 The Location of the Second Tidal Tail

The 3C 48 model provides a completely new possibility for the location of the apparently missing counter tidal tail. As obvious from the rotation sequence shown in the lower row of Fig. 31, the 3C 48 look-alike emerges for a projection angle which locates the second tidal tail in front of the main body of the host galaxy. At such a location, the tidal tail is severely foreshortened and would probably be outshone in observations by the QSO nucleus and the bright host. The last two images in the lower row of Fig. 31 demonstrate that the tips of both tidal tails are screened by increasing the lowest visible density level. In observations, this corresponds to a decreased limiting magnitude (see Sect. 3.1).

Given the uniform luminosity weighting of the particles, the elongation to the south-west remains as a high-density region. It is caused by particle crowding, where the counter tidal tail bends to the front of the projection plane. The south-western elongation of the model is a mismatch regarding the near-infrared image of 3C 48 in Fig. 31 or the R' -band ($0.612 \mu\text{m}$) image from Canalizo & Stockton (2000). This mismatch becomes evident from the scale-free comparison presented in Table 13 which is based on the figures of merit introduced in Sect. 7.1.4 and Fig. 29. The strongest deviations between the observed and the model parameters of up to 25% occur for those ratios including $L2$ which measures the southern elongation of the host galaxy. The ratios including $L1$ still show deviations larger than 10%, since also the northern elongation of the model galaxy is emphasized by the brightness ascribed to the counter tidal tail. The remaining figures of merit differ by less than 10%.

Canalizo & Stockton (2000) also present a ground-based image obtained by using an U' -band filter at $0.341 \mu\text{m}$. This image displays an enhanced brightness to the south-west

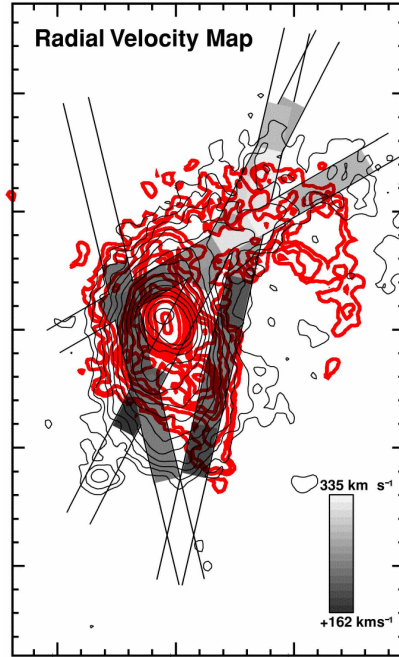


Figure 34: Direct overlay of the 3C 48 model (red) on the R' -band image of the 3C 48 host reproduced from the middle panel of Fig. 1 in Canalizo & Stockton (2000). The model is centered so that the northern of the two merging galaxy centers coincides with the highest contour in the R' -band image. As described in Canalizo & Stockton (2000), the minor and major tickmarks of the R' -band image correspond to $1''$ and $5''$, respectively.

of the 3C 48 QSO. It motivated Canalizo & Stockton (2000) to speculate about a possible gull-wing like configuration of the tidal tails. In view of the new 3C 48 model the enhanced brightness could also be a manifestation of the brightening effects where the counter tidal tail suggested by the model arcs towards the front. In this case, the mismatch of the model with the near-infrared images could just be an effect of luminosity weighting.

A direct overlay of the model and the R' -band image is shown in Fig. 34. This overlay fixes the scaling of the model units. The overlay shows that the curvature of the north-western tidal tail in the model increasingly deviates from the observed curvature towards the tip. The discrepancy is not solved by a simple rotation in the projection plane. Since the curvatures match at small angles, such a rotation causes a new mismatch where the northern tidal tail leaves the host body. The two possibilities for solving such a discrepancy have already been pointed out in Sect. 7.1.2. First, the extension of the tidal tails depends on the strengths and profiles of the dark matter halos of the model galaxies. Second, the discrepancy could be inherent to the initial orbital configuration and, in particular, to the orientation of the galaxy disks, as the projected curvature of the northern tidal tail strongly depends on the three-dimensional structure and extension of the tail. It is likely that a fine-tuning of the model would require a mixture of both possibilities.

8.1.3 Kinematical Comparison

The basic kinematic trends displayed by the mean particle line-of-sight velocities in the 3C 48 model are consistent with those in the mean stellar line-of-sight velocities reported by

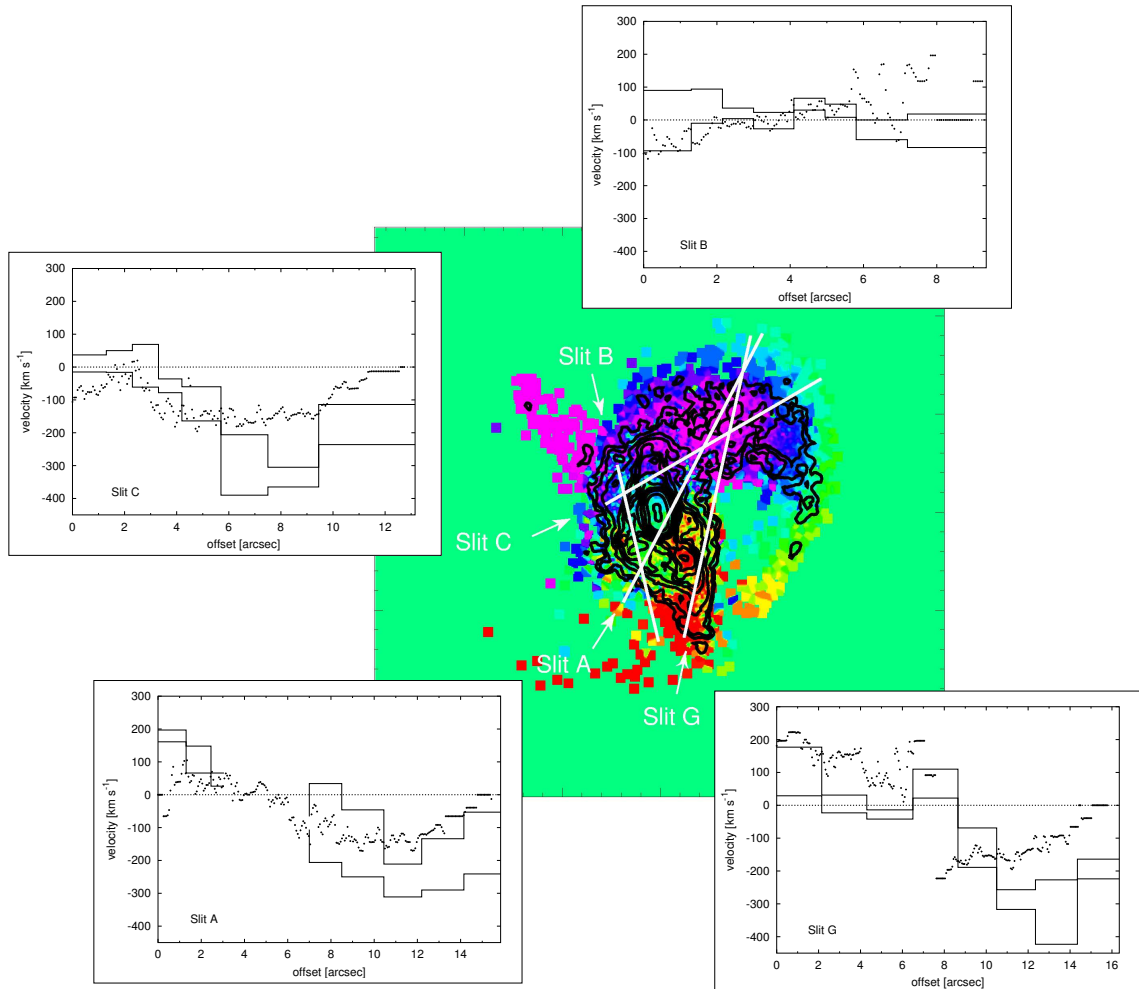


Figure 35: Slit settings used by Canalizo & Stockton (2000) for a stellar-kinematical analysis overlaid on the 3C 48 model. The model is colored according to the mean particle line-of-sight velocities. Green means a velocity of zero. The color changes via blue to magenta for higher approaching velocities and via orange to red for higher receding velocities. The major tickmarks of the coordinate box around the model image indicate $5''$. For each slit, the corresponding diagram shows a comparison of the mean stellar line-of-sight velocities within the error limits reported by Canalizo & Stockton (2000, Table 2) (region between the histograms) with the mean particle line-of-sight velocities derived from the 3C 48 model (points). The offsets along the slits are measured as indicated by the arrows.

Canalizo & Stockton (2000). As evident from the colored velocity field of the model image in Fig. 35, the highest approaching velocities (magenta) are found in the north-western tidal tail. The highest receding velocities occur in the south-western elongation, where the particles composing the tail move into the projection plane. The velocity field within the body of the host galaxy is mainly characterized by a dispersion around a line-of-sight velocity of zero.

The qualitative agreement of particle line-of-sight velocities with the observed stellar line-of-sight velocities in the 3C 48 host is demonstrated by the diagrams in Fig. 35. Each diagram shows a projection along the respective slit in the direction indicated by the arrow. The observational data, taken from Table 2 in Canalizo & Stockton (2000), are shown in histogram style. The region between the histograms corresponds to the errors reported for these measurements. The mean particle line-of-sight velocities are plotted as points. The data characterized by a constant velocity for several neighboring offset bins are an artefact of low particle statistics in these regions and should be excluded from the comparison. They are caused by the smoothing process which smears the line-of-sight velocity belonging to a single pixel in an otherwise empty region over several neighboring pixels. The low particle statistics mainly affects all slits at their large-offset ends, and *Slit G* at an intermediate offset of about $8''$. With regard to the basic trends in observed stellar line-of-sight velocities, *Slits A, C, and G* fall in a category characterized by a velocity gradient across the slit. These are the slits approximately tracing from eastern and south-eastern regions of the host towards north-western regions. *Slit B* differs by showing an almost constant velocity, close to zero for all offsets. This suggests that the major rotation axis is approximately parallel to *Slit B*. The same behavior is reflected by the mean particle line-of-sight velocities in the 3C 48 model.

8.1.4 The Nature of 3C 48A

The 3C 48 model presents a scenario in which the QSO of 3C 48 and the second luminosity peak 3C 48A are respectively associated with the merging centers of the two progenitor galaxies. This can be seen from the close-up on the central region of the 3C 48 model shown in Fig. 36. At the time step and the projection angle selected for the 3C 48 model, the two merging galaxy centers are still separated. The projected relative position and alignment of the two galaxy centers is similar to the observed separation between the QSO and 3C 48A.

However, the dynamics of the two merging galaxy centers in the simulation is very rapid at the stage of the 3C 48 model. It is impossible to fix their positions with respect to the slow evolution of the overall model morphology. Consequently, the similarity with the 3C 48 QSO and 3C 48A is rather occasional. This means that the alternative scenario of a jet-gas-interaction is possible but not necessary to explain the luminosity peak associated with 3C 48A.

8.2 The Gas Model for 3C 48

To neglect the gas contribution to the gravitational potential means a violation of Newton's third law for the interaction between the gas and the collisionless particles. The gas is accelerated by the gravitational potential of the collisionless particles but not vice versa. Despite the restriction to a less massive gas component, the gas simulation is affected by a small loss of energy. The consequence of this inaccuracy for the simulation is investigated

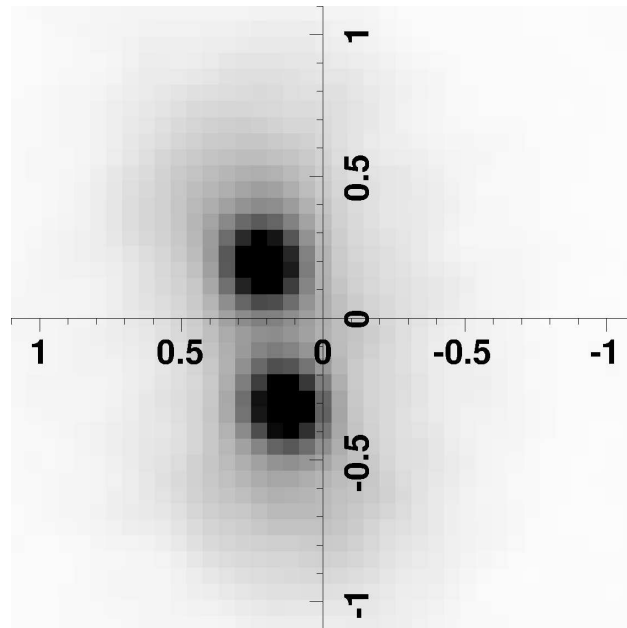


Figure 36: *Close-up on the central region of the 3C 48 model showing the separation between the two merging galaxy centers. The coordinates are given in arcseconds.*

by a comparison with the collisionless simulation. Finally, the gas model is interpreted with respect to observations of molecular gas in 3C 48.

8.2.1 Reliability of the Gas Model

The unphysical loss of energy, involved in violating Newton's third law for the gas-star-interaction, means an effective deepening of the gravitational potential. Consequently, the 3C 48 model resulting from the gas simulation suffers from an artificially enhanced compactness in comparison to the collisionless model. This effect reveals itself in Fig. 37 by a more compact host body and less-dense tidal tails in the global morphology (upper panels) and by a smaller separation of the central density peaks (lower panels). Within each row, the grey-scaling of the images is identical so that the densities are directly comparable. By means of the smaller peak separation in the central region, it has been cross-checked that the enhanced compactness is intrinsic and not caused by projection.

Fig. 38 shows that the collisionless particle distribution of the bulge and disk component are more strongly affected by the energy loss than the extended particle distribution of the halo. The decaying orbits of the simulations with and without gas, traced by the centers-of-mass of the collisionless disk and bulge particles, are compared in the left panel, the corresponding orbits, traced by the centers-of-mass of the dark halo particles, are compared in the right panel. While the halo centers-of-mass follow nearly identical orbits in both simulations, the bulge and disk centers-of-mass display deviations. This difference is a likely consequence of two points: First, the distribution of the gas particles within the galaxies disks implies a stronger interaction with the collisionless bulge and disk particles. Second, the dynamical time scales for the bulge and disk particles are much shorter than those for the halo particles.

The deepening of the potential in this gas model is a mere consequence of violating

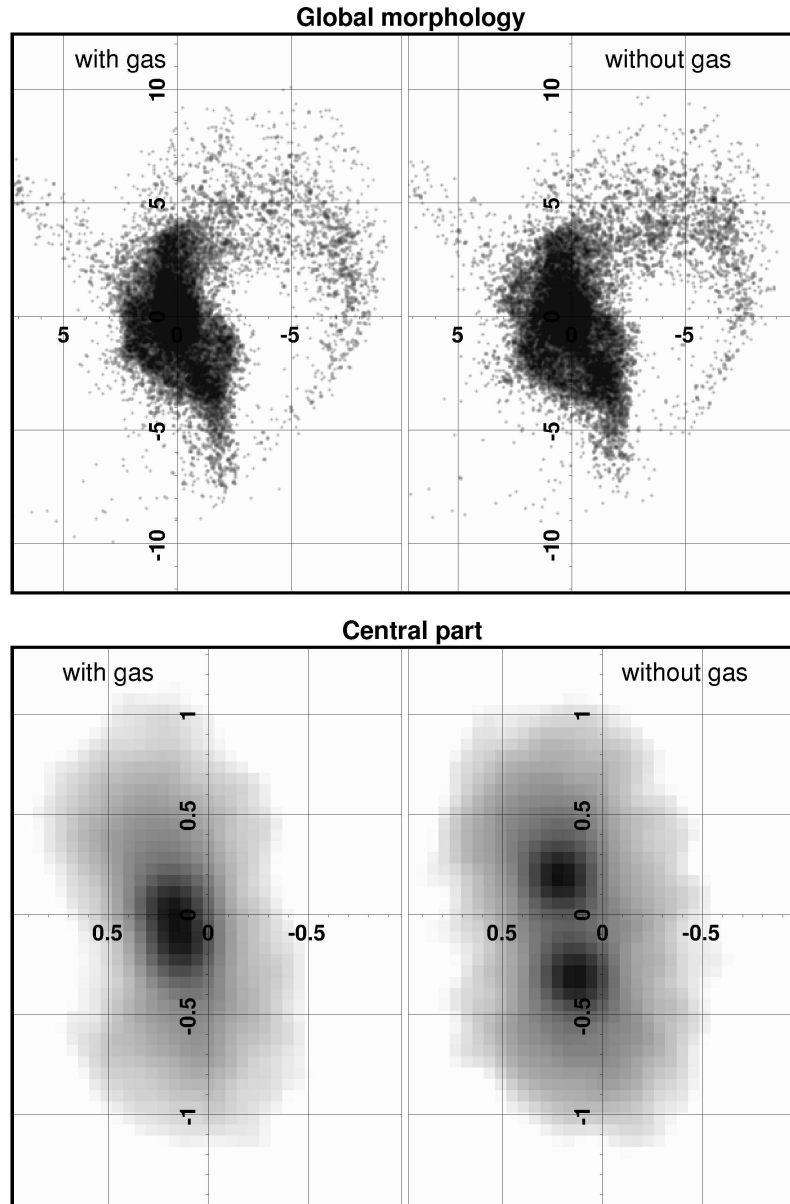


Figure 37: Comparison of the images of the 3C 48 model resulting from the simulation with and without gas. Both images show the collisionless luminous particles of the bulge and the disk only. The projection angle and the time step is the one obtained for the 3C 48 model from the collisionless simulation. The upper row shows the global morphology, the lower row a close-up of the central region. The same color bars are used for the respective images within each row so that the grey-scaling of the densities is directly comparable.

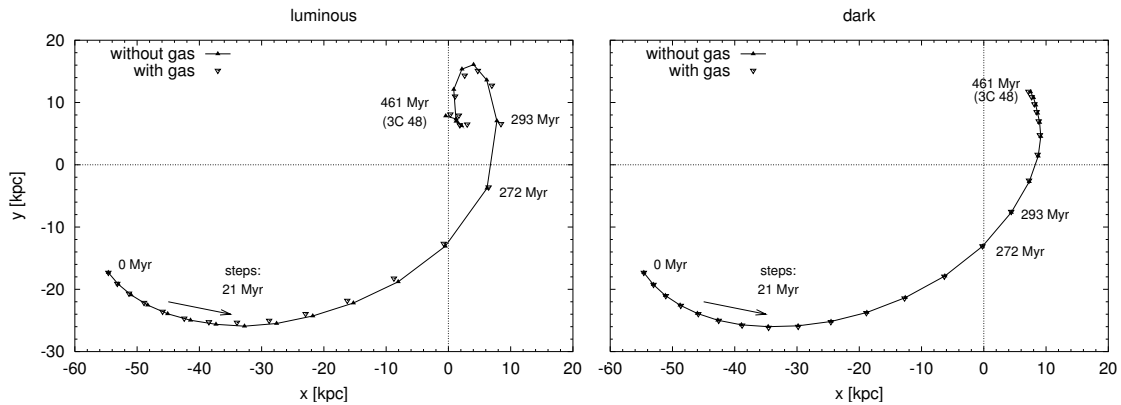


Figure 38: Comparison of the decaying orbits in the simulations with gas and without gas. The orbits are shown in the reduced one-body system. The distance vectors in the left panel are computed with respect to centers-of-mass of the luminous particles of the disk and bulge components of both galaxies. The distance vectors in the right panel refer to the centers-of-mass of the dark halo particles.

physical principles. A deepening of the potential with physical origin is found in merger simulations including a fully self-gravitating gas component (Barnes & Hernquist 1996). In this case, the deepening is caused by the central gas accumulation which forms during the merger process. While the deepening can alter the kinematics of the collisionless component in the ultimate elliptical merger remnant, the large scale dynamics of tail formation and orbital decay seems to remain basically unchanged when including a self-gravitating gas component (Barnes & Hernquist 1996). Regarding this, the separation of the merging galaxy centers in the collisionless model for 3C 48 (Sect. 8.1.4) might also be changed under the influence of a self-gravitating gas component. Without gas gravity, the model presented here is neither suitable to investigate possible consequences for the putative second galaxy center 3C 48A nor to predict the local gravitational collapse of dense gas clumps.

However, by restricting the model to a small gas mass, it suffices to study the pure kinematical response of the gas.

8.2.2 Evolution of the Gas Simulation

The evolution of the gas component during the merger simulation for 3C 48 is visualized in Fig. 39. The projection angle chosen for this figure provides a clear view onto the complex three-dimensional gas structures formed during the merger process. The evolution for the projection angle of the 3C 48 model is correspondingly shown in Fig. 40. As known from previous simulations (e.g. Barnes & Hernquist 1996; Mihos & Hernquist 1996), a major gas fraction loses angular momentum by the torques of the stars during the simulations and flows into the central regions of the merging galaxies. Correspondingly, about 50% of the gas particles of the 3C 48 simulation are found in a central sphere with a radius of about $0''.43$ at the time step of the 3C 48 model (461 Myr, last panels in Figs 39 and Fig. 40.) This number count does not consider whether the gas particles are, indeed, gravitationally bound to the central region. However, regarding the uncertainties implied in neglecting gas gravity, it can be taken as a rough estimate.

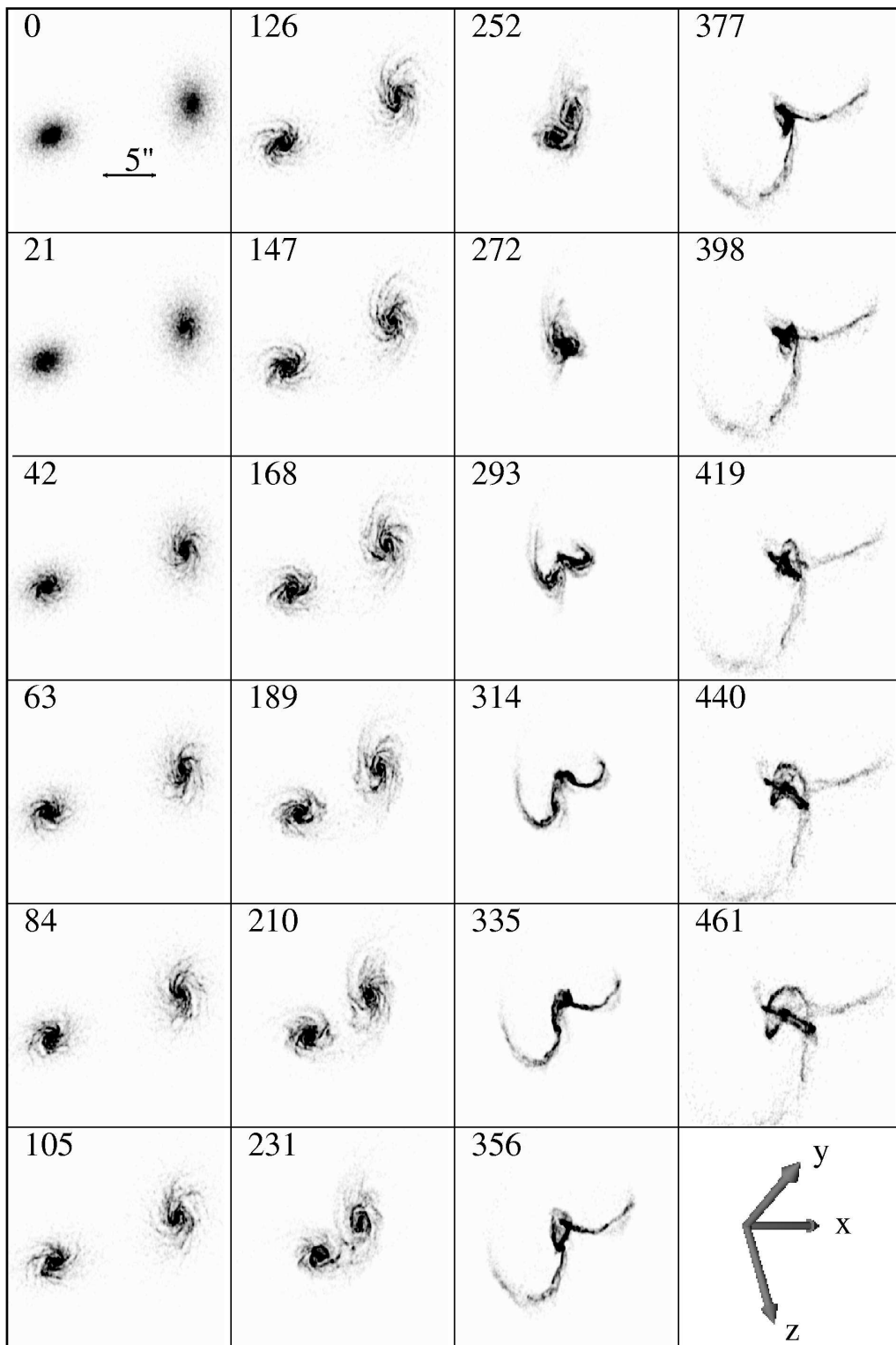


Figure 39: Time evolution of the gas density during the merger simulation for 3C 48. The projection angle is indicated in the lower right panel, the time is given in Myr. All images have the distance scaling marked by the scale bar in the first image.

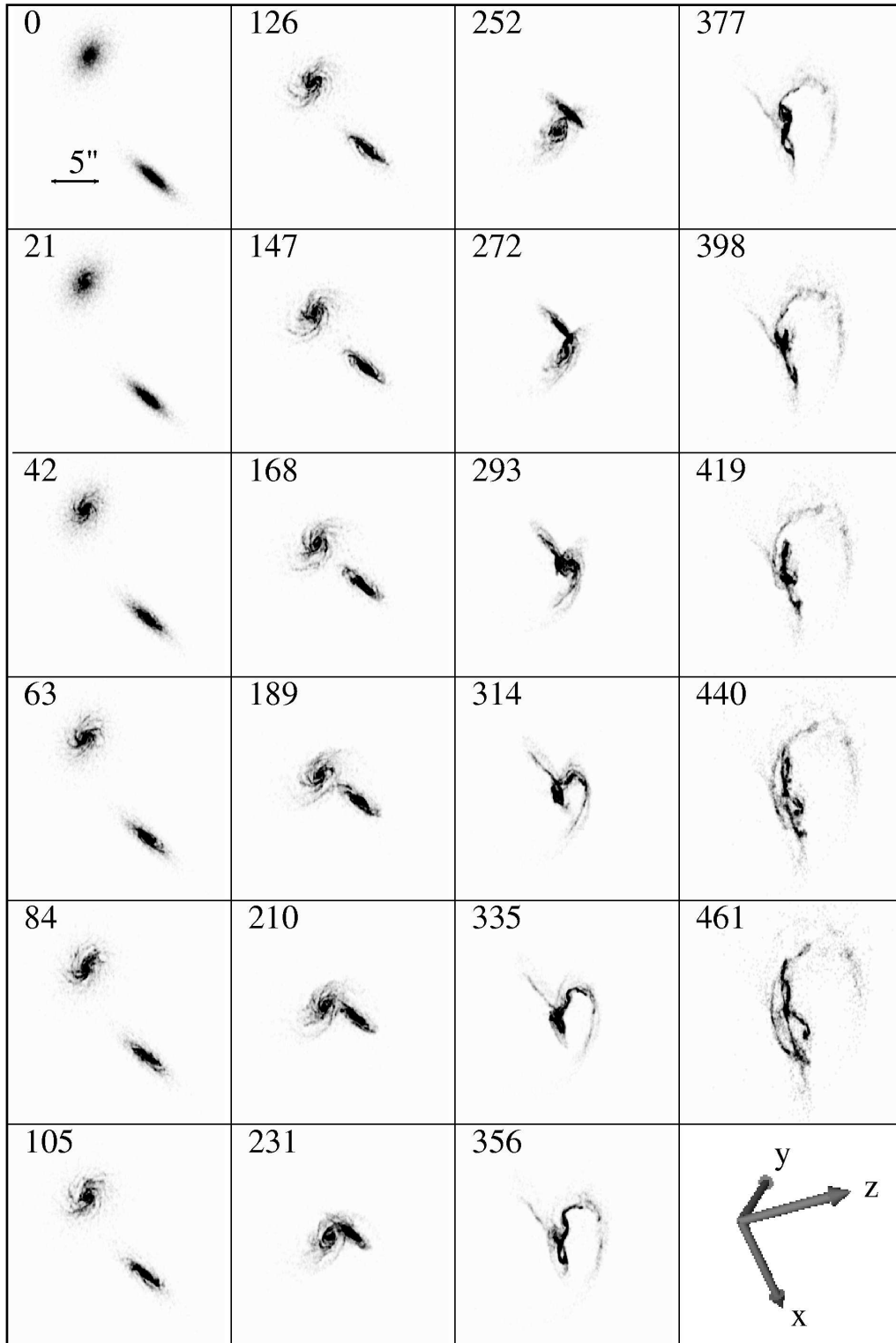


Figure 40: The same as Fig. 39, but for the projection of the 3C 48 model. The time is indicated in Myr. All images have the distance scaling as indicated by the scale bar in the first image.

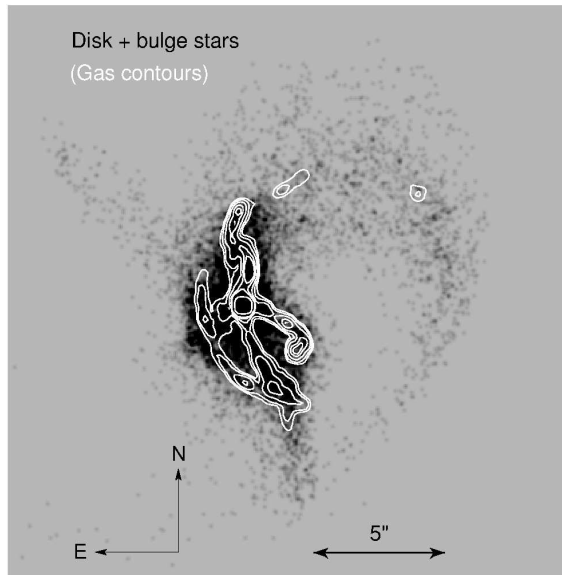


Figure 41: *Overlay of the gas density contours of the final 3C 48 model on a greyscale image of the densities displayed by the luminous collisionless particles of the bulge and the disk component.*

The basic evolution of the gas model is similarly consistent with previous merger models between two inclined disk galaxies (e.g. Barnes & Hernquist 1996). In contrast to the collisionless dynamics of the stellar particles, the gas component dissipates energy by forming shocks. This also implies that the gas is not able to move on intersecting orbits. Consequently, the structures traced by the gas are more clearly marked than the corresponding stellar ones.

In the initial stages of the merger, the gas in both galaxy disks develops a spiral structure. The same is observed in the models discussed by Barnes & Hernquist (1996), who include gas self-gravity and radiative heating and cooling in their simulations. These authors report to find such a spiral structure also in isolated galaxy models. As they discuss, the effect is mainly attributed to swing amplification (see Sect. 5.6.5) of noise, inherent to the discrete particle distribution. This noise is a consequence of the fact that multi-particle simulations for galaxies are based on a Monte Carlo technique (Sect. 6.2).

The main influence on the gas particles is exerted by the bar-like potential perturbation formed in the galaxy disks as a consequence of the tidal forces of the interaction. Such a barred potential is known to force the gas particles into an eccentric ring (e.g. Shlosman & Heller 1994; Barnes & Hernquist 1996). The spatial structure of the gas features is complex since the potentials within the inclined disk components are superposed with the tidal forces predominantly oriented in the orbital plane. This results in a complex three-dimensional structure of warped gas rings, when the galaxies finally approach the second time after their apocenter passage at about 335 Myr.

8.2.3 The Gas Distribution in the 3C 48 Model

The regions of the highest gas concentrations in the 3C 48 model can be seen from Fig. 41. This figure shows an overlay of the gas density contours of the 3C 48 model on a greyscale image of the densities displayed by the collisionless bulge and disk particles. The gas model

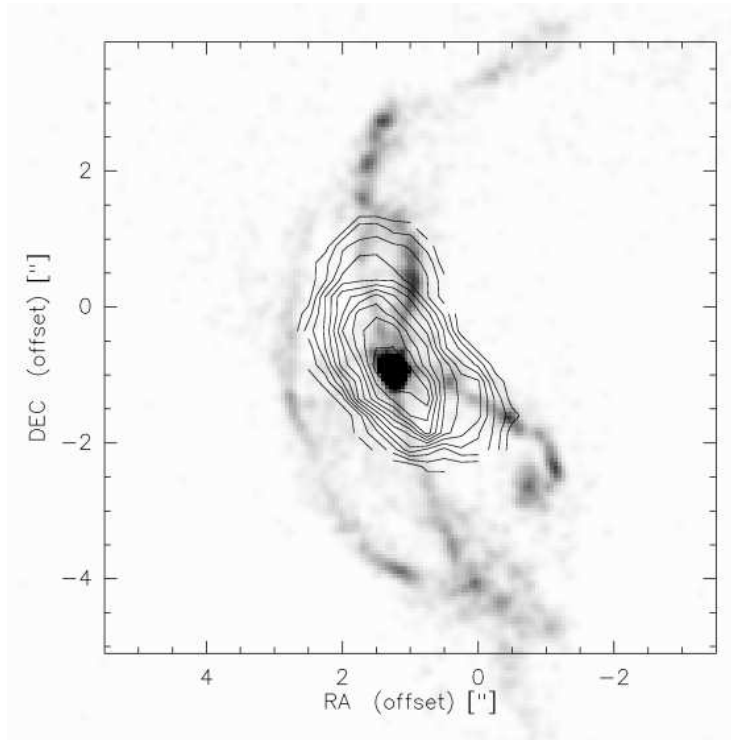


Figure 42: *Overlay of the integrated $^{12}\text{CO}(1-0)$ intensity measured for 3C 48 (contours) on the gas density distribution displayed by the 3C 48 model (greyscale image). The CO data are provided by courtesy of Melanie Krips (Krips et al., *subm. to A&A*).*

features two striking coincidences with the observed properties of molecular gas in 3C 48.

- (i) The model is characterized by the high central gas concentration which contains about 50% of all gas particles. This agrees with observations in which molecular gas is only detected close to the center of 3C 48 (Scoville et al. 1993; Wink et al. 1997). Conclusions about starbursts and the formation of local gas clumps by gravitational collapse are beyond the scope of a model without gas gravity. However, the mere presence of gas inflows in the model suggests a considerable star formation activity in reality. This is in agreement with the enhanced star formation activity in the 3C 48 host derived from observations (Canalizo & Stockton 2000).
- (ii) The gas distribution in the model is compared with contours of the integrated $^{12}\text{CO}(1-0)$ intensity in Fig. 42. The CO data for this overlay were provided by courtesy of Melanie Krips. As a consequence of the complex three-dimensional systems of gas rings, the model projection is characterized by a structure of gas lanes. The most prominent lanes are the ones to the north and to the south-west of the central gas concentrations. These lanes coincide with the elongated morphology of the molecular gas distribution in 3C 48, displayed by the latest observations of $^{12}\text{CO}(1-0)$, (Krips et al., *subm. to A&A*).

8.3 The 3C 48 Model as Observational Stimulus

The multi-particle model for 3C 48 yields direct stimulus for future observation programs. This applies to the collisionless model as well as to the tentative results derived from the gas model.

The collisionless model inspires a new idea of a possible location of the apparently missing counter tidal tail. The search for such a tidal tail could be a particular challenge for imaging at high sensitivities. In front of the host galaxy, the detection will be difficult in consequence of the bright background emission from the QSO and the main body of the host galaxy. According to the model, these observations should, therefore, concentrate on those regions where the counter tidal tail exceeds the body of the host galaxy. This qualifies either the region to the north-east of the 3C 48 body or the one to the south-west. Unlike the north-eastern part, the south-western part of the tidal tail model is strengthened by crowding effects, where the tail arcs to the front. The simulation, therefore, predicts the easiest detection in the region south-west to the 3C 48 host. Besides imaging, the model motivates spectroscopy programs to search for the kinematic signatures of the counter tidal tail. Again, the most promising region is the one to the south-west of the host galaxy. This part is predicted to show a peak of receding velocities. The exact position of this peak is an uncertainty of the model parameters and might be missed by incomplete spatial sampling, if using long-slit spectroscopy. The project, therefore, suggests itself as an interesting program for integral field spectroscopy.

The tentative gas model discussed for 3C 48 shows the striking coincidence of the northern and the south-western high-density lanes with the corresponding elongation found in most recent observations of $^{12}\text{CO} (1-0)$ in 3C 48. Improved observations might provide a more detailed observational approach to the filamentary gas structure predicted by the model. Besides the gas lanes, the model predicts several regions with gas density peaks. Since gas gravity is neglected, it is not possible to directly associate these peaks with star forming regions caused by gravitational collapse. Even though unsuitable for an observational comparison with peaks of star formation activity across the 3C 48 host, the peaks should be expected to coincide with regions of enhanced molecular gas densities in the 3C 48 host.

Part IV

Conclusions

9 Summary of the Individual Case Studies

This work presents case studies of the two QSO hosts I Zw 1 and 3C 48, both originally used by Sanders et al. (1988) as neighboring template objects at a transitional stage in the proposed evolutionary track from ULIRGs to QSOs. The results about I Zw 1 are based on data obtained from NIR imaging and spectroscopy with the ISAAC camera at the Very Large Telescope. The investigations of 3C 48 are based on numerical multi-particle simulations combined in an interpretative way with previously published data. The following two sections present brief summaries of the main results obtained from the analyses discussed in detail in the respective sections of Parts II and III.

9.1 I Zw 1 and the Two Nearby Sources

The study of I Zw 1 focused on the I Zw 1 QSO, the host galaxy, as well as the two bright sources to the north and to the west.

As discussed in Sect. 5.1, the *J*-band image provides evidence for an ongoing minor merger process between the I Zw 1 host and the western source. The bridge found between this source and the north-western spiral arm of the I Zw 1 disk, the extension at the far side of the western source, and its elongation along a roughly radial axis with respect to the I Zw 1 disk, remind of the bisymmetric forces occurring during a tidal interaction. In agreement with previous optical spectroscopy (Canalizo & Stockton 2001) and with the results obtained from the *JHK* colors (Sect. 5.5.2), the *H*- and *K*-band spectra of the likely companion indicate an old stellar population (Sect. 5.4). This suggests that the companion shows similarities to an elliptical dwarf galaxy. The spectra provide evidence that the second bright source to the north of I Zw 1 is a projected foreground star (Sect. 5.3). This supports the previously assumed scenario (Sargent 1970; Stockton 1982) and argues against the recently proposed idea that the object might be a tidal dwarf galaxy or a galaxy nucleus merging with I Zw 1 (Davies et al. 2003). It seems to be merely by coincidence that the star is apparently located near the tip of the north-western spiral arm of I Zw 1.

Based on the one-dimensional decomposition of the *J*-band surface-brightness profile and the gas rotation curve (Sect. 5.6), the I Zw 1 host galaxy itself shows characteristics typical of a high-surface-brightness spiral galaxy. The *J*-band mass-to-light ratio of the bulge component is unusually low, which indicates a mean young stellar population with an enhanced fraction of hot stars and supergiants. Although allowing no unique conclusion, the same trend towards younger stellar populations in the central region of the host galaxy is suggested by the *JHK* color-color diagram (Sect. 5.5.1). Consistently, central starburst activity in I Zw 1 is suggested in view of previous results from spectroscopy and in view of the circum-nuclear gas ring found in molecular gas observations (Schinnerer et al. 1998; Staguhn et al. 2004).

The nuclear spectrum of the I Zw 1 QSO (Sect. 5.2) mainly confirms the results from a previous spectrum (Schinnerer et al. 1998). The hydrogen emission lines indicate broad and narrow components and their ratios are comparable to the values expected for case *B* recombination under standard conditions. As previously discussed, the high-excitation

lines are extremely blueshifted. Likely originating from the coronal line region located at distances between the narrow- and the broad-line region, these lines suggest significant outflowing velocities.

In summary, the new NIR data consistently complement the existing knowledge about I Zw 1 and provide further evidence for an ongoing minor merger process with the western companion galaxy.

9.2 3C 48

As a central result, the multi-particle model for 3C 48 shows no a priori contradiction to the hypothesis that 3C 48 has emerged from a major merger between two galaxies of similar masses. Starting from the heuristic assumption of two equal disk galaxies interacting in an inclined orbital configuration, a model of 3C 48 emerges under a certain projection angle, 461 Myr after the initialization (Sect. 8.1). This model is in qualitative agreement with the basic morphology and the stellar line-of-sight velocity field of the 3C 48 host (Sect. 8.1.3 and Canalizo & Stockton (2000)). At the selected time step, the galaxy centers are in the final stages of merging but are still separated. It is, therefore, possible that the QSO of 3C 48 and the second luminosity peak 3C 48A, found about $1''$ north-east of the QSO (Stockton & Ridgway 1991), represent the merging centers of the two 3C 48 progenitor galaxies (Sect. 8.1.4). A stringent conclusion from the model is inhibited by the fact that the dynamics of the merging galaxy centers is much more rapid than the evolution of the overall morphology. The alternative scenario of 3C 48A as being the hot spot of an interaction of the radio jet with the interstellar medium (e.g. Stockton & Ridgway 1991; Chatzichristou et al. 1999) is still possible but not necessary.

As discussed in Sect. 8.1.2, the model provides a new solution for the controversy about the apparently missing counter tidal tail in 3C 48. In the model this tidal tail is located in front of the 3C 48 host galaxy for the projection angle of the model. At such a location, the tidal tail is likely to be missed in observations so far. It is, therefore, up to more sensitive imaging observations in the future to test the model predictions. As a consequence of crowding effects, the model suggests the region south-west to the 3C 48 QSO as the one most promising for a possible identification of the counter tidal tail (Sect. 8.3).

The simulation including in addition a non-gravitating gas component (Sect. 8.2.3) results in interesting similarities to recent molecular gas observations of 3C 48 (Krips et al., *subm. to A&A*). It indicates that the large central gas masses could be the consequence of gas inflows triggered by the tidal interaction. The elongated structure of the observed molecular gas distribution coincides with high density gas lanes in the model.

In summary, the simulations of this work show that the 3C 48 host galaxy can be described as a major merger remnant.

10 The Merger Properties of I Zw 1 and 3C 48

Depending on the mass ratios of the galaxies involved in a merger process, the resulting remnants display very distinct morphological and kinematical signatures.

A typical minor merger is given by an initial mass ratio of larger than 10:1 between the spiral galaxy and its merging dwarf companion. In such a kind of merger, the spiral galaxy is mainly changed in the vertical direction by disk heating and thickening (Walker et al. 1996). The radial profile remains a disk governed by rotational velocity. The ultimate

major merger is defined by a mass ratio of 1:1 between the two interacting spiral galaxies. This type of merger is known to transform the progenitor galaxies into an elliptical galaxy supported by velocity dispersion rather than rotation (e.g. Barnes 1992). Between these two extrema, there seems to be a gradual change in the properties of the merger remnant from predominantly disk-like characteristics to predominantly elliptical-like ones (Bendo & Barnes 2000; Cretton et al. 2001; Naab & Burkert 2003; Bournaud et al. 2004a).

Both, I Zw 1 and 3C 48, fit well into this clear scheme of initial galaxy mass ratios and resulting remnant structures. As already discussed in Scharwächter (2001), the mass ratio between I Zw 1 and the companion galaxy seems to be larger than 10:1. It classifies this system as the typical minor merger of a spiral galaxy with a low-mass companion. Correspondingly, I Zw 1 still shows a spiral morphology as well as the typical kinematic signatures of a rotating disk. The simulations for 3C 48, in contrast, suggest a major merger. This agrees with the fact that the body of the 3C 48 host is already more reminiscent of an elliptical galaxy.

The conclusions about the correlations between remnant structure and initial mass ratio refer to merger remnants when they have completely coalesced into a single galaxy. Both, I Zw 1 and 3C 48, are not at the final relaxed stages of their putative merger processes, so that it is not surprising that the typical characteristics are not yet fully developed. The timing of merger processes is difficult because of the many unknown parameters. The supposed minor merger in the case of I Zw 1 will be ongoing, since the companion is still distant from the I Zw 1 center. In the case of major mergers, the classical Toomre sequence represents an attempt to classify different merger stages based on observations. This sequence can be used for an approximate timing of the supposed major merger responsible for the present appearance of the 3C 48 host.

10.1 3C 48 and the Toomre Sequence

The Toomre sequence (Toomre 1977) consists of eleven galaxies or galaxy systems from the NGC catalog. The overview given here is based on the information given in two recent publications about the Toomre sequence (Hibbard & van Gorkom 1996; Laine et al. 2003).

Since the presence of extended tidal tails was the main criterion for selection, it is most likely that all systems represent ongoing major mergers between two spiral galaxies in a prograde encounter geometry. They are ordered into a sequence of decreasing distance between the galaxy bodies or increasing degree of coalescence. With regard to the scenarii revealed by the typical simulations for mergers of two disk galaxies, the Toomre sequence is likely to be an evolutionary sequence. Hubble Space Telescope images of all eleven objects of the merger sequence are presented by Laine et al. (2003) in the original ordering. These consist of NCC 4038/4039 (*the Antennae*), NGC 4676, NGC 7592, NGC 7764A, NGC 6621/6622, NGC 3509, NGC 520, NGC 2623, NGC 3256, NGC 3921, and NGC 7252.

Hibbard & van Gorkom (1996) define three stages of the sequence. In the early stage, the two spiral galaxies are clearly separated and their disks are not completely disrupted. In the intermediate stage, the two galaxies form a common body but still with distinct nuclei. In the late stage, the galaxies have relaxed into a single object with tidal features in the outskirts.

Compared to the Toomre sequence, 3C 48 is suggested to be a representative of the late stage. Depending on the nature of 3C 48A two scenarios are possible:

- (a) 3C 48A is not associated with a second galaxy center but is resulting from a jet-

gas-interaction. In this case, the 3C 48 merger would be characterized by a single nucleus and, therefore, belong to a late stage of the original Toomre ordering. This, of course, does not take into account projection effects. A second galaxy center could still be present, hidden by the host body.

- (b) 3C 48A is the center of the second precursor galaxy – a scenario which is at least not impossible regarding the multi-particle model. In this case, the projected separation between both galaxy centers is about 4.1 kpc (Stockton & Ridgway 1991). At this small separation 3C 48 would already belong to the class of late stage mergers (e.g. Table 1 in Laine et al. 2003).

The late-stage merger scenario is also suggested by the large-scale morphology of the 3C 48 host galaxy. Very similar to the late-stage Toomre objects NGC 2623, NGC 3256, NGC 3921, or NGC 7252, the host appears as a single body in a rather relaxed stellar envelope, but with a significant tidal extension at least to the north-west.

10.2 Possible Scenarios for 3C 48 and I Zw 1

The scenario of a late-stage major merger for 3C 48 is consistent with the unusually large amounts of molecular gas of a few times $10^{10}M_{\odot}$ found in the center (Wink et al. 1997), assuming that both precursor galaxies were gas-rich. The large dynamical masses involved in a major merger imply strong tidal forces, driving the cumulative gas reservoir toward the center of the remnant galaxy (Mihos & Hernquist 1996). This gas inflow is supported by the tentative gas simulations discussed for 3C 48. Without regard to the detailed fueling mechanisms which determine the final fueling efficiency in the nuclear region of 3C 48, starbursts and AGN activity are likely to be more vigorous, the larger the total reservoir of gas is. Consistently, 3C 48 is a powerful representative of the objects at a transitional stage between ULIRGs and QSOs with a large infrared luminosity of $L_{\text{IR}} = 10^{12.81}L_{\odot}$ as well as a large blue magnitude $M_{\text{B}} = -24.55$ (Canalizo & Stockton 2001).

As a consequence of the minor merger with the low-mass elliptical dwarf, I Zw 1 is only supplied with its own original gas reservoir. Consistent with this reasoning, the mass of molecular gas of $M_{\text{H}_2} = 9 \times 10^9 M_{\odot}$ (Schinnerer et al. 1998) is typical to the masses found in spiral galaxies. The tidal forces are weak but apparently able to cause dynamical instabilities in the I Zw 1 disk, invoking gas inflow associated with starbursts and nuclear activity. The weak tidal forces and the small gas reservoir make expect that I Zw 1 is less luminous than typical ULIRGs or QSOs. In fact, the luminosity of $L_{\text{IR}} = 10^{11.87}L_{\odot}$ and the nuclear magnitude of $M_{\text{B}} = -22.62$ (Canalizo & Stockton 2001) are just at the limits of the definitions used for the ULIRG and the QSO classes.

The ongoing minor merger in the case of I Zw 1 and the advanced major merger in the case of 3C 48 seem to be at different intrinsic stages of the dynamical merger process. Yet there is a possibility to explain their neighboring stage in the proposed evolutionary sequence from ULIRGs to QSOs. The total time elapsed since the onset of the interactions could be similar in both cases, regarding the different forces implied in a minor and a major merger. This would require the interaction between I Zw 1 and the companion to be already long-lasting. A caveat for this scenario is given by the young ages of only a few 10 Myr found for the nuclear starburst (Schinnerer et al. 1998). On the contrary, the companion displays an old stellar population, either because its starburst has already subsided or because it is an intrinsically gas-poor object without the ability for strong

star formation. These controversies can be solved by the observation that the starburst in the more massive partner of an unequal-mass merger can be delayed by up to 100 Myr compared to the starburst in the less-massive partner (Bernloehr 1993). A similar scenario for delayed starburst in such transition objects which are at a later stage of the merger is also discussed by Canalizo & Stockton (2001). They further conclude that the age of the QSO activity is correlated with the age of the starburst rather than with the dynamical age of the merger process. As shown by simulations, the starburst activity in a merger process can be delayed by the presence of a significant bulge component (Mihos & Hernquist 1996).

Nevertheless, in the case of I Zw 1 it is not certain whether the apparently ongoing minor merger is the origin of its present nuclear activity. It cannot be excluded that the QSO and the starburst activity are the consequences of a previous merger event. Regarding the spiral morphology of I Zw 1, it is, however, unlikely that any recent merger event was a major one.

11 On the Discrepancies between ULIRGs and QSO Hosts

The validity of a global ULIRG-to-QSO evolutionary track has recently been challenged by basic discrepancies found between a sample of ULIRGs (Tacconi et al. 2002) and a sample of classical radio-loud QSOs, radio-quiet QSOs, and radio galaxies (Dunlop et al. 2003, which is based on earlier samples as mentioned in the references therein). The ULIRG sample consists of 18 objects at redshifts smaller than 0.16, which were chosen because of their likely late-stage merger properties. The QSO sample includes 33 objects at redshifts smaller than 0.25 and is characterized by comparably high QSO luminosities.

The main argument against an evolutionary link comes from the observation that ULIRGs and QSO host galaxies seem to occupy different regions in the fundamental plane spanned by the effective radius, the effective surface brightness, and the stellar velocity dispersion. The ULIRGs from the sample by Tacconi et al. (2002) are comparable to intermediate-mass ellipticals with small effective radii of about 1 kpc and small velocity dispersions. In contrast, the QSO hosts of the sample presented by Dunlop et al. (2003) are similar to massive ellipticals which are characterized by effective radii of about 10 kpc and by high velocity dispersions. It has to be mentioned that the latter statement about the velocity dispersions of QSO hosts is not based on real measurements but simply on the assumption that the QSO hosts display the same velocity dispersions as the massive ellipticals which they resemble in their effective radii and surface brightnesses. Even if this assumption were valid, the apparent discrepancies could still be solved when regarding the observational bias implied in the extreme physical conditions in ULIRGs and QSOs:

- The apparent discrepancy in stellar velocity dispersions could be caused by dust extinction, as the high dust extinction in ULIRGs could imply a bias towards lower values of the measured stellar velocity dispersions. Such an effect occurs, if the central high-velocity-dispersion regions are hidden by dust. Consequently, the line widths in the spectra only trace the lower velocity dispersions of the stellar kinematics in the outer regions.
- Stellar velocity dispersions also depend on the stage of the merger. As discussed in Sect. 8.1.1 for the example of the merger orbit of the 3C 48 simulation, relaxation is most efficient in the inner parts of the merger remnant where the dynamical time

scales are small. Since the ULIRG population is primarily found at later merger stages (Mihos 1999; Veilleux et al. 2002), the central regions should already be kinematically relaxed (Mihos 1999). However, it remains unproven whether the velocity dispersions measured for the ULIRGs are indeed representative of the more relaxed merger stages which should be characteristic of QSO hosts.

- Genzel et al. (2001) and Tacconi et al. (2002) emphasize the significant influence of dust extinction, hot dust emission, and starburst properties on the measured effective radii. They show that this is reflected in the fact that the K -band effective radii of the ULIRG sample are, by a factor of about 2, larger than J -band effective radii. Tacconi et al. (2002) present a toy model in which ULIRGs can theoretically reach the effective radii of QSO hosts as a consequence of stellar evolution effects. However, they disregard this possibility in view of the extreme conditions required by this model.
- Both, the ULIRG and the QSO effective radii, could be affected by unclean subtractions of the central AGN component (e.g. Veilleux et al. 2002).

Although these observational uncertainties weaken the statement about the ULIRG-QSO discrepancies, the prime uncertainty seems to be implied in the samples chosen for the comparisons. The small sample of ULIRGs discussed by Tacconi et al. (2002) might result in an underestimation of the variations in the measured properties. This is suggested by Veilleux et al. (2002) based on their much larger sample of 118 ULIRGs at a median redshift of 0.145. While their sample proves consistent with the statement that ULIRGs do not resemble massive ellipticals, Veilleux et al. (2002) avoid a more detailed comparison in view of the wide range of properties displayed by their sample.

On the QSO side, there are obvious disagreements between the samples presented by Dunlop et al. (2003) and by McLeod & McLeod (2001). The latter contains 16 radio-quiet QSOs comprised of the most luminous Palomar-Green QSOs and several additional luminous QSOs up to $z \lesssim 0.4$. As Veilleux et al. (2002) point out, the McLeod & McLeod (2001) sample much better fits the properties of ULIRGs, as it is characterized by smaller effective radii than the Dunlop et al. (2003) sample. They also report the host galaxy luminosities and colors of their ULIRG sample to basically agree with the ones of infrared-excess QSOs (e.g. Surace et al. 2001). Like I Zw 1 and 3C 48, these QSOs are considered as transitional objects in the ULIRG-to-QSO evolutionary sequence.

The latter seems to confirm the evolutionary hypothesis at least for these objects which are likely to be at an immediate post-ULIRG stage. Whether the evolutionary track is as simple as originally proposed by Sanders et al. (1988) remains controversial. Some ULIRGs might just evolve into quiescent intermediate-mass ellipticals as suggested by Genzel et al. (2001) and Veilleux et al. (2002). Likewise, the mentioned discrepancies with the QSO sample presented by Dunlop et al. (2003) might indicate that only subsets of QSOs originate from ULIRGs.

In agreement with the previous results about I Zw 1 and 3C 48 as transitional objects with merger indications (Canalizo & Stockton 2001), the study presented here suggests that merger signs could be the clue to identify such subsets.

A List of Abbreviations

AGN	Active galactic nucleus
BALQSO	Broad-absorption line quasi-stellar object
BIMA	Berkeley Illinois Maryland Association
CSS	Compact steep-spectrum source
ESO	European Southern Observatory
FWHM	Full width at half maximum
HST	Hubble Space Telescope
IRAS	Infrared Astronomical Satellite
ISAAC	Infrared Spectrometer and Array Camera
NIR	Near-infrared
NLS1	Narrow-line Seyfert 1
PdBI	Plateau de Bure Interferometer
PSF	Point-spread function
QSO	Quasi-stellar object
SED	Spectral energy distribution
SPH	Smoothed Particle Hydrodynamics
S/N	Signal-to-noise ratio
ULIRG	Ultraluminous infrared galaxy
VLT	Very Large Telescope

B The Program SIM2OBS

The program SIM2OBS is written to transform the particle lists provided by the multi-particle program into a form mimicking real telescope observations. This is done by projecting the particles for a specified viewing angle onto a grid similar to the pixel array of detectors. The number of particles contained in each grid cell and the mean line-of-sight velocity of the particles are computed. In order to scan the velocity field in the line-of-sight direction, the program provides the option to select only those particles within a slice parallel to the line-of-sight direction. The pixel lists can be read by using the IRAF¹³ task RTEXTIMAGE to convert them into the IRAF internal IMH format which can be transformed into the standard FITS format using the task WFITS.

The viewing angle is specified by the three angles α_x , α_y , and α_z for a counterclockwise rotation around the fixed axes x , y , and z . Other parameters required by SIM2OBS include the total number of particles, the number of dark and luminous particles, a switch to select luminous particles only, the dimensions of the pixel array, the number of slices in the line-of-sight direction, and scaling factors for lengths, velocities, and luminosities.

For each slice in the line-of-sight direction, the program yields two output files of pixel arrays, both starting with a header for basic FITS informations. One file contains a list of the total number of particles within each pixel, weighted by a constant luminosity scaling factor. A second file contains a list of pixel values reporting the mean particle line-of-sight velocities. The array of the mean velocities is multiplied by the array of particle luminosities within the program. Therefore, the output velocity array has to be divided

¹³Image Reduction and Analysis Software, see <http://iraf.noao.edu/>

by the output particle luminosity array. In the case of the 3C 48 model, both arrays are individually smoothed by a Gaussian convolution using IRAF before they are divided.

In summary, the program executes the following steps:

- Read the particle data from the simulation snapshot.
- Rotate the viewing angle by the specified angles.
- For each slice in the line-of-sight direction:
 - For each pixel of the array:
 - Construct a linked lists of associated particles.
 - Sum the number of particles and multiply by luminosity factor.
 - Compute the mean line-of-sight velocity of the particles.
 - Multiply the derived velocity by the pixel luminosity.
- Write the arrays for *particle luminosity* and *mean line-of-sight velocity* \times *particle luminosity*.

C Cosmological Measures

This outline of several important cosmological definitions mainly refers to the summary of distance measures given by Hogg (1999). A detailed introduction to cosmology is given by Peacock (1999).

The Hubble constant H measures the expansion rate of the Universe. Its present-day value is indicated as H_0 . As this value is uncertain, it is often expressed as $H_0 = 100h \text{ km s}^{-1} \text{ Mpc}^{-1}$, where h is a dimensionless parameter, usually assumed as 0.5, 0.75, or 1, for simplicity. Most recent measurements indicate an h around 0.72 (e.g. Koopmans et al. 2003; Altavilla et al. 2004). The Friedmann-Lemaître cosmological models, as simple solutions for the Einstein field equations in the case of a homogeneous and isotropic Universe, are further parametrized by the dimensionless density parameters Ω_m , Ω_r , and Ω_v . These parameters account for pressure-less matter, for radiation as matter with pressure, and for vacuum energy, respectively. The parameters are related with the curvature k via the Friedmann Equation

$$\frac{kc^2}{H^2 R^2} = \Omega_m(a) + \Omega_r(a) + \Omega_v(a) - 1,$$

where R is the scale factor and $a = R/R_0$ is its normalized form (Equation (3.31) in Peacock (1999)). In the case of a flat Universe with $k = 0$, this equation has the simple form $\Omega_m(a) + \Omega_r(a) + \Omega_v(a) = 1$. As a dimensionless measure, the deceleration parameter

$$q := -\frac{\ddot{R}R}{\dot{R}^2} \tag{C.1}$$

is often used to specify the assumed cosmology. In the Friedmann-Lemaître cosmological models, it is given by $q = \Omega_m/2 + \Omega_r - \Omega_v$, which becomes $q = 3\Omega_m/2 + 2\Omega_r - 1$ if

$k = 0$. The deceleration parameter is a practical measure under the assumption of a flat and matter-dominated Universe, in which case it is simply given by $q = \Omega_m/2$. The latter cosmological model is usually used for the purposes of extragalactic research, so that the cosmology is specified by the present-day values of the Hubble constant H_0 and the deceleration parameter q_0 .

Throughout this thesis, it is assumed that $q_0 = 0.5$, which corresponds to the so-called *Einstein-de Sitter* model given by $k = 0$, $\Omega_m = 1$, and $\Omega_v = 0$. When measuring distances for high-redshift objects, it has to be distinguished between the luminosity distance D_L , defined via the relation $f = L/(4\pi D_L^2)$, and the angular-size distance D_A , at which the source of size s appears with an angular size of $\delta\Theta = \tan^{-1}(s/D_A)$. Both distances are related via

$$D_L = (1 + z)^2 D_A.$$

For the assumed cosmological models, the luminosity distance is given in terms of q_0 by

$$D_L = \frac{c}{H_0} \frac{2[2 - 2q_0(1 - z) - (2 - 2q_0)\sqrt{1 + 2q_0z}]}{4q_0^2}.$$

While still negligible for the redshift of I Zw 1, the differences become important at the redshift of 3C 48.

D Eddington Luminosity and Eddington Limit

This short outline of the physical limits implied in spherical gas accretion refers to the explanation presented in Krolik (1999).

Assuming a radiating object of mass M surrounded by fully ionized gas and assuming Thomson scattering as the main interaction process between radiation and the gas, accretion is only possible as long as the inward gravitational forces exceed the outward radiative forces. The Eddington luminosity is the maximum possible luminosity allowed by this configuration and follows from equating gravitational and radiative forces as $L_{\text{Edd}} = 3 \times 10^4 (M/M_\odot) L_\odot$. Since the luminosity caused by spherical gas accretion is proportional to the accretion rate, the Eddington luminosity corresponds to the Eddington limit $\dot{M}_{\text{Edd}} = L_{\text{Edd}}/(\eta c^2)$ for accretion rates, where η is the efficiency of the accretion process and c is the speed of light.

References

- Altavilla, G., Fiorentino, G., Marconi, M., et al. 2004, MNRAS, 349, 1344
- Athanassoula, E. 1984, Phys. Rep., 114, 321
- Bahcall, J. N., Kirhakos, S., & Schneider, D. P. 1995, ApJ, 450, 486
- Barkhouse, W. A. & Hall, P. B. 2001, AJ, 121, 2843
- Barnes, J. & Hut, P. 1986, Nature, 324, 446
- Barnes, J. E. 1988, ApJ, 331, 699
- . 1992, ApJ, 393, 484
- Barnes, J. E. & Hernquist, L. 1996, ApJ, 471, 115
- Bendo, G. J. & Barnes, J. E. 2000, MNRAS, 316, 315
- Bernloehr, K. 1993, A&A, 268, 25
- Bessell, M. S. & Brett, J. M. 1988, PASP, 100, 1134
- Bian, W. & Zhao, Y. 2004, MNRAS, 144
- Binney, J. & Merrifield, M. 1998, Galactic astronomy (Princeton, NJ : Princeton University Press, 1998. (Princeton series in astrophysics))
- Binney, J. & Tremaine, S. 1987, Galactic dynamics (Princeton, NJ, Princeton University Press, 1987. (Princeton series in astrophysics))
- Boller, T., Brandt, W. N., & Fink, H. 1996, A&A, 305, 53
- Boroson, T. A. & Oke, J. B. 1982, Nature, 296, 397
- Boroson, T. A., Oke, J. B., & Green, R. F. 1982, ApJ, 263, 32
- Boroson, T. A., Persson, S. E., & Oke, J. B. 1985, ApJ, 293, 120
- Bosma, A. 1998, Celestial Mechanics and Dynamical Astronomy, 72, 69
- Bosma, A. 2004, in IAU Symposium no. 220, held 21 - 25 July, 2003 in Sydney, Australia. Eds: S. D. Ryder, D. J. Pisano, M. A. Walker, and K. C. Freeman. San Francisco: Astronomical Society of the Pacific, p. 39
- Botte, V., Ciroti, S., Rafanelli, P., & Di Mille, F. 2004, AJ, 127, 3168
- Bournaud, F., Combes, F., & Jog, C. J. 2004a, A&A, 418, L27
- Bournaud, F., Duc, P.-A., Amram, P., Combes, F., & Gach, J.-L. 2004b, A&A, 425, 813
- Braine, J., Duc, P.-A., Lisenfeld, U., et al. 2001, A&A, 378, 51
- Brandt, W. N. & Gallagher, S. C. 2000, New Astronomy Review, 44, 461

- Bushouse, H. A., Borne, K. D., Colina, L., et al. 2002, *ApJS*, 138, 1
- Canalizo, G. & Stockton, A. 2000, *ApJ*, 528, 201
- . 2001, *ApJ*, 555, 719
- Chatzichristou, E. T., Vanderriest, C., & Jaffe, W. 1999, *A&A*, 343, 407
- Combes, F., Boisse, P., Mazure, A., Blanchard, A., & Seymour, M. 1995, *Galaxies and Cosmology* (Springer-Verlag Berlin Heidelberg New York. Also *Astronomy and Astrophysics Library*)
- Combes, F., García-Burillo, S., Boone, F., et al. 2004, *A&A*, 414, 857
- Cretton, N., Naab, T., Rix, H., & Burkert, A. 2001, *ApJ*, 554, 291
- Davies, R., Tacconi, L., Genzel, R., & Thatte, N. 2003, *ArXiv Astrophysics e-prints*, astro-ph/0310877
- de Jong, R. S. 1996, *A&A*, 313, 45
- Dehnen, W. 2001, *MNRAS*, 324, 273
- Dubinski, J., Mihos, J. C., & Hernquist, L. 1999, *ApJ*, 526, 607
- Duc, P.-A., Bournaud, F., & Masset, F. 2004, *A&A*, 427, 803
- Dunlop, J. S., McLure, R. J., Kukula, M. J., et al. 2003, *MNRAS*, 340, 1095
- Eckart, A., van der Werf, P. P., Hofmann, R., & Harris, A. I. 1994, *ApJ*, 424, 627
- Edelson, R. A. & Malkan, M. A. 1986, *ApJ*, 308, 59
- Evans, A. S., Frayer, D. T., Surace, J. A., & Sanders, D. B. 2001, *AJ*, 121, 1893
- Fabian, A. C. 1999, *MNRAS*, 308, L39
- Falco, E. E., Kurtz, M. J., Geller, M. J., et al. 1999, *PASP*, 111, 438
- Ferrarese, L. & Merritt, D. 2000, *ApJ*, 539, L9
- Fioc, M. & Rocca-Volmerange, B. 1999, *A&A*, 351, 869
- Freeman, K. C. 1970, *ApJ*, 160, 811
- Fuchs, B. 2001, *A&A*, 368, 107
- García-Burillo, S., Combes, F., Hunt, L. K., et al. 2003, *A&A*, 407, 485
- Gebhardt, K., Bender, R., Bower, G., et al. 2000, *ApJ*, 539, L13
- Genzel, R., Tacconi, L. J., Rigopoulou, D., Lutz, D., & Tecza, M. 2001, *ApJ*, 563, 527
- Gingold, R. A. & Monaghan, J. J. 1977, *MNRAS*, 181, 375
- Glass, I. S. 1999, *Handbook of infrared astronomy* (Cambridge ; New York : Cambridge University Press, 1999. (Cambridge observing handbooks of research astronomers ; 1))

- Greenstein, J. L. & Schmidt, M. 1964, *ApJ*, 140, 1
- Hawarden, T. G., Leggett, S. K., Letawsky, M. B., Ballantyne, D. R., & Casali, M. M. 2001, *MNRAS*, 325, 563
- Hernquist, L. 1993, *ApJS*, 86, 389
- Hernquist, L. & Katz, N. 1989, *ApJS*, 70, 419
- Hernquist, L. & Mihos, J. C. 1995, *ApJ*, 448, 41
- Hibbard, J. E. & van Gorkom, J. H. 1996, *AJ*, 111, 655
- Hickson, P. & Hutchings, J. B. 1987, *ApJ*, 312, 518
- Hogg, D. W. 1999, *ArXiv Astrophysics e-prints*, astro-ph/9905116v3
- Howell, S. B. 2000, *Handbook of CCD astronomy* (Cambridge, U.K. ; New York : Cambridge University Press, c2000. (Cambridge observing handbooks for research astronomers ; 2))
- Hummer, D. G. & Storey, P. J. 1987, *MNRAS*, 224, 801
- Hunt, L. K., Malkan, M. A., Moriondo, G., & Salvati, M. 1999, *ApJ*, 510, 637
- Hutchings, J. B. & Crampton, D. 1990, *AJ*, 99, 37
- Hutchings, J. B. & Neff, S. G. 1997, *AJ*, 113, 550
- Hyland, A. R. & Allen, D. A. 1982, *MNRAS*, 199, 943
- Koopmans, L. V. E., Treu, T., Fassnacht, C. D., Blandford, R. D., & Surpi, G. 2003, *ApJ*, 599, 70
- Koornneef, J. 1983, *A&A*, 128, 84
- Krolik, J. H. 1999, *Active galactic nuclei : from the central black hole to the galactic environment* (Princeton, N. J. : Princeton University Press, c1999.)
- Laine, S., van der Marel, R. P., Rossa, J., et al. 2003, *AJ*, 126, 2717
- Lancon, A. & Rocca-Volmerange, B. 1992, *A&AS*, 96, 593
- Laor, A., Jannuzi, B. T., Green, R. F., & Boroson, T. A. 1997, *ApJ*, 489, 656
- Leighly, K. M., Mushotzky, R. F., Nandra, K., & Forster, K. 1997, *ApJ*, 489, L25
- Lim, J. & Ho, P. T. P. 1999, *ApJ*, 510, L7
- Lipari, S., Colina, L., & Macchetto, F. 1994, *ApJ*, 427, 174
- Lucy, L. B. 1977, *AJ*, 82, 1013
- Ma, C., Arias, E. F., Eubanks, T. M., et al. 1998, *AJ*, 116, 516
- MacKenty, J. W. & Stockton, A. 1984, *ApJ*, 283, 64

- Magorrian, J., Tremaine, S., Richstone, D., et al. 1998, *AJ*, 115, 2285
- Maiolino, R. 2001, *Memorie della Societa Astronomica Italiana*, 72, 43
- Maiolino, R., Oliva, E., Ghinassi, F., et al. 2004, *A&A*, 420, 889
- Makino, J., Fukushige, T., Koga, M., & Namura, K. 2003, *PASJ*, 55, 1163
- Mathur, S. 2000, *MNRAS*, 314, L17
- Matthews, T. A., Bolton, J. G., Greenstein, J. L., Munch, G., & Sandage, A. R. 1961, *Sky and Telescope*, 21, 148
- Matthews, T. A. & Sandage, A. R. 1963, *ApJ*, 138, 30
- McLeod, K. K. & McLeod, B. A. 2001, *ApJ*, 546, 782
- Meyer, M. R., Edwards, S., Hinkle, K. H., & Strom, S. E. 1998, *ApJ*, 508, 397
- Mihos, C. 1999, *Ap&SS*, 266, 195
- Mihos, J. C. & Hernquist, L. 1994, *ApJ*, 437, 611
- . 1996, *ApJ*, 464, 641
- Miyamoto, M. & Nagai, R. 1975, *PASJ*, 27, 533
- Monaghan, J. J. 1989, *Journal of Computational Physics*, 82, 1
- . 1992, *ARA&A*, 30, 543
- Moorwood, A., Cuby, J.-G., Biereichel, P., et al. 1998, *The Messenger*, 94, 7
- Naab, T. & Burkert, A. 2003, *ApJ*, 597, 893
- Neugebauer, G. & Matthews, K. 1999, *AJ*, 118, 35
- Neugebauer, G., Soifer, B. T., Matthews, K., & Elias, J. H. 1989, *AJ*, 97, 957
- Neugebauer, G., Soifer, B. T., & Miley, G. K. 1985, *ApJ*, 295, L27
- Oke, J. B. & Lauer, T. R. 1979, *ApJ*, 230, 360
- Origlia, L., Moorwood, A. F. M., & Oliva, E. 1993, *A&A*, 280, 536
- Osterbrock, D. E. & Pogge, R. W. 1985, *ApJ*, 297, 166
- Palunas, P. & Williams, T. B. 2000, *AJ*, 120, 2884
- Peacock, J. A. 1999, *Cosmological physics* (Cambridge, UK: Cambridge University Press, 1999.)
- Peletier, R. F., Knapen, J. H., Shlosman, I., et al. 1999, *ApJS*, 125, 363
- Percival, W. J., Miller, L., McLure, R. J., & Dunlop, J. S. 2001, *MNRAS*, 322, 843
- Persic, M., Salucci, P., & Stel, F. 1996, *MNRAS*, 281, 27

- Persson, S. E., Murphy, D. C., Krzeminski, W., Roth, M., & Rieke, M. J. 1998, *AJ*, 116, 2475
- Pfalzner, S. & Gibbon, P. 1997, *Many-Body Tree Methods in Physics* (Cambridge University Press, 1997.)
- Phillips, M. M. 1976, *ApJ*, 208, 37
- Pickles, A. J. 1998, *PASP*, 110, 863
- Poggianti, B. M. 1997, *A&AS*, 122, 399
- Pounds, K. A., Done, C., & Osborne, J. P. 1995, *MNRAS*, 277, L5
- Press, W. H., Teukolsky, S. A., Vetterling, W. T., & Flannery, B. P. 1992, *Numerical recipes in FORTRAN. The art of scientific computing* (Cambridge University Press, c1992, 2nd ed.)
- Ratnam, C. & Salucci, P. 2000, *New Astronomy*, 5, 427
- Rieke, G. H. & Lebofsky, M. J. 1985, *ApJ*, 288, 618
- Rigopoulou, D., Spoon, H. W. W., Genzel, R., et al. 1999, *AJ*, 118, 2625
- Rodríguez-Ardila, A., Viegas, S. M., Pastoriza, M. G., & Prato, L. 2002, *ApJ*, 579, 214
- Samland, M. & Gerhard, O. E. 2003, *A&A*, 399, 961
- Sanders, D. B. 1999, *Ap&SS*, 266, 331
- . 2003, *Journal of Korean Astronomical Society*, 36, 149
- Sanders, D. B. & Mirabel, I. F. 1996, *ARA&A*, 34, 749
- Sanders, D. B., Soifer, B. T., Elias, J. H., et al. 1988, *ApJ*, 325, 74
- Sargent, W. L. W. 1970, *ApJ*, 160, 405
- Scharwächter, J. 2001, Master's thesis, I. Physikalisches Institut der Universität zu Köln
- Scharwächter, J., Eckart, A., Pfalzner, S., et al. 2003, *A&A*, 405, 959
- . 2004, *A&A*, 414, 497
- Schinnerer, E., Eckart, A., & Tacconi, L. J. 1998, *ApJ*, 500, 147
- Schmidt, M. 1963, *Nature*, 197, 1040
- Schmidt, M. & Green, R. F. 1983, *ApJ*, 269, 352
- Scoville, N. Z., Evans, A. S., Thompson, R., et al. 2000, *AJ*, 119, 991
- Scoville, N. Z., Frayer, D. T., Schinnerer, E., & Christopher, M. 2003, *ApJ*, 585, L105
- Scoville, N. Z., Padin, S., Soifer, B. T., Yun, M. S., & Sanders, D. B. 1993, *Bulletin of the American Astronomical Society*, 25, 1241

- Shlosman, I. & Heller, C. H. 1994, in *Mass-Transfer Induced Activity in Galaxies*, Proceedings of the Conference held at the University of Kentucky, Lexington, April 26-30, 1993. Edited by Isaac Shlosman. Cambridge: Cambridge University Press, 1994, p. 274
- Soifer, B. T., Sanders, D. B., Madore, B. F., et al. 1987, *ApJ*, 320, 238
- Solomon, P. M., Downes, D., Radford, S. J. E., & Barrett, J. W. 1997, *ApJ*, 478, 144
- Staguhn, J. G., Schinnerer, E., Eckart, A., & Scharwächter, J. 2004, *ApJ*, 609, 85
- Stockton, A. 1982, *ApJ*, 257, 33
- Stockton, A. & Ridgway, S. E. 1991, *AJ*, 102, 488
- Sundelius, B., Thomasson, M., Valtonen, M. J., & Byrd, G. G. 1987, *A&A*, 174, 67
- Surace, J. A., Sanders, D. B., & Evans, A. S. 2001, *AJ*, 122, 2791
- Tacconi, L. J., Genzel, R., Lutz, D., et al. 2002, *ApJ*, 580, 73
- Toomre, A. 1977, in *Evolution of Galaxies and Stellar Populations*, Proceedings of a Conference at Yale University, May 19-21, 1977. Edited by Beatrice M. Tinsley and Richard B. Larson. New Haven: Yale University Observatory, 1977, p. 401
- Toomre, A. 1981, in *Structure and Evolution of Normal Galaxies*, 111–136
- Toomre, A. & Toomre, J. 1972, *ApJ*, 178, 623
- Urry, C. 2004, in *AGN Physics with the Sloan Digital Sky Survey*, Proceedings of a conference held in Princeton, NJ, USA, 27-31 July 2003, Edited by Gordon T. Richards and Patrick B. Hall, ASP Conference Series, Volume 311. San Francisco: Astronomical Society of the Pacific, 2004, p. 49
- Véron-Cetty, M.-P., Joly, M., & Véron, P. 2004, *A&A*, 417, 515
- Veilleux, S., Kim, D.-C., & Sanders, D. B. 1999, *ApJ*, 522, 113
- . 2002, *ApJS*, 143, 315
- Walker, I. R., Mihos, J. C., & Hernquist, L. 1996, *ApJ*, 460, 121
- Wallace, L. & Hinkle, K. 1997, *ApJS*, 111, 445
- Weymann, R. J., Morris, S. L., Foltz, C. B., & Hewett, P. C. 1991, *ApJ*, 373, 23
- Wilkinson, P. N., Tzioumis, A. K., Benson, J. M., et al. 1991, *Nature*, 352, 313
- Willott, C. J., Rawlings, S., & Grimes, J. A. 2003, *ApJ*, 598, 909
- Wink, J. E., Guilloteau, S., & Wilson, T. L. 1997, *A&A*, 322, 427
- Yuan, M. J. & Wills, B. J. 2003, *ApJ*, 593, L11
- Zakamska, N. L., Strauss, M. A., Krolik, J. H., et al. 2003, *AJ*, 126, 2125
- Zuther, J., Eckart, A., Scharwächter, J., Krips, M., & Straubmeier, C. 2004, *A&A*, 414, 919

Acknowledgements

My special thanks go to the supervisor of my thesis, Prof. Dr. Andreas Eckart, for his inspiring suggestions and clear-sighted ideas, and to HD Dr. Susanne Pfalzner for her very competent and enthusiastic support with my numerical investigations. Both have been ready at any time to help when problems arose, and it has been a great pleasure to work with them and to learn from their experience.

I have very much enjoyed the cordial and encouraging ambience in the group on the red floor of the institute. My thanks go to all members of the group for over and over answering questions, helping with computer problems and the many other workaday difficulties, and for calming down my panic attacks during the final stage of thesis-writing. I would like to especially thank Jens Zuther, with whom I spent a lot of time, struggling to learn data reduction and to prepare proposals, and who gave me very helpful comments on a part of my thesis, and Dr. Rainer Schödel, who carefully read through a version of my thesis and gave me new insights into the magics of image reduction.

I am particularly grateful to Prof. Dr. Lars Hernquist, who kindly provided the codes TREESPH and BUILDGAL and gave helpful advice during my visit at the *Harvard-Smithsonian Center for Astrophysics (CfA)* in Cambridge (USA). This visit was kindly supported by a travel grant of the *Käthe-Hack-Stiftung*. I would also like to thank Dr. Peter Englmaier for sharing his expertise on SPH simulations and Prof. Dr. Burkhard Fuchs for inspiring the swing amplification approach. Dr. Richard Davies kindly provided an IRAF script for the reduction of long-slit spectra which was a very helpful introduction to the basic steps of reduction techniques. My particular thanks go to Melanie Krips and Jens Zuther as well as to Dr. Johannes Staguhn and Dr. Eva Schinnerer for exciting collaborations on 3C 48 and I Zw 1, respectively, and to Dr. Jeremy Lim, who kindly provided HI data, which I partly used for the compilation of the gas rotation curve of I Zw 1 during my diploma thesis. The visualization of the galaxy simulations is very much improved by the interesting collaboration with Volker Winkelmann from the *Regional Computer Center of the University of Cologne (ZAIK/RRZK)*.

Two years of my doctoral studies were kindly supported by a fellowship for doctoral students of the *Studienstiftung des deutschen Volkes (German National Academic Foundation)*. In addition, this work was partly supported by the *Deutsche Forschungsgemeinschaft (DFG)* via grant SFB 494.

Last but not least, I am deeply indebted to my parents and my brother for their invaluable support in cheering me up again and again and for their never-ending patience. My mother struggled through the typos of my thesis in a single day, and I am particularly thankful to my parents for discussing the corrections during an endless weekend-session.

This work is partly based on observations carried out at the *Very Large Telescope (UT1)* of the *European Southern Observatory* on Cerro Paranal in Chile under project 67.B-0009. I am grateful to the anonymous observer who did the service-mode observations. This research has made use of the *NASA/IPAC Infrared Science Archive* and the *NASA/IPAC Extragalactic Database (NED)*, which are operated by the *Jet Propulsion Laboratory, California Institute of Technology*, under contract with the *National Aeronautics and Space Administration*, and of data products from the *Two Micron All Sky Survey*, which is a joint project of the *University of Massachusetts* and the *Infrared Processing and Analysis Center/California Institute of Technology*, funded by the *National Aeronautics and Space Administration* and the *National Science Foundation*.

Erklärung

Ich versichere, dass ich die von mir vorgelegte Dissertation selbständig angefertigt, die benutzten Quellen und Hilfsmittel vollständig angegeben und die Stellen der Arbeit - einschließlich Tabellen, Karten und Abbildungen -, die anderen Werken im Wortlaut oder dem Sinn nach entnommen sind, in jedem Einzelfall als Entlehnung kenntlich gemacht habe; dass diese Dissertation noch keiner anderen Fakultät oder Universität zur Prüfung vorgelegen hat; dass sie - abgesehen von unten angegebenen Teilpublikationen - noch nicht veröffentlicht worden ist sowie, dass ich eine solche Veröffentlichung vor Abschluss des Promotionsverfahrens nicht vornehmen werde. Die Bestimmungen dieser Promotionsordnung sind mir bekannt. Die von mir vorgelegte Dissertation ist von Herrn Prof. Dr. Andreas Eckart betreut worden.

Teilpublikationen

Scharwächter, J., Eckart, A., Pfalzner, S., Zuther, J., Krips, M., Schinnerer, E., & Staguhn, J., To appear in the Proceedings of the 2004 European Workshop: "Dense Molecular Gas around Protostars and in Galactic Nuclei", Eds. Y. Hagiwara, W.A. Baan, H.J. van Langevelde, 2004, a special issue of *Ap&SS*, Kluwer: *The QSO Hosts I Zw 1 and 3C 48: Prototypes of a Merger-Driven Quasar Evolution?*

Scharwächter, J., Eckart, A., Pfalzner, S., Zuther, J., Krips, M., & Straubmeier, C. 2004, *A&A*, 414, 497: *A multi-particle model of the 3C 48 host*

Scharwächter, J., 2004, *Sterne und Weltraum*, August 2004, pp.14: *Der Wirt des Quasars 3C 48 - Galaxienverschmelzung in flagranti*

Scharwächter, J., Eckart, A., Pfalzner, S., Moulta, J., Straubmeier, C., & Staguhn, J. G. 2003, *A&A*, 405, 959: *I Zw 1: Decomposition of the nearby QSO host*

Scharwächter, J., Eckart, A., Pfalzner, S., Moulta, J., Straubmeier, C., Staguhn, J., & Schinnerer, E. 2003, in: "The Dense Interstellar Medium in Galaxies", Proceedings of the 4th Cologne-Bonn-Zermatt-Symposium, held September 22-26, 2003, in Zermatt, Switzerland, Ed: Susanne Pfalzner, Carsten Kramer, Christian Straubmeier, and Andreas Heithausen, Springer, 666p. ISBN 354021254X, p.143: *The Nearby QSO Host I Zw 1: NIR Probing of Structural Properties and Stellar Populations*

Scharwächter, J., Eckart, A., Pfalzner, S., Staguhn, J., & Schinnerer, E. 2003, in: Proceedings of the 3rd Euroconference: "The Evolution of Galaxies, III - From Simple Approaches to Self-Consistent Models", Eds. G. Hensler, G. Stasińska, S. Harfst, P. Kroupa, Chr. Theis, *Ap&SS*, 284, 507: *I Zwicky 1: Decomposition and dynamics of the nearby QSO host*

Julia Scharwächter

Adresse: Westfalenweg 49, D-42651 Solingen

Telefon: (++49)(+212)44882

E-mail: scharw@ph1.uni-koeln.de

Persönliche Angaben

Nationalität: deutsch

Geburtsdatum: 9. Mai 1977

Geburtsort: Solingen

Ausbildung

Schule

1983 - 1987

Grundschule Meigen (Solingen)

1987 - 1996

Gymnasium August-Dicke-Schule (Solingen)

1996

Abitur

Universität

1996 - 2001

Physikstudium (Universität zu Köln)

1998

Physik Vordiplom

12/2001

Physik Diplom

Diplomarbeit: "The Dynamics of the Nearby QSO Host I Zw 1"

Betreuer: Prof. Dr. Andreas Eckart

seit 01/2002

Doktorarbeit (I. Physikalisches Institut der Universität zu Köln)

Dissertationsthema: "Merger Dynamics and Stellar Populations in the Host Galaxies of the Quasi-Stellar Objects I Zw 1 and 3C 48"

Betreuer: Prof. Dr. Andreas Eckart

Anstellungen und Stipendien

10/2000 - 12/2001

Studentische Hilfskraft (I. Physikalisches Institut der Universität Köln)

01/2002 - 06/2002

Wissenschaftliche Mitarbeiterin (I. Physikalisches Institut der Universität Köln)

07/2002 - 06/2004

Promotionsstipendium der Studienstiftung des deutschen Volkes

seit 07/2004

Wissenschaftliche Mitarbeiterin (I. Physikalisches Institut der Universität zu Köln)

Sprachen

Englisch (fließend in Wort und Schrift)

Spanisch (gute Grundkenntnisse)

Französisch (gute Grundkenntnisse)

Latein (Latinum)